Synthesis and luminescent properties of aluminium oxide-titanium dioxide nanocomposites doped with different rare-earths ions

By

Mokoena Teboho Patrick

(BSc. Hons)

A thesis is submitted in partial fulfilment of the requirements for the degree

Magister Scientiae (Nanoscience)

in the

Faculty of Natural and Agricultural Science

Department of Physics

at the

University of the Free State

Supervisor : Prof. O.M. Ntwaeaborwa

Co-supervisor : Prof. H.C. Swart

January 2016

Dedication

Dedicated to my family and the memory of my late grandmother

Liau Tlalane Emily

(1933 - 2015)

Declaration

(i) “I, Mokoena Teboho Patrick, declare that the Master of Science Degree research thesis or interrelated, publishable manuscripts / published articles, or coursework Master of Science Degree mini-thesis that I herewith submit for the Master of Science Degree qualification at the University of the Free State is my independent work, and that I have not previously submitted it for qualification at another institution of higher education.”

(ii) “I, Mokoena Teboho Patrick, hereby declare that I am aware that the copyright is vested in the University of the Free State.”

(iii) “I, Mokoena Teboho Patrick, hereby declare that all royalties as regards intellectual property that was developed during the course of and/or in connection with the study at the University of the Free State will accrue to the University.”

In the event of a written agreement between the University and the student, the written agreement must be submitted in lieu of the declaration by the student.

Signature **Date**

Acknowledgements

First of all I would like to give thanks to **God** Almighty for making it all possible for me to complete this study even when I was experiencing rough patches because with Him nothing is impossible. I would like to thank my supervisor **(Prof. Odireleng M. Ntwaeaborwa)** and co-supervisor (**Prof. Hendrik C. Swart)** for letting me to be a member of their esteemed research group. I cannot thank you enough for your encouragement that made me feel confident throughout this thesis work. Your patience and continuous support really meant a lot to me.

Dr Vinod Kumar I am deeply grateful for your guidance and patience when introducing me to the synthesis of nano-phosphors and to the various characterization techniques. **Prof. Robin E. Kroon** and **Dr. Anurag Pandey** I am very grateful for your fruitful discussions and advice you gave me during up-conversion measurements.

I would also like to thank everyone in the Physics department of the University of the Free State for their support. Working in such a friendly environment full of extremely helpful professionals who share their experiences with no hesitation was a privilege for me. I would also like to thank all members of **Prof. J.R Botha's** research group from Nelson Mandela Metropolitan University (NMMU) particularly **Dr. Z.N. Urgessa "Zola"** for his help during photoluminescence measurements.

Mr Sefako J. Mofokeng and **Mr Mpho S. Mokoena**, my colleagues, who never deprived me of their amazing discussions and advice we share together not only in research but in social life as well. Your kindness is very much appreciated. Additionally, members of Ntwaeaborwa Research Group (**NRG)**, I want to thank you all for your friendship and also for serious and at the same time funny discussions we had on our weekly group meetings.

Special thanks to all presenters of **Metro FM radio station**, you cannot imagine how many days and nights you managed to keep me alert in front of a laptop screen by means of your gorgeous playlists. I would like to express my deepest gratitude to my lovely family **("Bakoena ba ha Mohlakoana")** and my friend **(Maditaba K. Malakoane)** for their unconditional love and support.

Finally, I would like to thank National Nanoscience Postgraduate Teaching and Training Platform **(NNPTTP)** and **UFS** for their financial support during my course work and research project.

Abstract

Alumina-titania (Al_2O_3-TiO_2) is one of the most useful nano-composites to host up-conversion rare-earth (UCRE) ions to prepare light emitting nano-materials or nano-phosphors. These nano-composites have received a special attention because of their excellent thermal, chemical and mechanical stability. Alumina (Al_2O_3) is a ceramic material with high level of strength, toughness and tribological properties. Titania (TiO_2) is a wide bandgap semiconductor material that is used in different application including photocatalytic activities, solar cells, hydrogen storage and sensors.

The singly doped α- Al_2O_3:Yb^{3+} phosphor powder was successfully synthesized by solution combustion method. The structure of the phosphor powders was characterized with powder X-ray diffractometer (XRD). The XRD patterns confirmed that the phosphors crystallized in the hexagonal phases of α-Al_2O_3 with space group R3c and the average crystallite size was 29 nm estimated from Debye-Scherrer equation. The Fourier transform infrared (FTIR) measurements confirmed the characteristic bonds of Al-O from α-Al_2O_3. The particle morphology and elemental composition of the phosphors were characterized by field emission scanning electron microscope (FE-SEM) coupled with an energy dispersive x-ray spectroscopy (EDS). The phosphor powders were excited in ultraviolet (UV) region with excitation wavelength of 325 nm and the corresponding near infrared (NIR) emission was observed at 975 nm. The NIR emission was assigned to ${}^2F_{5/2} \rightarrow {}^2F_{7/2}$ transition of Yb^{3+}. The bluish green emission with maxima at ~ 480 nm was observed as a result of cooperative luminescence of Yb^{3+} when the powders were excited in the NIR with excitation wavelength of 980 nm.

The TiO_2:Er^{3+} nano-phosphor powder were successfully synthesized by sol-gel method at room temperature XRD confirmed that nano-phosphor has crystallized in the tetragonal phases of anatase and rutile with space groups of $\frac{4_1}{a}$md and $P\frac{4_2}{m}$nm, respectively. An average crystallite size of the undoped TiO_2 was 26 nm. The FE-SEM confirmed nano-rods particle morphology with diameter and length of 78 ± 36 nm and 1.51 ± 0.30 µm, respectively. The FTIR revealed the characteristic bonds of Ti-O due to the presence of TiO_6 in titania. The nano-phosphor powders were excited in the NIR region with excitation wavelength of 980 nm and the corresponding visible emissions were observed at 527, 564 and 665 nm. The green emission with maxima at

527 and 564 nm were assigned to ($^2H_{11/2}$, $^4S_{3/2}$)→$^4I_{15/2}$ while red emission at 665 nm was assigned to $^4F_{9/2}$→$^4I_{15/2}$ transition of Er^{3+} ion. The excited state absorption (ESA) mechanism of up-conversion (UC) process was discussed extensively.

The nano-composites of Al_2O_3-TiO_2:Yb^{3+},Er^{3+} and Al_2O_3-TiO_2:Yb^{3+},Tm^{3+} phosphor powders were successfully synthesized by sol-gel method. XRD patterns confirmed the mixed oxides of titania (TiO_2) rutile phase and an early crystallization of alumina (α-Al_2O_3) phase. The XRD patterns were consistent with JCPDS card no. 46-1212 and 21-1272 for α-Al_2O_3 and TiO_2 rutile phases, respectively. An average crystallite size of ~ 36 nm was estimated from Debye-Scherrer equation. FE-SEM confirmed nano-rods morphology self-assembled with spherical particles. In Yb^{3+}-Er^{3+} codoped nano-composites; the powders were excited in the NIR region with excitation wavelength of 980 nm and corresponding visible emissions were observed at 523, 548 and 658 nm. The green emission with maxima at 523 and 548 nm were assigned to ($^2H_{11/2}$, $^4S_{3/2}$)→$^4I_{15/2}$ while red emission at 658 nm was assigned to $^4F_{9/2}$→$^4I_{15/2}$ transition of Er^{3+} ion. In Yb^{3+}-Tm^{3+} codoped nano-composites; the powders were excited in NIR region with excitation wavelength of 980 nm and corresponding visible to NIR emissions were observed at 480, 650, 693 and 800 nm. The blue emission with maxima at 480 nm was assigned to $^1G_4$→$^3H_6$, red emission with maxima at 650 and 693 nm were assigned to $^1G_4$→$^3F_4$ and $^3F_3$→$^3H_6$ and NIR emission with maxima at 800 nm was attributed to $^3H_4$→$^3H_6$ transitions of Tm^{3+} ion. The other optical properties were investigated with the characterization techniques such as FTIR and UV-vis.

KEYWORDS

Alumina, titania, nano-composites, nano-phosphor, up-conversion, red, green, blue, near-infrared, emission.

ACRONYMS

nm	-	Nanometer
CNTs	-	Carbon nanotubes
QDs	-	Quantum dots
UC	-	Up-conversion
IR	-	Infrared

NIR	-	Near infrared
DSSCs	-	Dye-sensitized solar cells
a-Si	-	Amorphous silicon
c-Si	-	Crystalline silicon
RE	-	Rare-earths
SCS	-	Solution Combustion Synthesis
XRD	-	X-ray diffracrometer
UV-vis-NIR	-	Ultraviolet-Visible-Near infrared
FTIR	-	Fourier transform infrared
FE-SEM	-	Field emission scanning electron microscope
EDS	-	Energy dispersive x-ray spectroscopy
PL	-	Photoluminescence
CL	-	Cathodoluminescence
TL	-	Thermoluminescence
EL	-	Electroluminescence
ET	-	Energy transfer
ESA	-	Excited state absorption
ETU	-	Energy transfer up-conversion
CUC	-	Cooperative up-conversion
GSA	-	Ground state absorption
HCP	-	Hexagonal close-packed
MOCVD	-	Metalorganic chemical vapour deposition
UCRE	-	Up-conversion rare earths
FWHM	-	Full width half at maximum

Table of contents

List of figures

List of tables

1. Introduction

1.1 History of nanoscience and nanotechnology

The study of nanoscience and nanotechnology has generated a great attention in all the fields of science and technology. The materials and structures with at least one dimension that is less than 100 nanometer (nm) have novel properties which enable them to play an important role in the rapid progress of the fields of science and technology [1]. In 1959 the American physicist Richard Feynman gave a lecture with the title: “There is plenty of room at the bottom”. In this lecture, Feynman described a process by which the ability to manipulate individual atoms in a molecular level might be developed [2]. In addition, he also mentioned that scaling issues would arise from altering the size of various physical phenomena: Gravity would become less important, surface tension and Van der Waals attraction would become more important. The term “nanotechnology” was introduced in 1974 by Japanese scientist Norio Taniguchi in a conference. He described the term mainly as consisting of the processing of separation, consolidation and deformation of materials by one atom or one molecule [3]. However, the term nanotechnology was not used again until 1980s when the American engineer Eric Dexler, who was not aware of Taniguchi’s prior use of the term, published a first paper based on nanotechnology in 1981 [4].

Nanotechnology or nanoscience is a multidisciplinary field which covers a broad area of expertise including classical fields of physics, chemistry, biology, material science, electrical, mechanical and chemical engineering [5]. Many researchers have found that the existence of nano-sized particles have been present on earth for millions of years up-to-date and have been used by mankind for thousands of years [6]. In the 4th century the application of nano-materials was first observed from the Roman glass cage cup called the Lycurgus cup which is coated with gold (Au) nanoparticles (shown in Figure 1.1). The cup displays different colours when irradiated with light from different angles. The cup displays red light when lit from behind (Fig.1.1(a)) and green light when lit from front (Fig.1.1(b)) [7]. Nowadays, we are exposed to nano-materials on a daily basis through the products we use or the use of materials in work places. For example personal care products (cosmetics), sporting goods (tennis racquet), electronics (mobile phones) and the automotive industries (hydrophobic windscreens). The novel properties of these nano-materials due to their small size, morphology and their ability to alter their sizes and shapes by employing various synthesis methods, have shown great interest in research and development (R&D). Currently, nano-sized materials are widely used in various sectors of science including energy, electronics, biomedicine, pharmaceuticals, cosmetics and environmental studies. Amongst all the sectors, application of nano-materials in energy particularly in solar cells is one of the most focused areas of research [8-10].

Figure 1.1: A Lycurgus cup showing (a) a red colour when lit behind and (b) green colour when lit in front [7].

1.2 Nano-materials

Nano-materials can be metals, ceramics, polymeric materials or composites materials with particle sizes that range between 1 and 100 nm. Figure 1.2 depicts schematic diagram of material scale on how small nano is. There are different types of nano-materials existing such as carbon nanotubes (CNTs), fullerenes, quantum dots (QDs), dendrimers, nano-powders, nano-composites, nano-alloys, nano-wires and metal oxides. Amongst all the nano-materials, nano-composites have a wide range of applications due to their tremendous properties. Nano-composites are made up of two or more dissimilar materials and mixed together at the nanometer scale to form new product with novel and improved physical and chemical properties [11]. This study was aimed at preparing and characterizing luminescent nano-composites that could be used to enhance power conversion efficiency of solar cells.

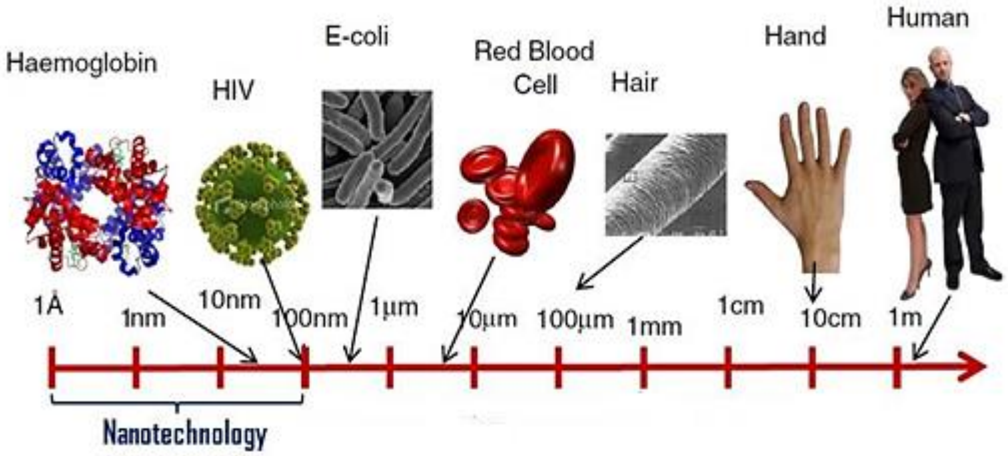

Figure 1.2: Schematic diagram of how small is nano [12].

1.3 Problem statement

Technology has always been a key determinant of energy consumption. The demand for energy is growing rapidly because of the advances in technology. There are various sources of energy such as nuclear energy, coal, wood, oil and gas but they have there are own drawbacks. Nuclear power plants are very expensive and they take long time to construct, and poses dangerous radiation. The other sources of energy which are coal, wood, oil and gas produce large amounts of carbon dioxide (CO_2) pollution. Therefore, they are not environmental friendly they cause global warming. Considering the fact that coal also needs to be transported from mines to the coal-fired power plant locations these leads to the high cost in transportation and delays in coal delivery. In addition, coal in South Africa (SA) is considered to be one of the most dominant primary energy supply as shown in figure 1.3 [13, 14].

All the above mentioned information challenged scientists to look for clean and inexpensive alternative energy sources such as hydroturbines and solar cells i.e green energy. The use of hydroturbines to generate electric power becomes limited due to the droughts and unpredictable weather patterns experienced in many parts of the world due to global warming effects. Solar cells are widely used because they generate electricity by using sunlight which is readily available. Research in solar cells is very crucial to our society because it will help so many families and industries to reduce the costs of electricity. Solar cells offer pollution-free, long-term, maintenance-free, efficient and are reliable. The average daily solar radiation in South Africa (SA) vary between 4.5 and 6.5 kWh/m^2 which are good compared to United States (3.6 kWh/m^2) and Europe (2.5 kWh/m^2) . Therefore, it is reasonable why research and development (R&D) based on solar cells requires a great attention in SA [15].

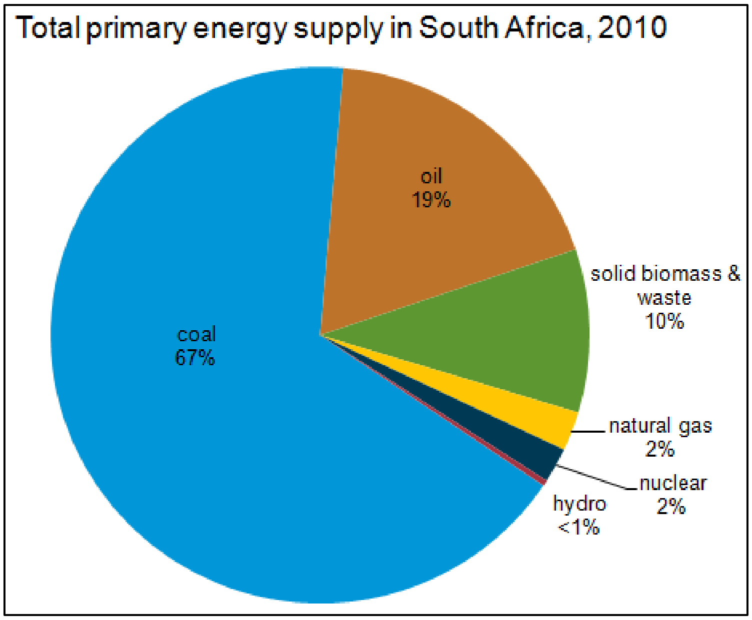

Figure 1.3: South Africa's primary energy supply sources as captured in 2010 [14].

To minimize the cost of harvesting shorter-energy photons from the solar spectrum or how to improve the efficiency of solar cells has been a challenge for the past years. Therefore, the application of the luminescent up-conversion (UC) nano-materials has been proposed as efficient methods for enhancing the poor spectral response of solar cells in an infrared (IR) region particularly for dye sensitized solar cells (DSSCs), silicon (Si) solar cells and organic solar cells [16-18]. The poor spectral response is due to transmission of photons with energy lower than the bandgap not being absorbed. Therefore, transmission losses contribute more to the losses for wider bandgap solar cells [17].

1.4 Research aim and objectives

This study was conducted to investigate the UC luminescence properties of Al_2O_3-TiO_2 nano-composites doped with different rare-earths (RE) such as ytterbium (Yb^{3+}), erbium (Er^{3+}) and thulium (Tm^{3+}). These UC luminescence properties display potential applications in solar cells. This work was proposed because transmission is a major problem in solar cells as a result of lower-energy photon than energy bandgap. The aim was to prepare UC nano-composites that will harvest lower-energy photons in the near infrared (NIR) and convert them to higher-energy photons in the visible region. The objectives of this study were as follows:

- To prepare the host matrix Al_2O_3, TiO_2 and Al_2O_3-TiO_2 by sol-gel method and solution combustion synthesis (SCS).
- To investigate the crystal structure of Al_2O_3, TiO_2 and Al_2O_3-TiO_2 by powder x-ray diffractometer (XRD).
- To investigate the optical properties of Al_2O_3, TiO_2 and Al_2O_3-TiO_2 by UV-vis-NIR spectrophotometer and Fourier transform infrared (FTIR).
- To characterize particle morphology and elemental composition by a field emission scanning electron microscope (FE-SEM) coupled with energy dispersive x-ray spectroscopy (EDS).
- To investigate the cooperative luminescence of singly doped Yb^{3+} by photoluminescence (PL) spectroscopy.
- To study the UC luminescence properties of a singly doped Er^{3+}.
- To investigate the energy transfer from Yb^{3+} to Er^{3+} in Al_2O_3-TiO_2 nano-composites.
- To investigate the energy transfer from Yb^{3+} to Tm^{3+} in Al_2O_3-TiO_2 nano-composites.

1.5 Thesis layout

This mini-thesis is divided into eight chapters. Chapter 1 gives an overview of the history of nanoscience and nanotechnology, problem statement, aims and objectives. Chapter 2 provides a theoretical background on photoluminescence, UC luminescence, a host matrix Al_2O_3, TiO_2 and Al_2O_3-TiO_2, and applications of UC phosphor based nano-materials in various fields. Chapter 3 gives a brief description of the synthesis techniques that were used to prepare nano-materials. Chapter 4 presents a brief description of the characterization techniques that were used to investigate the properties of nano-materials. Chapter 5 presents cooperative luminescence from low temperature synthesis of α-Al_2O_3:Yb^{3+} phosphor by using solution combustion method. The study of structural properties and up-conversion luminescence in TiO_2:Er^{3+} nano-phosphor is discussed in chapter 6. Chapter 7 presents up-conversion luminescence and nano-composites features of Al_2O_3-TiO_2:Yb^{3+},RE (RE = Er^{3+} and Tm^{3+}) powders. Chapter 8 gives summary and conclusion of the thesis and suggestions for future work.

1.6 References

[1]. L.F. Koao, B.F. Dejene, H.C. Swart, Material properties of semiconducting nanostructures synthesized using the chemical bath deposition method, PhD Thesis, (2013), University of the Free State, Bloemfontein, South Africa.

[2]. T.D. Malevu, R.O. Ocaya, Synthesis of ZnO nanoparticles using environmentally friendly zinc-air system, MSc Thesis, (2014), University of the Free State, Qwaqwa, South Africa.

[3]. J. Gribbin, M. Gribbin, Richard Feynman: A life in science, (1997), Dutton Adult, page 70.

[4]. https://en.wikipedia.org/wiki/History_of_nanotechnology [Last accessed 05 December 2015].

[5]. https://nanohub.org/resources/1906 (Last accessed 05 December 2015].

[6]. B. Nowack, T.D. Bucheli, Environmental Pollution, 150 (2007) 5 - 22.

[7]. https://en.wikipedia.org/wiki/Lycurgus_Cup [Last accessed 05 December 2015].

[8]. Q. Li, J. Lin, J. Wu, Z. Lan, Y. Wang, F. Peng, M. Huang, Electrochimica Acta, 56 (2011) 4980 - 4984.

[9]. J. Zheng, Y. Tao, W. Wang, Z. Ma, Y. Zuo, B. Cheng, Q. Wang, Journal of Luminescence, 132 (2012) 2341 - 2344.

[10]. H. Lian, Z. Hou, M. Shang, D. Geng, Y. Zhang, J. Lin, Energy, 57 (2013) 270 - 283.

[11]. M.R. Mohammadi, Materials Science in Semiconductor Processing, 27 (2014) 711 - 718.

[112]. http://electroiq.com/blog/2013/10/mems-devices-for-biomedical-applications/. [Last accessed 07 December 2015].

[13]. A.R. Jha, Solar Cell Technology and Applications, (2010), Auerbach Taylor & Francis Group, United States of America, page 1 - 5.

[14]. https://en.wikipedia.org/wiki/Energy in South Africa [Last accessed 20 January 2015].

[15]. F.R Cummings, TiO_2 nanaotube based dye-sensitised solar cells, PhD Thesis, (2012), University of the Western Cape, Cape Town, Western Cape.

[16]. G.-B. Shan, G. P. Demopoulos, Advanced materials, 22 (2010) 4373 - 4377.

[17]. P. Ramasamy, P. Manivasakan, J. Kim, Royal Society of Chemistry Advances, 4 (2014) 34873 - 34895.

[18]. H. -Q. Wang, T. Stubhan, A. Osvet, I. Litzov, C.J. Brabec, Solar Energy Materials & Solar Cells, 105 (2012) 196 - 201.

2. Background theory

2.1 Luminescence

The luminescence is the process of emission of light due to the chemical reactions, electrical energy, subatomic motions and stress on a lattice [1,2]. This process is whereby electrons in phosphor material decays radiatively from a higher energy state to a lower energy state with the difference in energy released as photons. In addition, for this process to take place the electrons needs to be excited to the higher energy level (absorption) by energy from the external source. The electrons decay to the ground state with two paths either radiative or non-radiative as shown in figure 2.1. The radiative relaxation is when excited electron decays to the ground state by emitting photons in a form of light. The radiative decay results in a spontaneous luminescence from phosphor materials and such luminescence may results from band edge or near band edge transitions, or from defect and/or activator quantum states as illustrated in figure 2.1. The non-radiative relaxation is when excited electron returns to the ground state by emitting phonons (heat). The process of non-radiative relaxation in phosphor applications it is not good because it suppresses the light generation efficiency and increases the heat losses. Therefore, it is very important to consider a material with a low phonon frequency to prepare a light emitting phosphors material [3]. There are many different types of luminescence existing such as photoluminescence (PL), cathodoluminescence (CL), thermoluminescence (TL), and electroluminescence (EL). The difference between them depends on the prefix name which indicates the type of excitation source (eg. catho- , thermo- , electro- and photo-).

2.2 Photoluminescence

Photoluminescence is the process when the phosphor material absorbs electromagnetic radiation particularly photons and therefore, an electron may be excited to a higher energy quantum state and the excited electron returns to a lower energy quantum state by emission of a photon. In general, the luminescence from the rare-earths (REs) doped phosphors begins with the absorption of photons on 4f-4f transition. The emission of a photon in solid/phosphor material occurs at lower energy than the absorbed energy of the photons due to the vibrational levels in the excited state. This phenomenon is known to be Stoke’s shift and the emitted photon is red-shifted relative to the absorption/excitation photon wavelength (as shown in figure 2.2). The process of photoluminescence exists in two different forms namely: fluorescence and phosphorescence. In fluorescence luminescence the emission stops after the excitation source stops while in phosphorescence luminescence the light emission continues for several seconds even after the excitation source has stopped. Fluorescence depicts short radiative relaxation lifetimes (10^{-9} – 10^{-5} s) while phosphorescence exhibits a relative long radiative relaxation lifetimes with (> 10^{-5} s) [4].

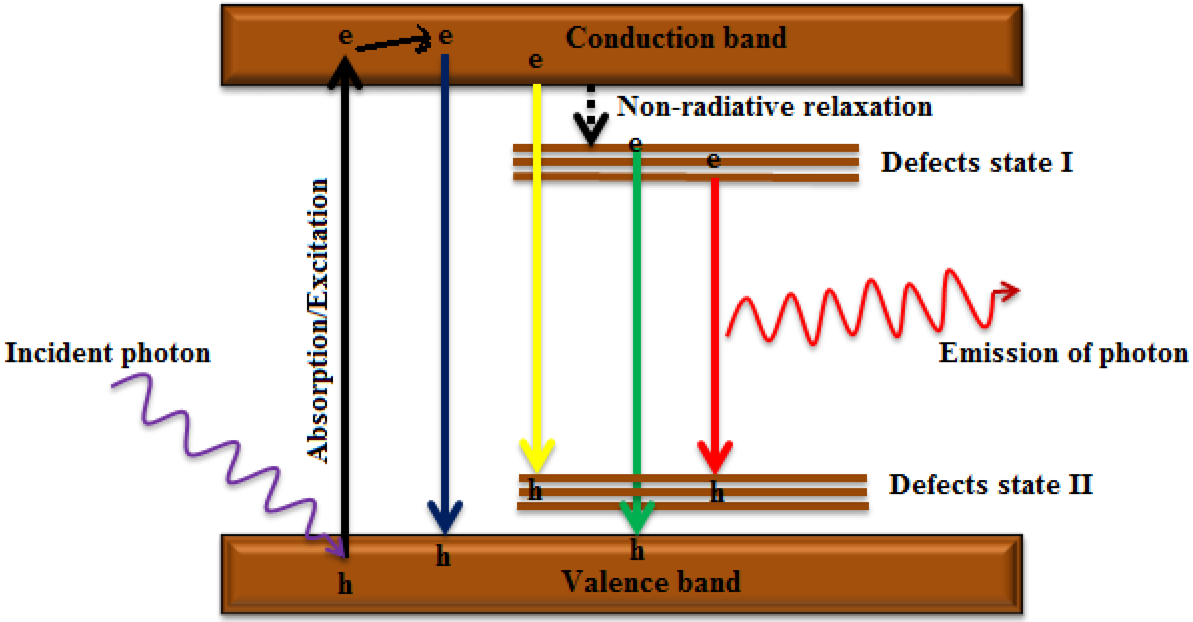

Figure 2.1: A radiative and non-radiative process that can occur during luminescence. (e - electron and h - hole)

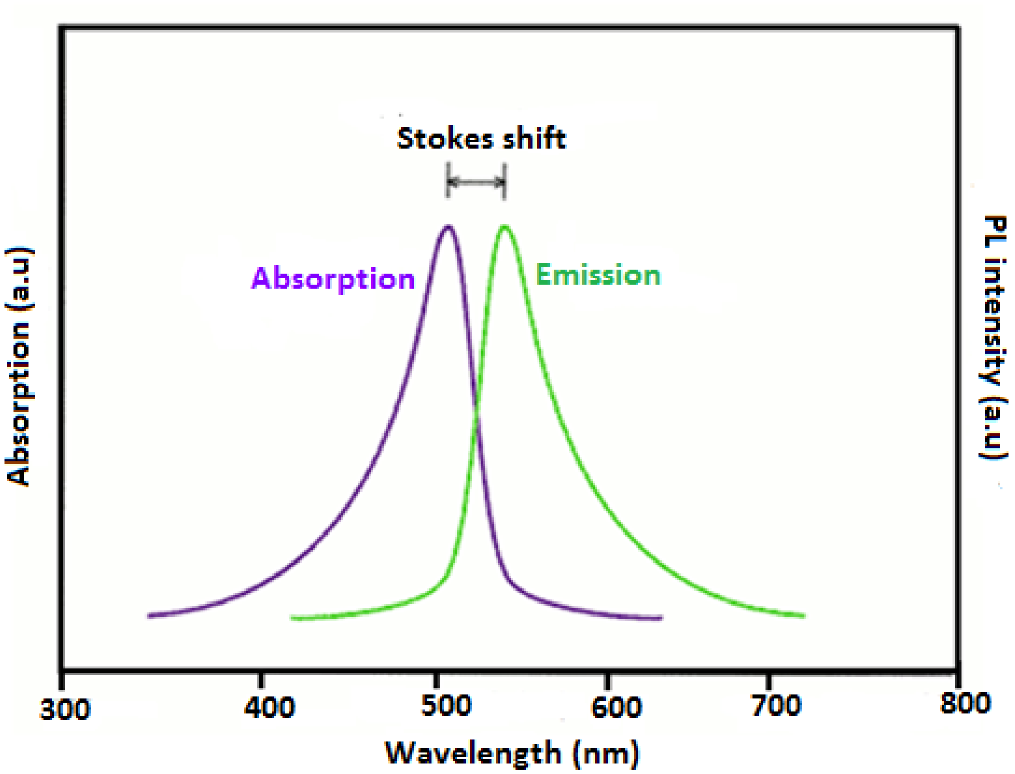

Figure 2.2: The absorption and emission spectra exhibiting Stokes shift.

2.3 Up-conversion process

Up-conversion (UC) process is a unique type of photoluminescence, in which the generation of high-energy photons (visible emission) it is induced by low energy excitation (near infrared photons) [5]. This process involves a sequential absorption of more than one lower energy photons and energy transfer (ET) between doping ions. This phenomenon was invented by Auzel in 1966 [6]. The UC process can be seen in rare-earths or transition metal ions incorporated into inorganic and organic host. The predominant mechanisms in UC phosphor based materials are excited state absorption (ESA), energy transfer up-conversion (ETU) and cooperative up-conversion (CUC) [7].

2.3.1 Excited state absorption

In ESA mechanism, excitation takes place in the form of sequential absorption of pump photons by a single ground state ion. The general energy diagram of ESA is depicted in (Fig. 2.3(a)) for a simple three-level system. The energy bandgap between the levels G and E1 is similar to that for the levels between E1 and E2. When the ion is excited from the ground state G to the intermediate state E1, a process it is called ground state absorption (GSA). The excited ion in E1 level has high chances of being pumped to the E2 level by pump photon because of the relatively long lifetime of the intermediate state E1 before its returns to the ground state. Eventually, the UC emission will occur from the E2 level. The selection of the dopants is very important in UC phosphors based materials because a ladder-like arrangement of the energy states of ions is needed [8].

2.3.2 Energy transfer up-conversion

ETU mechanism is quite the same with ESA. The ESA mechanism occurs within a single lanthanide ion, while ETU mechanism involves two neighboring lanthanide ions. In ETU, the sensitizer (ion 1) is first excited from its ground state G to its intermediate state E1 through the process of GSA. The sensitizer ion returns to the ground state G non-radiatively and transfer energy to the excited state E1 of the activator (ion 2). Therefore, exciting ion in an activator will be promoted to the upper emitting state E2 in a ladder-like until the excited ion in E2 returns back to the ground state G resulting in UC (Fig. 2.3(b)). The dopant concentration plays important role on the UC efficiency in this mechanism because it determines the average distance between the sensitizer and activator. Therefore, this mechanism is very sensitive to the dopants concentration [9]

The theory of energy transfer was proposed by Dexter and it has exposed that two luminescence centers, a sensitizer (Donor) and activator (Aceptor) within a certain distance, R with a certain interaction such as exchange or electric-multipole interaction may be in resonance and transfer energy from sensitizer to an activator. For near neighbouring ions (3 – 4 Å) the energy transfer is possible through the exchange interaction, while for interactions greater than (> 4 Å) the electric-multipole interaction takes place. The distance R between the two ions must be shorter than the critical distance R_c which is approximately twice the radius of a sphere. The critical distance R_c can be practically estimated by using the relation given by:

$$R_c = 2\left[\frac{3V}{2\pi X_c N}\right]^{1/3} \qquad (2.1)$$

Where X_c is the critical concentration, V is the volume of the unit cell and N is the number of cations per unit cell [10,11]

2.3.3 Cooperative up-conversion

CUC is a mechanism which involves the interaction among three ion centers, whereby ion 1 and ion 3 are assigned to be sensitizers in ETU process as shown in figure 2.3(c). The ion 1 and ion 3 can be excited to the intermediate state E1, then ion 1 and ion 3 will interact with an activator (ion 2) at the same time and excite ion 2 to its higher excited state E1. Finally, the ion 2 returns back to the ground state G displaying UC emission. The efficiency of CUC mechanism is lower than that of ESA and ETU processes, due to quasi-virtual pair levels during transitions which have to be described quantum mechanically in a higher order of perturbation [12].

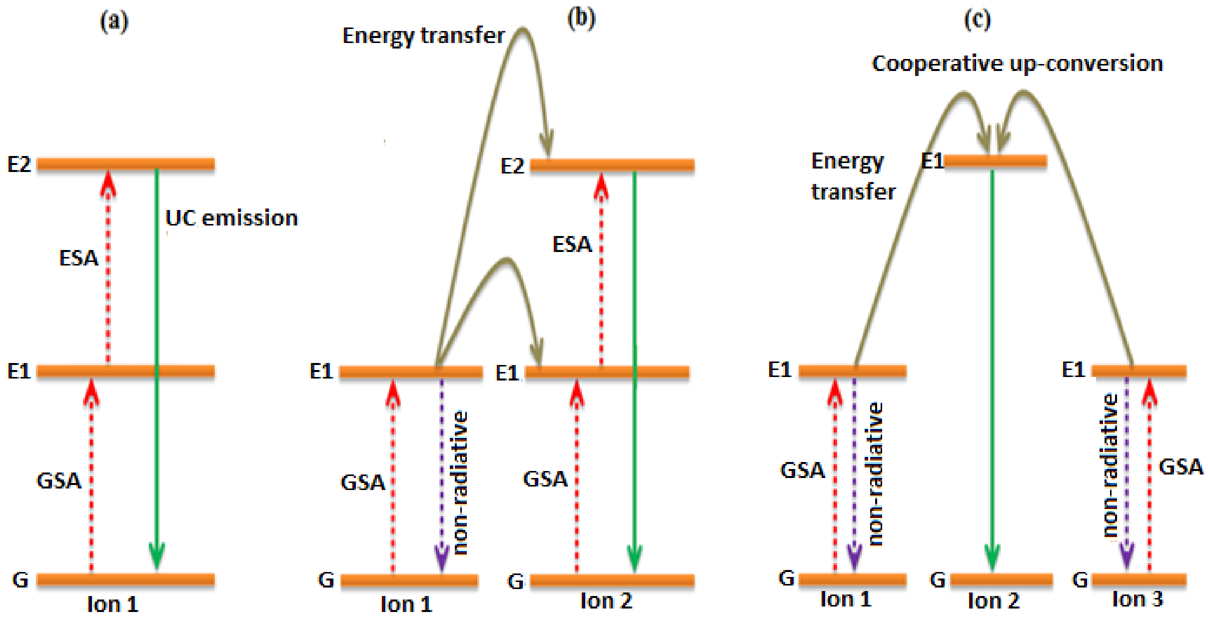

Figure 2.3: Schematic diagram of ESA mechanism in a three-energy level system (a), ETU mechanism between ion 1 (sensitizer) and ion 2 (activator) (b) and Cooperative up-conversion mechanism (c). (Red and violet dotted lines respectively represent photon excitation and non-radiative relaxation, brown curly arrows and green full arows represent energy transfer and UC photon emission, respectively).

2.4 The building blocks of up-conversion phosphors

The UC phosphors based nanomaterial is constructed with inorganic crystalline host matrix and dopant (emission centers). The dopant plays an important role of emission centers while the host matrix it brings these emission centers into optimal positions. The UC luminescence it is possible with one type of dopant ion but to achieve high UC efficiency two different types of ions are required. It has been mentioned previously that ETU is the most efficient UC process whereby two different types of ions as being sensitizer and activator interact. In this present study the sensitizer (Yb^{3+})/activator (Er^{3+} and Tm^{3+}) codoped Al_2O_3-TiO_2 UC phosphors were investigated. The trivalent Yb-Er and Yb-Tm pairs are chosen as dopant ions due to their tremendous properties which will be discussed in the following subsections [13].

2.4.1 Activator

An activator ion has to demonstrate the energy level structure with multiple long-lived excited states, with equidistant energy bandgap between excited states. The purpose of activator ion in UC process is to undergo a series of sequential excitation until the excited ion reaches a high-lying excited state where UC luminescence is produced. Most of the elements in the lanthanide group are considered as excellent activators because of their exceptional energy level structure. This electronic configuration $[Xe]4f^n6s^2$ is applicable for most lanthanides atoms such as erbium (^{68}Er) and thulium (^{69}Tm). In addition, most of the lanthanides atoms they exist as trivalent ions because of their oxidation state (3+). The lanthanides atoms display a sharp and narrow emission bands in near-infrared (NIR) and visible spectral region because of the f-f transitions. This happens because 4f electrons of lanthanide ions are shielded completely with filled $5s^2$ and $5p^6$ sub-shells. The f-f transitions are Laporte-forbidden, consequently resulting in low transition probabilities and substantially long-lived (up to 0.1 s) excited states and this seems to be an advantage for UC process. Therefore, Er^{3+} and Tm^{3+} ions are the most suitable activator ions in UC phosphors because of their ladder-like energy level that allows an efficient ETU process [13,14].

2.4.2 Sensitizer

In order to improve the efficiency of UC luminescence in phosphors material, a sensitizer with a large absorption cross-section in NIR spectral region is normally codoped along with an activator ion. In addition, one of the reasons by co-doping sensitizer along with an activator is to enhance the efficiency of ETU process between sensitizer and activator. Trivalent ytterbium (Yb^{3+}) ion is considered an excellent sensitizer with two manifolds ground ($^2F_{7/2}$) and excited ($^2F_{5/2}$) states with energy spacing of 10^4 cm^{-1} apart. This spacing apart of ground and excited states of Yb^{3+} ion matches well with the transition energy between the $^4I_{11/2}$ and $^4I_{15/2}$ states and the $^4F_{7/2}$ and $^4I_{11/2}$ states of Er^{3+} ion. The energy structure of Yb^{3+} is well resonant with the transition energies of the activators, eg. Er^{3+} and Tm^{3+} as shown in figure 2.4. Generally, Yb^{3+} ion is codoped into the host lattice in high concentrations (18 – 20 mol%), while the concentration of activator ions such as Tm^{3+} and Er^{3+} should not exceed 0.5 and 3 mol%, respectively [13,14].

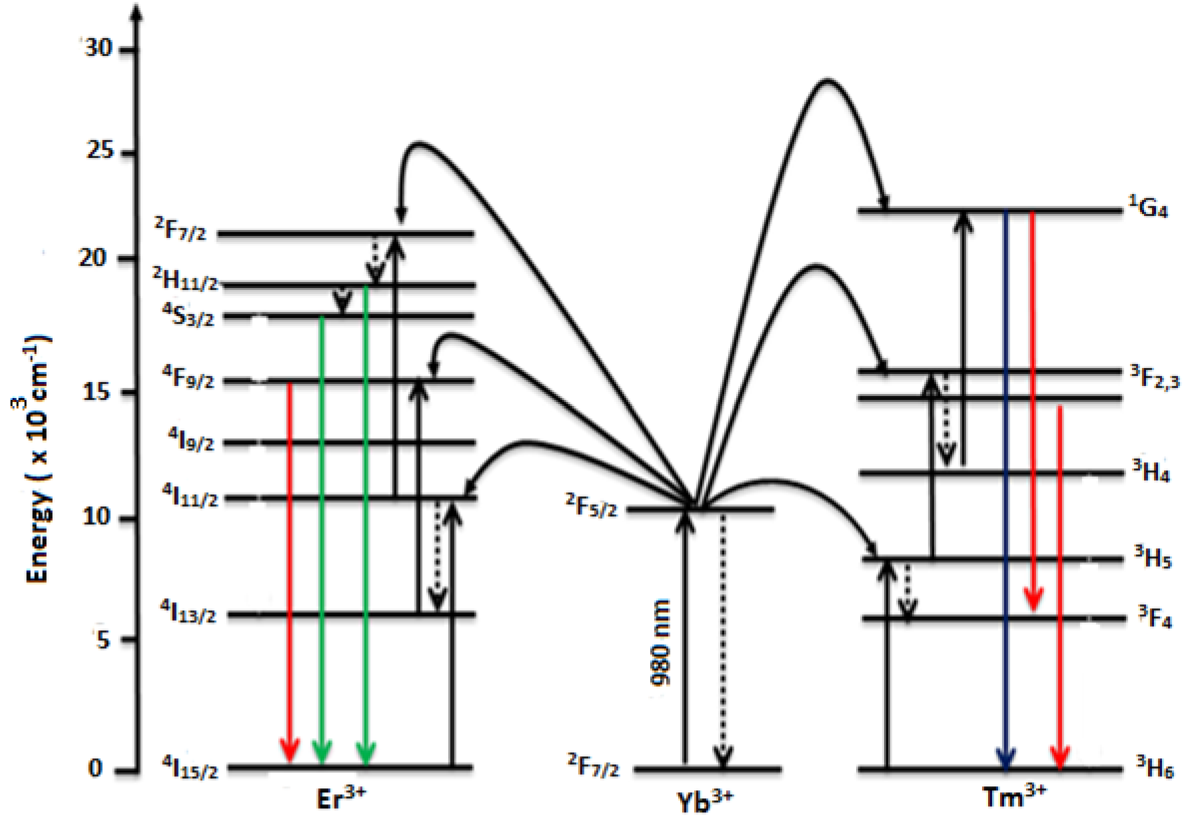

Figure 2.4: Schematic diagram of energy transfer mechanisms for UC process in trivalent pairs Yb-Er and Yb-Tm codoped phosphors under excitation of 980 nm. (The full arrows pointed up (Black) and down (Red, green and blue) represent photon excitation and emission, respectively. Square dotted lines (Black) and curly full arrows (Black) represent non-radiatively relaxation and energy transfer, respectively).

2.5 Quenching of Luminescence

Luminescent quenching refers to any process that reduces the luminescent intensity of a phosphor material. This process is caused by different factors including excess impurities in a material and heat exposed to the phosphor material i.e. concentration and thermal quenching. In this present study, the luminescence quenching shown was caused by an excess concentration of lanthanides ions in a host. The concentration quenching occurs at the critical concentration in which there is a decrease in the average distance between the ions (donor/sensitizer and acceptor/activator) to favour energy transfer. Thermal quenching occurs at elevated temperatures when the thermal vibrations of atoms surrounding luminescent centre transfer energy away from the center leading to a non-radiative recombination and a subsequent dissipation of the excess energy as phonons in the host matrix [15].

2.6 Host

The selection of appropriate host matrix has always been an important issue to design UC phosphor based nano-materials. The UC process depends on the properties of the host matrix and its interaction with the dopant ions. Because the lattice of the host matrix determines the inter-ionic distance between the dopant ions, their relative spatial position, coordination numbers and the types of anions surrounding the dopant. There are two important factors which are needed for an “ideal” host crystal: a relatively low phonon frequency and small lattice mismatch to the dopant ions. A low phonon frequency has a strong influence on the UC efficiency, in which it reduces a non-radiative relaxation and enhances the radiative relaxation. The halides host such as chlorides, bromides and iodides demonstrate a low phonon frequency typically ~300 cm^{-1} but they are hygroscopic, while oxides hosts generally exhibit a relatively high phonon frequency greater than (>500 cm^{-1}) with a good chemical stability. Nevertheless, the oxide based nano-composites material Al_2O_3-TiO_2 is yet considered as one of the most suitable matrix to host lanthanides ions to prepare phosphor materials [8].

2.6.1 Al_2O_3

Alumina (Al_2O_3) ceramic oxide is one of the most useful host lattice for rare-earth ions to prepare light emitting materials. It has got tremendous properties such as relatively high melting point (2072 ^{o}C), hydrophobicity, good chemical stability, high optical transparency, good thermal and mechanical stability, and fine optical and dielectric characteristic [16,17]. There are different phases of alumina which are α, β, γ, η, θ, κ and χ. The phase α-Al_2O_3 is considered as the most thermodynamically stable at 1200 °C while others are metastable phase obtained during the calcination of aluminium hydroxides (AlO(OH) or $Al(OH)_3$) as shown in figure 2.5 [18]. The phase α-Al_2O_3 is called corundum. In this structure Al atom is octahedrally coordinated with oxygen atoms as illustrated in figure 2.6 and the crystal structure was drawn by Diamond crystal software [19]. The structure can be seen as hexagonal close-packed (HCP) oxygen atoms with small Al atoms occupying two-thirds of the octahedrally coordinated holes between the oxygen atoms. The dimensions of unit cell are: $a = b = 4.7588$ Å and $c = 12.992$ Å [20].

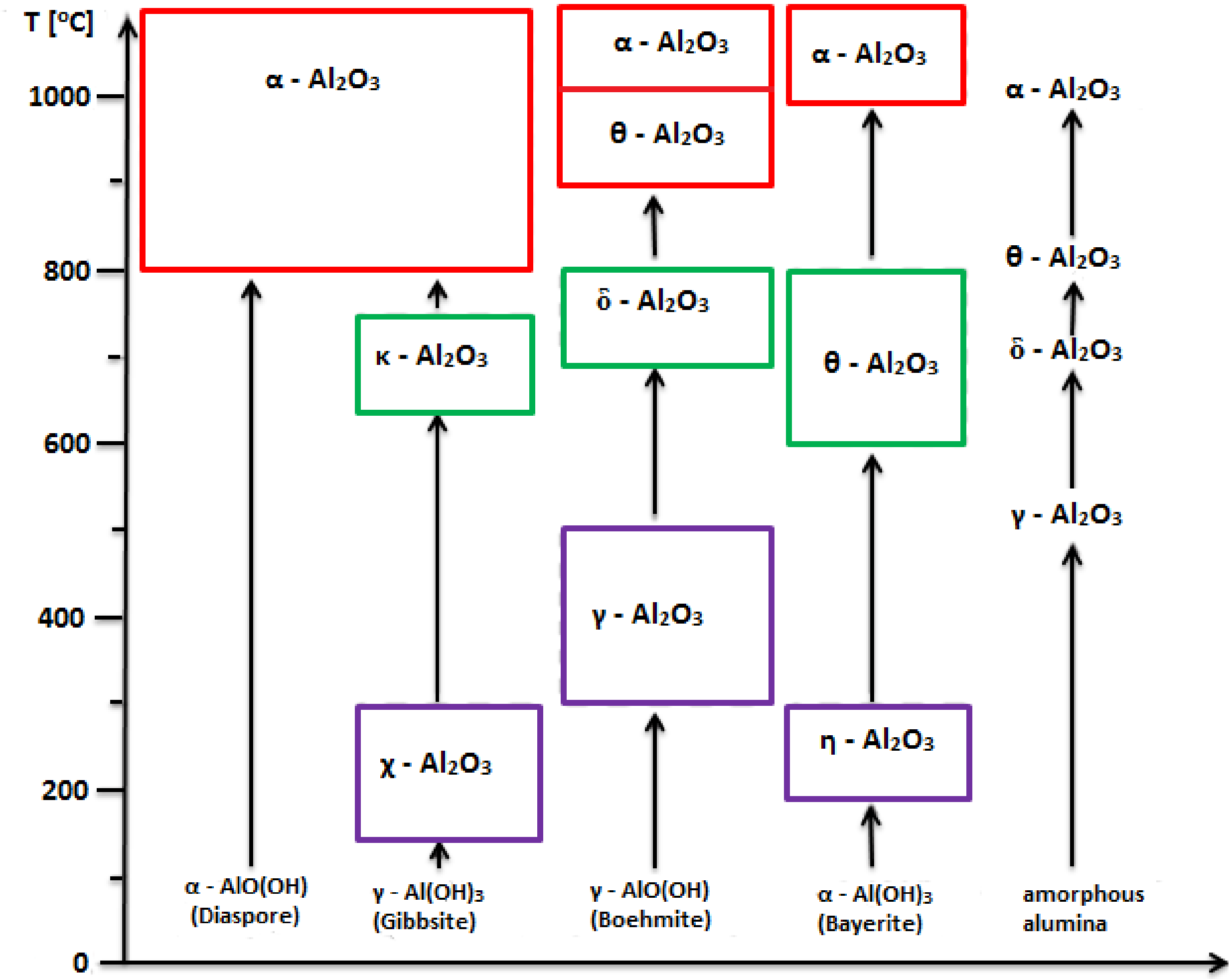

Figure 2.5: Phase transitions of aluminium oxide at different temperatures [20].

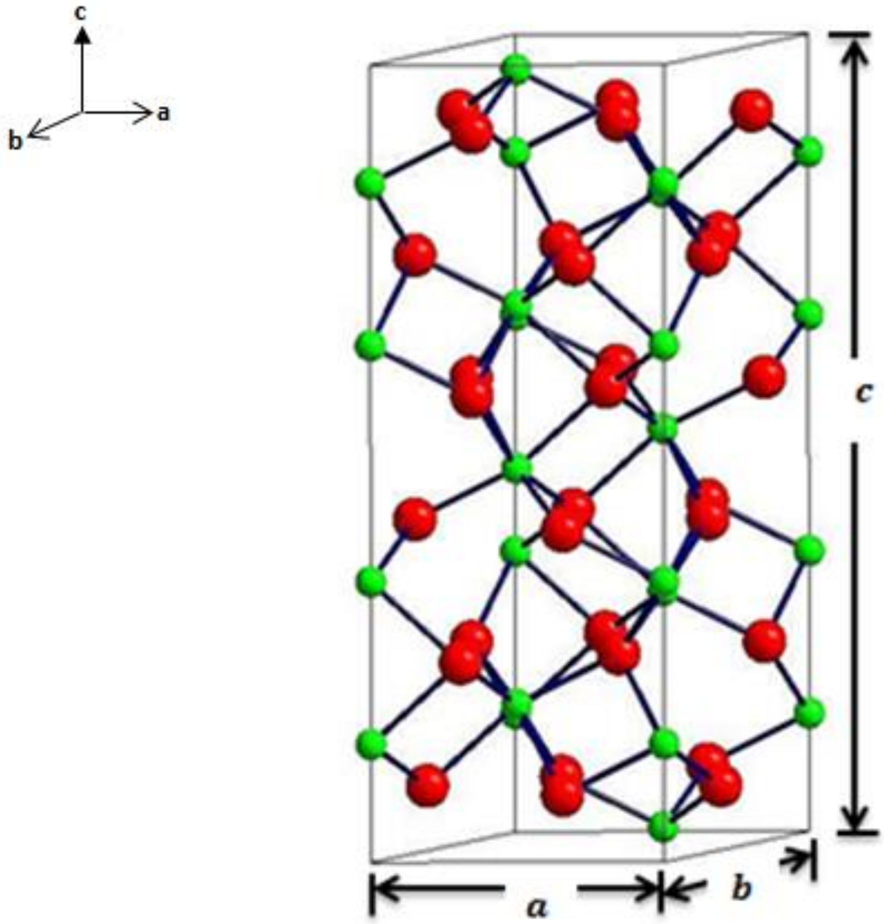

Figure 2.6: Crystal structure of corundum α – Al_2O_3. (Al atoms - green spheres and O atoms – red spheres) [21].

2.6.2 TiO_2

Titania (TiO_2) is one of the suitable host of rare-earths ions especially for UC phosphors because of its good physical and chemical stability, non-toxicity, anti-corrosiveness and wide bandgap [22]. The anatase and rutile phase exhibits an indirect bandgap of 3.2 eV and 3.0 eV, respectively [23]. There are three polymorphs of TiO_2, namely brookite, anatase and rutile. The anatase phase of TiO_2 has potential applications in gas sensors, catalysts and it can also be used for pigments because of its excellent chemical and physical properties [24]. The rutile phase is thermodynamically stable at high temperatures between 600 - 1000 ^{o}C. Therefore, the rutile phase it allows the TiO_2 to operate at unpleasantly environment. The brookite phase is commercially hardly used and its mechanical properties are very identical to those of rutile phase. Normally, addition of dopants changes some of the properties of the host (TiO_2) for example it is altering optical bandgap, electrical resistivity and inhibit particle growth. In addition, the doping of rare-earths in TiO_2 inhibits the phase transformation of anatase-rutile phase by stabilizing the anatase phase. Rao et al. [25] suggested that all dopants in TiO_2, both donor and acceptor cations and anions dopants, prevent the anatase-rutile phase transformation by stabilizing the anatase phase of TiO_2. The tetragonal crystal structures of anatase (a) and rutile (b) phase of TiO_2 are shown in figure 2.7. Both crystal structures consist of octahedron TiO_6. In anatase phase the Ti-O octahedra share four corners (Fig. 2.8(a)), while in rutile phase the Ti-O octahedra share four edges (Fig. 2.8(b)). The theoretical dimensions of anatase unit cell are: $a = b = 0.3872\,nm$ and $c = 0.9616\,nm$, while for rutile unit cell are : $a = b = 0.4594\,nm$ and $c = 0.2959\,nm$ [26].

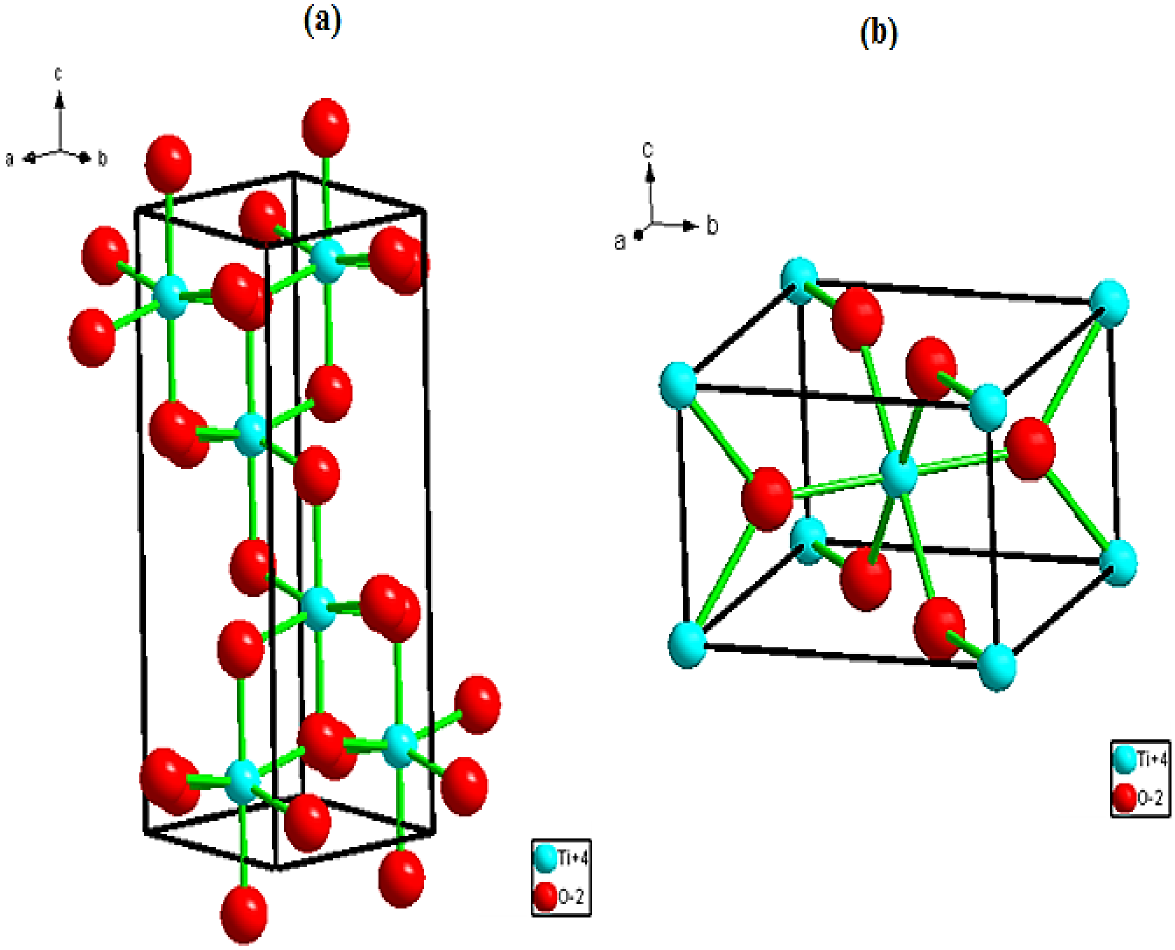

Figure 2.7: Tetragonal crystal structure of anatase (a) and rutile (b) phase in TiO_2 [21].

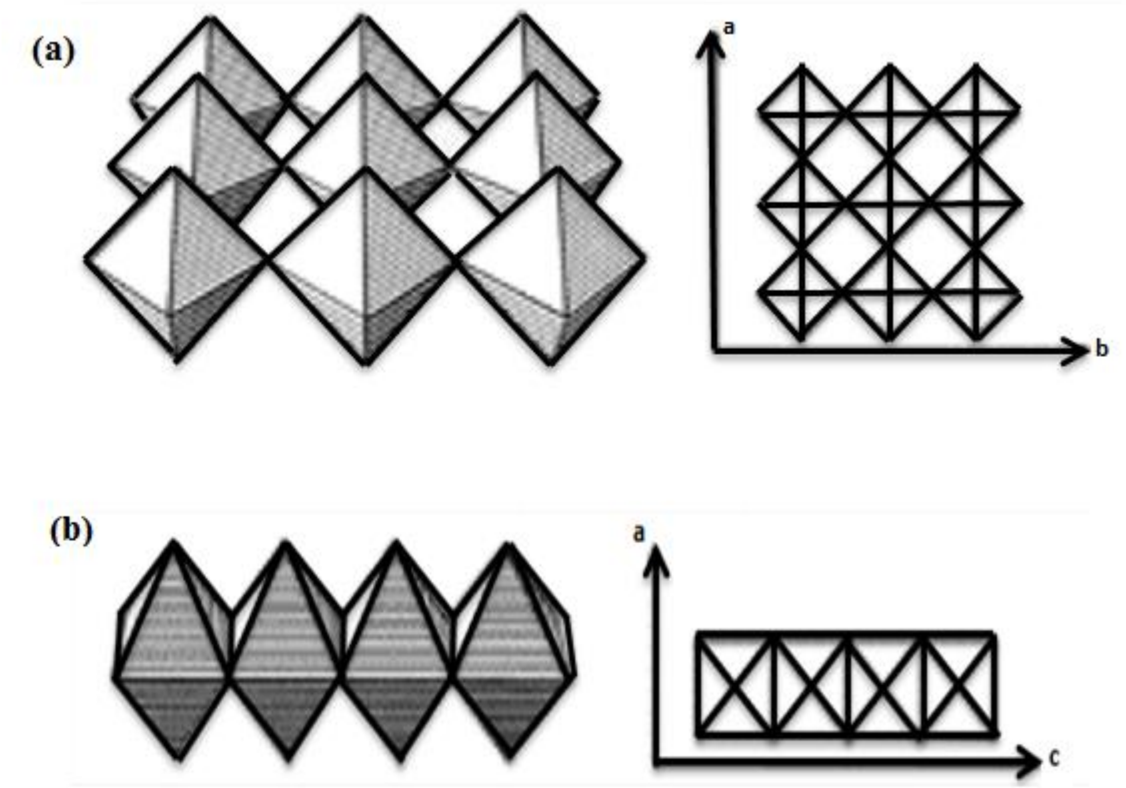

Figure 2.8: A schematic diagrams of anatase (a) and rutile (b) crystal structure [26].

2.6.3 Al_2O_3-TiO_2 nano-composites

Recently, the field of nano-composite materials has shown great attention in various applications due to the tremendous properties. The nano-composite is formed by using more than one building block with dimensions in less than (< 100 nm) in order to design and create new product with novel and improvements in their physical and chemical properties. Alumina-titania (Al_2O_3-TiO_2) is one of the most useful nano-composites to host UC rare-earth ions such as Yb^{3+}, Er^{3+} and Tm^{3+} to prepare light emitting phosphors. These nano-composites have shown great interest in physical properties protected metallic structural components against wear and corrosion because of their excellent thermal, chemical and mechanical stability. In addition, the nano-composites can be used in different applications including catalysis, photocatalytic, solar cells and self-cleaning. Many methods have been employed to synthesis Al_2O_3-TiO_2 nano-composites including sol-gel synthesis, coprecipitation method, plasma-sprayed method, hydrothermal synthesis, metalorganic chemical vapour deposition (MOCVD), spin coating method and microwave-combustion synthesis. The advantage of sol-gel synthesis is to control the crystallite size of nano-composites which is very important for nano systems. In addition, the method is cost-effective, good compositional control and low crystallization temperature [27-29].

2.7 Applications of UC phosphors

There are numerous applications of UC phosphors including photonics, frequency up-converters, biological fluorescence labels, undersea optical communications, solar cells and temperature sensors. The main focus in our present study has been involved in the development of UC phosphor which will be suitable for enhancement efficiency of solar cells. The UC phosphors material of Yb^{3+} codoped with Er^{3+} are highly suitable for narrow bandgap crystalline-silicon (c-Si) solar cells, since they can convert long-wavelength (~ 980 nm) NIR into short-wavelength (800, 660 and 550 nm) NIR and visible emissions. This UC phosphor material can also be suitable in improving the efficiency of amorphous silicon (a-Si) solar cells, dye-sensitized solar cells (DSSC) and organic solar cells [6,8,16]. While the UC phosphor material of Yb^{3+} codoped with Tm^{3+} are highly suitable in biomedical imaging applications, since they can convert long-wavelength (~ 980 nm) into short-wavelength (805, 642, 476 and 452 nm) NIR and visible emissions. The “optical window” is a NIR emission found in spectral region of 650 – 1350 nm and it’s where a light has a maximum length of penetration in biological tissues. In addition, this optical window is very important for the deep tissue imaging of UC fluorescent labels [30,31].

2.8 Reference

[1]. G.H. Mhlongo, K.T. Hillie, O.M. Ntwaeaborwa, Luminescence investigation of trivalent rare-earth ions in sol-gel derived SiO_2 and ZnO codoped SiO_2:Pr^{3+}, PhD Thesis, (2011), University of the Free State, Bloemfontein, South Africa.

[2]. https://en.wikipedia.org/wiki/Luminescence. [Last accessed 09 November 2015].

[3]. A. Kitai, Luminescent Materials and Applications, (2008), John Wiley & Sons, Chichester, England, page 30.

[4]. F.V. Molefe, L.F. Koao, B.F. Dejene, H.C. Swart, Novel ZnO Nanostructures: Synthesis, Growth Mechanism and Applications, MSc Thesis, (2014), University of the Free State, Qwaqwa, South Africa.

[5]. A. Pandey, V.K. Rai, V. Kumar, V. Kumar, H.C. Swart, Sensors and Actuators B, 209 (2015) 352 - 358.

[6]. N. Dyck, G.P. Demopoulos, F.C.J.M van Veggel, Spectral Engineering of Dye Sensitized Solar Cells Through Integration of $NaYF_4$:Yb^{3+},Er^{3+} Up-conversion Nano-materials, MEng Thesis, (2013), McGrill University, Montreal, Canada.

[7]. A. Patra, C.S. Friend, R. Kapoor, P.N. Prasad, Chemistry of Materials, 15 (2003) 3650 - 3655.

[8]. P. Ramasamy, P. Manivasakan, J. Kim, Royal Society of Chemistry Advances, 4 (2014) 34873 - 34895.

[9]. G. Dumlupinar, S.A, -Engels, H. Liu, Crystal Structure and Luminescence Studies of Up-converting Nanoparticles, MSc Thesis, (2015), Lund University, Lund Scania, Sweden.

[10]. N. Feng, Y. Tian, L. Wang, C. Cui, Q. Shi, P. Huang, Journal of Alloys and Compounds, 654 (2016) 133 - 139.

[11]. Y. Tian, B. Chen, X. Li, J. Zhang, B. Tian, J. Sun, L. Cheng, H. Zhong, H. Zhong, R. Hua, Journal of Solid State Chemistry, 196 (2012) 187 - 196.

[12]. F. Zhang, Photon Up-conversion Nano-materials, (2015), Springer-Verlag, Berlin Heidelberg, Germany, page 5 - 6.

[13]. F. Wang, X. Liu, Royal Society of Chemistry, (2009) 38 976 - 989.

[14]. J. Chen, J.X. Zhao, Sensors, 12 (2012) 2414 - 2435.

[15]. J.L. Ferrari, A.M. Pires, M.R. Davolos, Materials Chemistry and Physics, 113 (2009) 587 - 590.

[16]. D.M. Giolando, Solar Energy, 97 (2013) 195 - 199.

[17]. K. Laishram, R. Mann, N. Malhan, Ceramics International, 38 (2012) 1703 - 1706.

[18]. G. Rani, P.D. Sahare, International Journal of Applied Ceramics Technology, 12 (2015) 124 - 132.

[19]. Y. Wu, D.N. Ruzic, J.F. Stubbins, Deposition of aluminium oxide by evaporative coating at atmospheric pressure, MSc Thesis, (2013), University of Illinois at Urbana-Champaign, Illinois, Urbana.

[20]. A. Tougerti, C. Methivier, S. Cristol, F. Tielens, M. Che, X. Carrier, Physical Chemistry Chemical Physics, 13 (2011) 6531 - 6543.

[21]. K. Brandenburg, Diamond Version 3.0 d, (2005) Crystal Impact GbR, Bonn, Germany.

[22]. X. Meng, C. Han, F. Wu, J. Li, Journal of Alloys and Componds, 536 (2012) 210 - 213.

[23]. Z.P. Tshabalala, D.E. Motaung, G.H. Mhlongo, O.M. Ntwaeaborwa, Sensors and Actuators B: Chemical, 224 (2015) 841 - 856.

[24]. D. Dastan, N.B. Chaure, International Journal of Materials Mechanics and Manufacturing, 2 (2014) 21-23.

[25]. C. Rao, A. Turner, J. Honig, Journal of Physical Chemistry of Solids, 11 (1959) 173 - 175.

[26]. D.A.H. Hanaor, C.C. Sorrell, Journal of Material Science, 46 (2011) 855 - 874.

[27]. S.A.E. All, G.A.E. –Shobaky, Journal of Alloys and Compounds, 479 (2009) 91 - 96.

[28]. M.R. Mohammadi, Materials Science in Semiconductor Processing, 27 (2014) 711 - 718.

[29]. B. Dong, C.R. Li, M.K. Lei, Journal of Luminescence, 126 (2007) 441 - 446.

[30]. D.K. Chatterjee, M.K. Gnanasammandhan, Y. Zhang, Nano Small Micro, 6 (2010) 2781 - 2795.

[31]. J. Chang, Y. Liu, J. Li, S. Wu, W. Niu, S. Zhang, Journal of Materials Chemistry C, 1 (2013) 1168 - 1173.

3. Synthesis of nano-materials

3.1 Introduction

In order to study the novel physical and chemical properties, and notice the potential applications of nanostructures and nano-materials, the ability to manufacture and process nano-materials and nanostructures is the first corner stone in nanotechnology. The synthesis techniques for nano-materials are classified as "top-down" and "bottom-up" approach. Top-down approach includes solid state route while the bottom-up include wet chemical route like sol-gel, hydrothermal, microwave synthesis and co-precipitation. The top down approach involves the chopping of massive solid materials into tiny portions until achieving particles in the nanometer scale, and the bottom up approach involves condensation of atoms or molecules in a solution phase to form nanoparticles as shown in figure 3.1 [1].

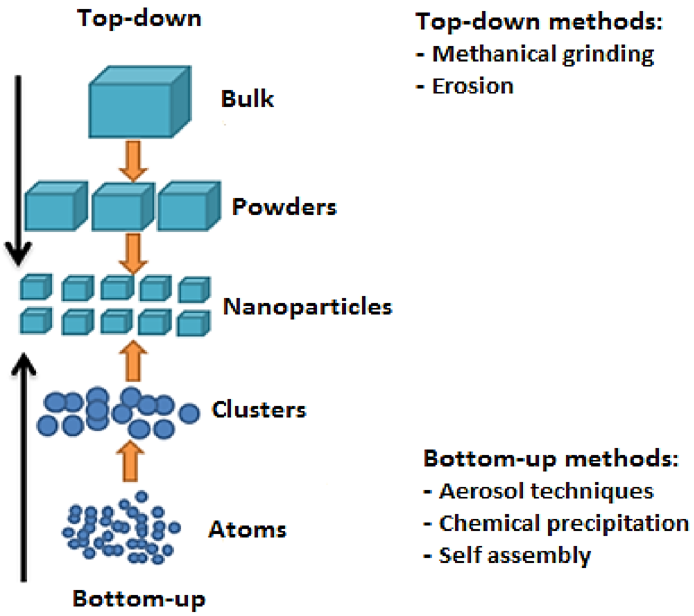

Figure 3.1: Schematic diagram of top-down and bottom-up method to prepare nanoparticles [2].

In this study, the bottom up approach was used a brief description of examples of this approach such as solution combustion and sol-gel synthesis are discussed in this chapter. The solution combustion synthesis was used to prepare the Al_2O_3:Yb^{3+} nano-phosphor while the sol-gel synthesis was used to prepare Al_2O_3:Yb^{3+},Tm^{3+}, TiO_2:Er^{3+} and Al_2O_3-TiO_2:Yb^{3+},Er^{3+}/Tm^{3+} powder nano-phosphors.

3.2 Solution combustion synthesis

The solution combustion synthesis (SCS) is one of the most efficiently method to prepare highly pure and homogeneous and mostly nanocrystalline powders such as ceramics oxides. In addition, the synthesis involves high temperatures making use of salts such as nitrates, metal sulphate and carbonates as oxidizers, and fuels such as glycine, sucrose, urea and other water soluble carbohydrates as reducing agents. The stoichiometric amounts or ratio between the oxidizer and fuel is required so that combustion reaction can take place. The typical example showing stoichiometric combustion reaction of aluminium nitrates nonahydrates ($Al(NO_3)_3{\cdot}9H_2O$) and urea ($CO(NH_2)_2$) yield Al_2O_3 nano-phosphor powder as shown below.

$$2Al(NO_3)_3{\cdot}9H_2O + 5CO(NH_2)_2 \rightarrow Al_2O_{3(s)} + 28H_2O_{(g)}\uparrow + 5CO_{2(g)}\uparrow + 8N_{2(g)}\uparrow.$$

When combustion reaction occurs, all gaseous form of nitrogen (N_2), carbon dioxide (CO_2) and water vapour (H_2O) are liberated, and there are residual or incidental impurities that is in the final Al_2O_3 nanopowder. Figure 3.2 shows a schematic diagram of the synthesis procedure of nanopowder. In this typical reaction, the stoichiometric amount of aluminium nitrate and urea were disolved in de-ionised water. A homogeneous transparent solution was obtained after stirring vigorously for 60 min. The transparent solution was transferred to a muffle furnace maintained at 550 ± 10 ^{o}C. After all the liquid had evaporated, the mixture decomposed and released large amounts of gases. Due to the exothermic nature of the combustion process, the reaction continued for a while and mixture swelled to a large volume. Large exothermicity resulted in a high temperature flame that further decomposed the mixture into gaseous phase and alumina. The combustion process was completed in less than 5 min. The resulting powder was gently ground by pestle motar. Al_2O_3:Yb^{3+} nano-phosphor powder with a concetrations of 0.4, 0.8 and 1.2 mol% Yb^{3+} were prepared. In addition, the temperature of 550 ± 10 ^{o}C is low relatively to the temperature at which crystallization of the fact that desired phase occurs because the Al_2O_3 becomes thermodynamically stable at 1200 ^{o}C.

There are some advantages to SCS, i.e. very quick and easy process. In addition, this process is widely used in the production of high purity, homogeneous ceramics powders because of the fact high temperature is used and impurities with low boiling points can be volatilize easily. Most of the gases evolved during the combustion process in a porous product in which the agglomerates formed are so weak that they can be easily crushed and ground into fine powder [3-5].

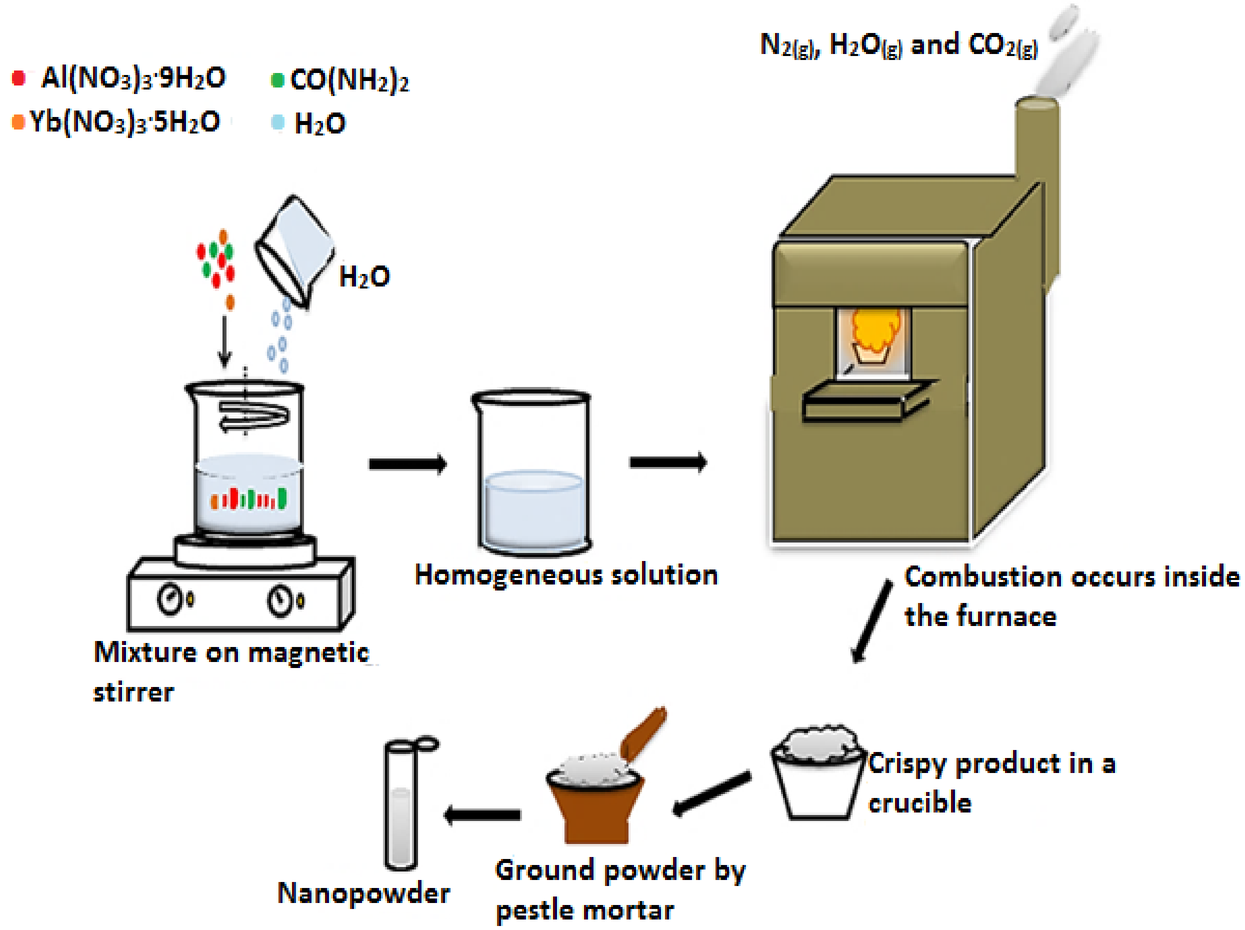

Figure 3.2: A schematic diagram of the synthesis procedure of nanopowder.

3.3 Sol-gel method

Sol-gel process is one of the most powerful synthesis techniques for producing nanoscale powders from small molecules. This process has been developed in recent years as an alternative to the conventional hydrolytic route to metal oxides, mainly the oxides of titanium (Ti), aluminium (Al) and silicon (Si) etc. The list of advantages to this synthesis method is endless, i.e. low cost simple synthetic route, low temperature synthesis, simple equipment to be used, control of the particle size and shape, homogeneous compositions, high purity and low heat treatment temperatures. In this typical process, a sol diffuses in a solvent by Brownian motion and is prepared by using metal precursors such as alkoxides, acetates or nitrates in an acidic or basic medium. The process involves three main steps which are hydrolysis, condensation (sol-formation) and growth (gel-formation) shown in figure 3.3. In addition, the metal precursors hydrolysis in the medium and condenses to form a sol, followed by a polymerization to form a network (gel) [4,6-9].

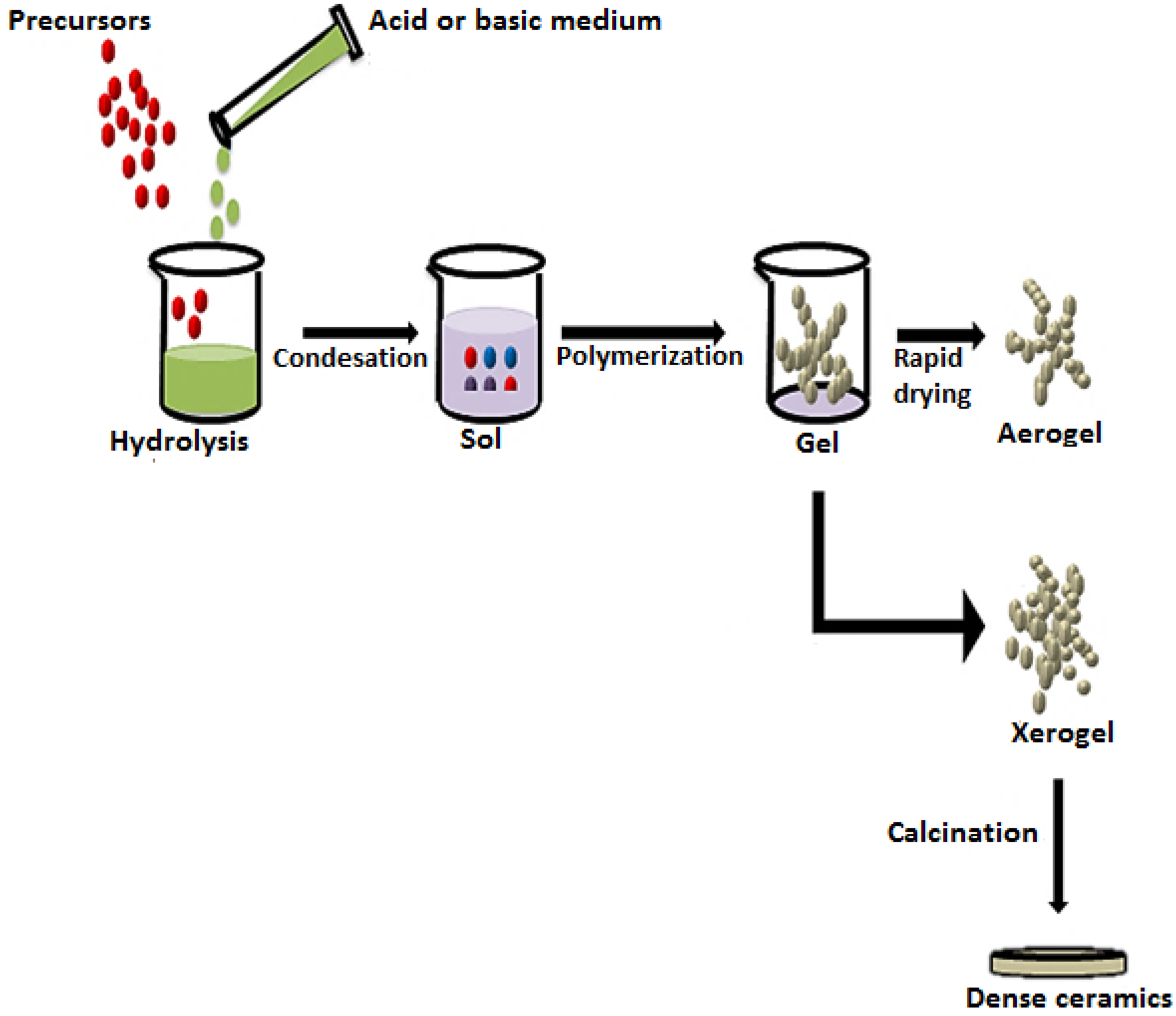

Figure 3.3: Schematic diagram of sol-gel process synthesis of nanopowders [4].

The sol-gel process is also useful in thin film deposition by use of spin coating though it was not a part of the scope in this work. Recently, many researchers have done so much work based on thin film deposition prepared by the sol-gel method. Tabaza et al. [6] synthesized $(Mg_xZn_{1-x})Al_2O_4$ phosphor thin films by using the sol-gel method . The composite of semiconductor TiO_2-Al_2O_3 thin film for application of gas sensors prepared by the sol-gel process was studied by

Mohammadi et al. [7]. In this study, Al_2O_3-TiO_2 nano-composite phosphors were prepared by the sol-gel method as depicted in figure 3.4.

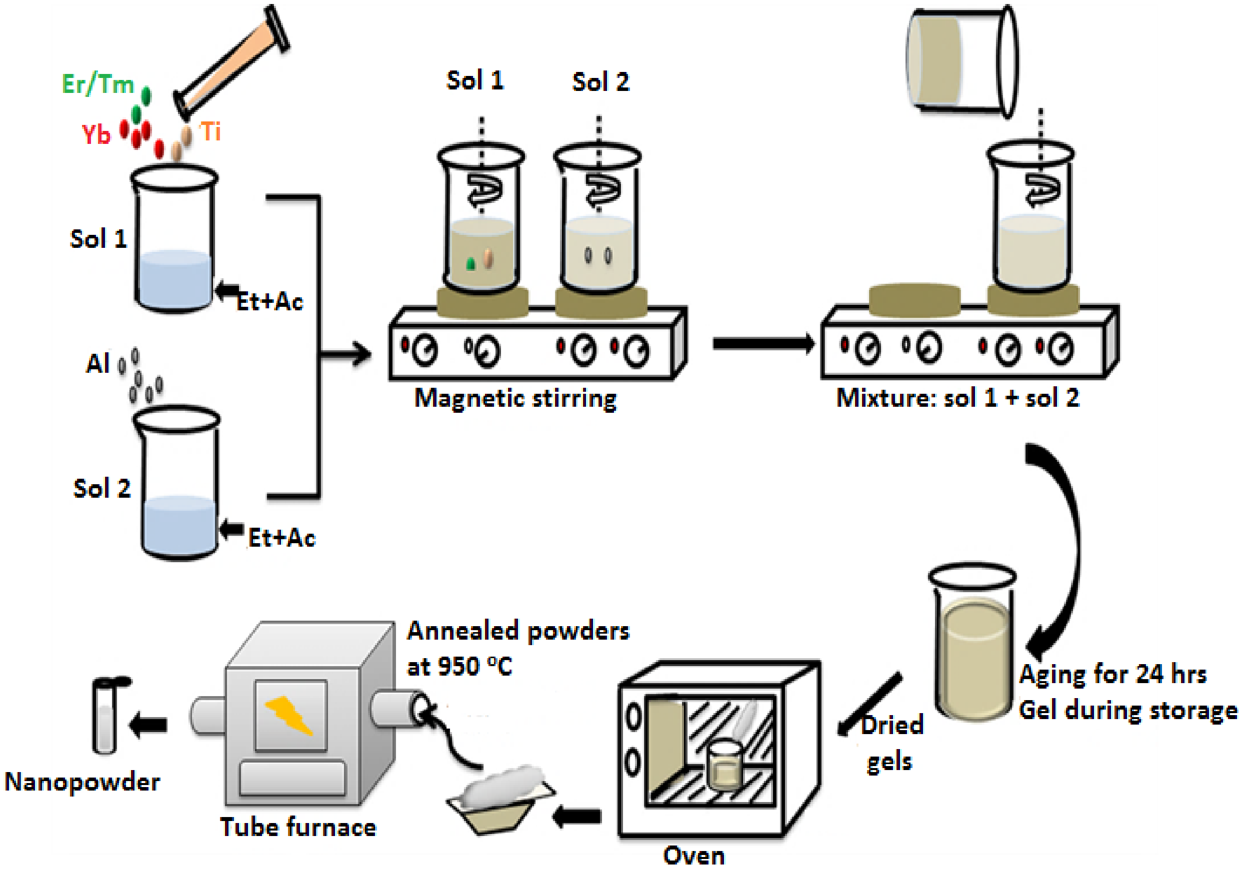

Figure 3.4: Schematic diagram of the synthesis procedure of Al_2O_3-TiO_2 nano-composite phosphor powder (Ti = titanium (IV) butoxide, Yb = ytterbium (III) acetate tetrahydrate, Er = erbium (III) acetate hydrate, Tm = thulium (III) acetate hydrate, Al = aluminium n-butoxide, Et = ethanol and Ac = acetic acid).

3.4 Reference

[1]. M.A. Shah, Nanotechnology applications for improvements in energy efficiency and environmental management, (2015), Information Science reference IGI Global, United States of America, page 1-8.

[2]. http://3p2-2012.wiki.hci.edu.sg/T1g+Nanotechnology. [Last accessed 25 August 2015].

[3]. S.T. Aruna, A.S Mukasyan, Current Opinion in Solid State and Material Science, 12 (2008) 44 - 50.

[4]. A. Kitai, Luminescent Materials and Applications, (2008), John Wiley & Sons, Chichester, England, page 40.

[5]. T. Mimani, K.C. Patil, Material physics and mechanics, 4 (2001) 134 - 137.

[6]. W.A.I. Tabaza, R.E. Kroon, H.C. Swart, Synthesis and characterization of $MgAl_2O_4$ and $(Mg_xZn_{1-x})Al_2O_4$ mixed spinel phosphors, PhD Thesis, (2014), University of the Free State, Bloemfontein, South Africa.

[7]. M.R. Mohammadi, Materials Science in Semiconductor Processing, 27 (2014) 711 - 718.

[8]. http://www.gitam.edu/eresource/nano/nanotechnology/nanotechnology%20web%201.htm. [Last accessed 21 August 2015].

[9]. A.K. Koloddziejczak-Radzimska, T Jesionowski, Materials, 7 (2014) 2833 - 2881.

4. Characterization techniques of nano-materials

4.1 Introduction

In this chapter, the experimental techniques that were used to characterize the nano-phosphor powders are explained in detail. These include powder x-ray diffraction (XRD), ultraviolet visible near infrared (UV-Vis-NIR) spectrophotometer, Fourier transform infrared (FTIR), Field emission scanning electron microscopy (FE-SEM), energy dispersive x-ray spectroscopy (EDS) and photoluminescence (PL) spectroscopy. XRD was used to analyse the crystal structure, the UV-Vis-NIR and FTIR were used to study the optical properties and vibrations for different types of functional bonds in a molecule, the FE-SEM coupled EDS was used to analyse particle morphology and chemical composition of the samples and the PL spectroscopy was used to study luminescent properties of the materials.

4.2 X-ray diffraction

X-ray diffraction (XRD) is a powerful technique used to identify structural properties, degree of crystallinity, phase identification, lattice parameters and crystallite size. The instrumentation made up of three essential elements: x-ray source, a sample stage and an x-ray detector. The x-rays are produced in a cathode ray tube by applying high voltage in a filament in order to produce electrons, which are accelerated to the target. The most commonly used target materials are copper (Cu), iron (Fe), molybdenum (Mo) and chromium (Cr). Suppose the incident electrons have high energy to knock-off the electrons in a core shell of a target, therefore characteristic x-rays will be produced additionally to continuous x-ray background which is called “brehmsstrahlung” [1]. The characteristics x-ray spectrum consist various components; K_α and K_β are considered as the most significant components with a unique characteristic wavelength, hence are called “characteristic x-rays”. However, amongst the entire target materials Cu is the most preferable target for crystal diffraction, with the wavelength of Cu K_α radiation of 1.5406 Å. The process of monochromatization of single wavelength from x-ray spectrum was done by employing nickel (Ni) in order to filter K_β radiation because Ni strongly absorbs x-rays below 1.5 Å [2,3].

The interaction of an incident x-rays with a single crystal produces constructive interference from parallel planes if conditions for Bragg's law is satisfied as illustrated in figure 4.1:

$$n\lambda = 2dsin\theta \tag{4.1}$$

where *n* is integer multiple or (order of diffraction), λ wavelength of the radiation source, *d* interplanar spacing and θ incident angle with the planes [4]. The crystallographic planes are very useful in crystal in order to define direction and distance, and identified by Miller indices *(hkl)*, and for cubic crystal with a lattice parameter a, the interplanar corresponding to a specific *(hkl)* can be represented by d_{hkl}:

$$d_{hkl} = \frac{a}{\sqrt{h^2+k^2+l^2}} \tag{4.2}$$

The average crystallite size *D* can be determined from the broadened peaks of the XRD spectrum by using Debye-Scherrer equation:

$$D = \frac{k\lambda}{\beta cos\theta} \tag{4.3}$$

where *k* is dimensionless shape factor has typical value of ~ 0.9 but that varies with actual shape of crystalline, β is a full width at half maximum (FWHM) of diffraction at an angle θ, and λ is a diffraction wavelength of radiation source. The line width is narrow as the size of nanocrystalline is large, and as the size decreases the line width is broadened due to the loss long range order relative to the bulk [5]. In some case broadening may be due to micro-stains and stress in a lattice as a results of crystal imperfection and distortion. The micro-strain ε can be estimated by:

$$\varepsilon = \frac{\beta}{4tan\theta} \tag{4.4}$$

The Williamson-Hall (W-H) equation is used to determine the crystallite sizes and micro-strains in lattices. The W-H equation is computed by adding broadening due to micro-strains (β_s) and Debye-Scherrer (β_D) from equation 4.4 and 4.3, respectively.

$$\beta = \beta_s + \beta_D \tag{4.5}$$

$$\beta cos\theta = 4\varepsilon sin\theta + \frac{k\lambda}{D} \tag{4.6}$$

The plot of *4sinθ* along x-axis and *βcosθ* in y-axis shows linear behaviour, micro-strain and crystallite size can be estimated from the slope and y-intercept, respectively [6].

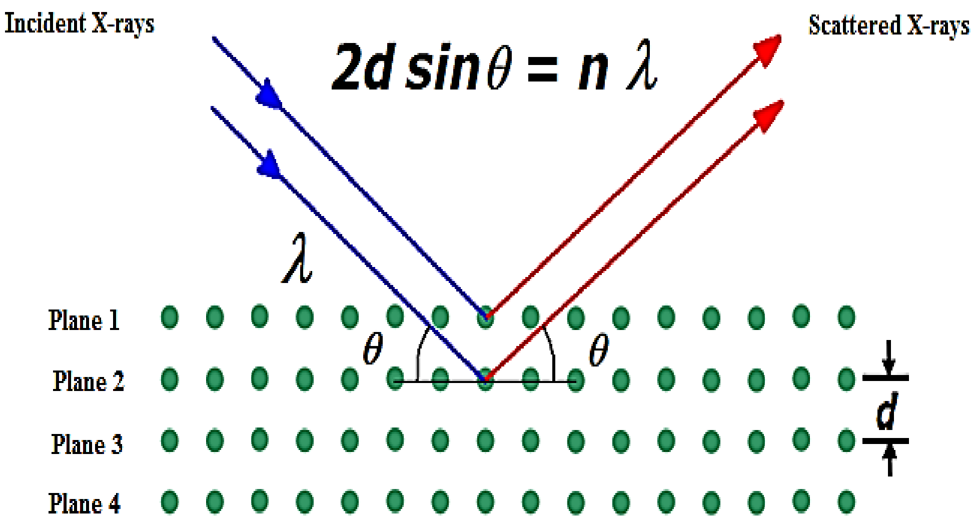

Figure 4.1: Schematic diagram for Bragg's law conditions [5].

The intensity of the reflected x-rays is recorded as the sample and detector are rotated simultaneously. When the incident x-rays interact with a sample satisfies Bragg's condition constructive interference occurs and diffraction peaks will be observed on the machine. The spectrum on the computer will be recorded as *2θ* in degrees and intensity in counts per seconds along x-axis and y-axis, respectively. In this study, the XRD measurements were conducted using Bruker D8 Advance x-ray diffractometer with a copper anode x-ray tube.

4.3 UV-Vis-NIR spectrophotometer

Ultraviolet-visible-near infrared (UV-Vis-NIR) spectrophotometer is a technique that is used to measures the absorption and reflectance of radiation in UV-Vis-NIR spectral region. This is one of the most important spectroscopy to study the behaviour of the nano-phosphor materials under a light irradiation because of the fact that a material has capability to absorb and reflect when they interact with light. The spectroscopy measures intensity (I) of light that is absorbed by the sample and compares it with the intensity of light before it passes through the reference (I_o). The transmittance (T) is the ratio of I/I_o and it is normally expressed as a percentage ($\%T$). The relationship between absorbance (A) and T is defined by the following equation:

$$A = -log\left(\frac{\%T}{100}\right) \tag{4.7}$$

In a reflectance mode, the spectroscopy measures the intensity of the light reflected from the sample (I) and compares it with the intensity of the light reflected from a reference material (I_o). The reflectance (R) is the ratio of I/I_o and it is normally expressed as a percentage ($\%R$). The instrumentation of the spectroscopy consists of a source, monochromator, beam splitter, sample compartment and detectors, as shown in figure 4.2. The source it covers in a ranges of (200-400 nm) and (320-2500 nm) spectral region corresponding to deuterium (D) and tungsten (W) lamps, respectively. The light with variety of wavelength will passes through the slit and reaches a prism which will refract rainbow colours. However, only a monochromatic beam will passes through a second slit and that beam will strikes a beam splitter, and becoming two beams with the same intensities. These beams with the same intensities are directed towards the reference and sample cell, the outgoing intensities corresponding to I_o and I, respectively and will be detected by two similar detectors. The detectors used in this spectroscopy are photomultiplier tube (PMT) and lead sulphide (PbS) measuring UV to visible and NIR region, respectively [1,7-9].

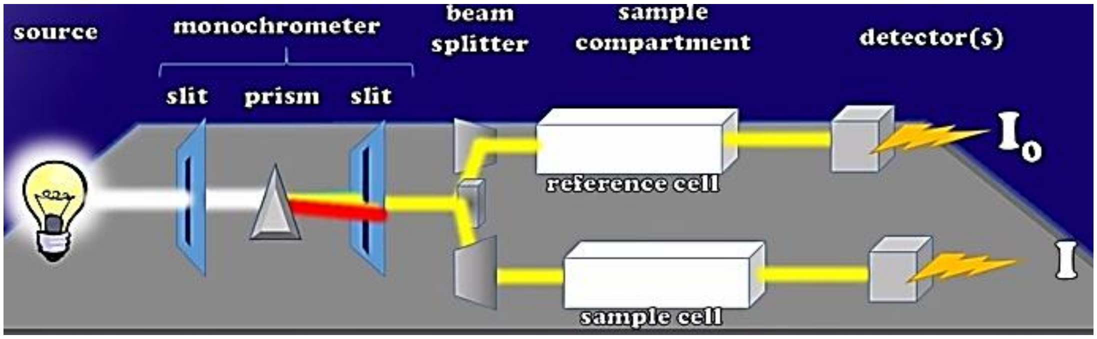

Figure 4.2: Schematic diagram of UV-Vis-NIR spectrophotometer [9].

In semiconductors the optical bandgap (E_g) is determined by Tauc's plot method with the aid of the following equation:

$$\alpha hv = A\left(hv - E_g\right)^n \tag{4.8}$$

where α is the absorption coefficient, h is Planck's constant, v is the frequency of the incident photons, A is a constant which is dependent on the effective mass of the holes and electrons, and also to the refractive index of the material but is independent of the frequency, and n denotes the type of the transition in a sample. The value of exponent *n* for allowed direct, allowed indirect, forbidden direct and forbidden indirect transitions are 1/2, 2, 3/2 and 3, respectively [2,11,12]. The diffuse reflectance measurements for this study were performed by using the Perkin Elmer Lambda 950 UV-Vis-NIR spectrophotometer.

4.4 Fourier Transform Infrared Spectroscopy

Fourier transform infrared (FTIR) is a spectroscopic technique that is widely used to observe the vibrations of molecular bonds, and gives information about the nature of the bonding and the functional groups in a molecule. Infrared (IR) photons do not have sufficient energies to cause electronic transitions but they can cause vibrations to a group of atoms with respect to the attached bonds. In addition, these vibrational transitions correspond to different energies and molecules absorb IR radiations only at certain wavelength and frequencies [13]. For a molecule to have IR absorptions needs to have dipole moments and therefore it is assigned to be IR-active. The part of IR spectrum in a range from 600 to 1400 cm^{-1} is where many complex vibrations occur and it is called "fingerprint region" because every compound is unique, there is no two different compounds have the same absorption bands in this region. The Michelson interferometer is the most useful principle in FTIR spectrometers as shown in figure 4.3.

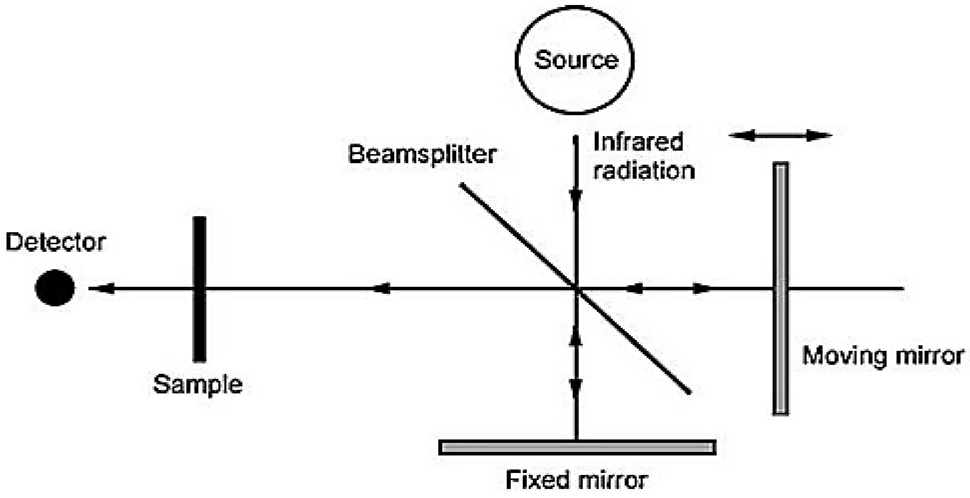

Figure 4.3: Schematic diagram of an FTIR spectrometer [15].

The instrumentation of FTIR spectroscopy consists of a source of IR radiation, interferometer, sample compartment, detector, amplifier, analog-to-digital (A/D) converter and a computer. The source produces radiation which passes the sample through the interferometer and get to the detector. Afterwards the signal is amplified and converted to digital signal by A/D converter. Then the signal is relayed to a computer in which the Fourier transform is also carried out. Eventually, the spectrum will show the plot of transmittance along y-axis as a function of wavenumbers along x-axis. The spectroscopy can be conducted in two modes, namely absorbance and transmittance [14,15]. In this study, the types of functional bonds were characterized by using Bruker TENSOR 27 Series FTIR spectrometer.

4.5 Field emission scanning electron microscope

Field emission scanning electron microscope (FE-SEM) is one of the most powerful electron microscope that is used to study the morphology and surface features of materials. The electron microscope inspect the structure by scanning in a raster pattern to the surface of materials with a resolution down to nanometer range. In FE-SEM, accelerated electrons carry significant amounts of kinetic energy and this energy is dissipated as a variety of signals produced by electron-sample interactions when the incident electrons are decelarated in the solid samples. In addition, there are variety of signals can be produced such as secondary electrons (SE), backscattered electrons (BSE), auger electrons and x-rays but amongst them SE, BSE and characteristic x-rays are considered as the most important signals for topographical, compositional observations in a surface and elemental analysis of specimen, respectively as shown in figure 4.4 [2].

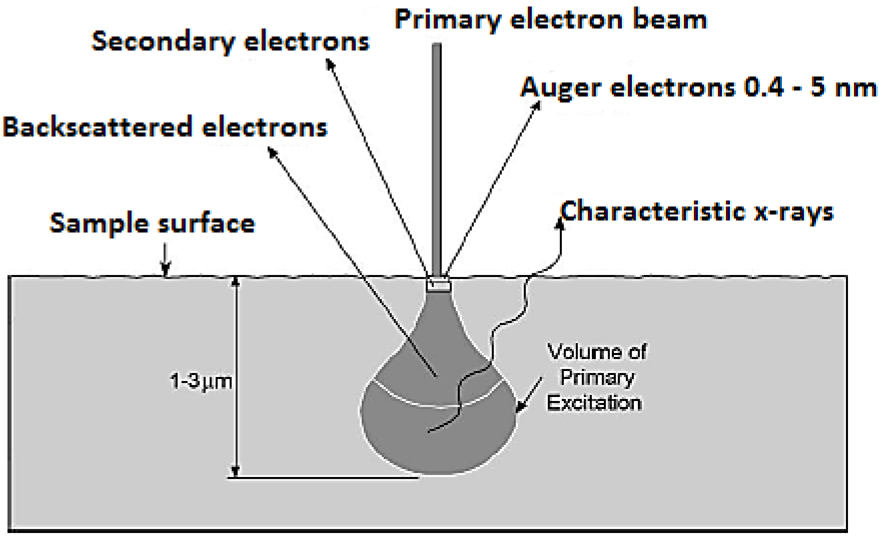

Figure 4.4: Interaction volume showing variety of signals when incident electron beam interact with a sample [2].

In this study, the particle morphology and elemental identification analyses in a specimen were carried out using JEOL JSM-7800 FE-SEM. The instrumentation of FE-SEM consists of an electron gun, a column through which electron beam travels, a series of electromagnetic lenses including condenser lenses and objective lens to shape the electron beam, the sample chamber at the base and a series of pumps to keep the system under vacuum as shown in figure 4.5. There are two types of electron guns that generate electron beam and those guns are thermionic and field emission guns because of their high beam brightness which plays crucial part in imaging quality in an FE-SEM [16].

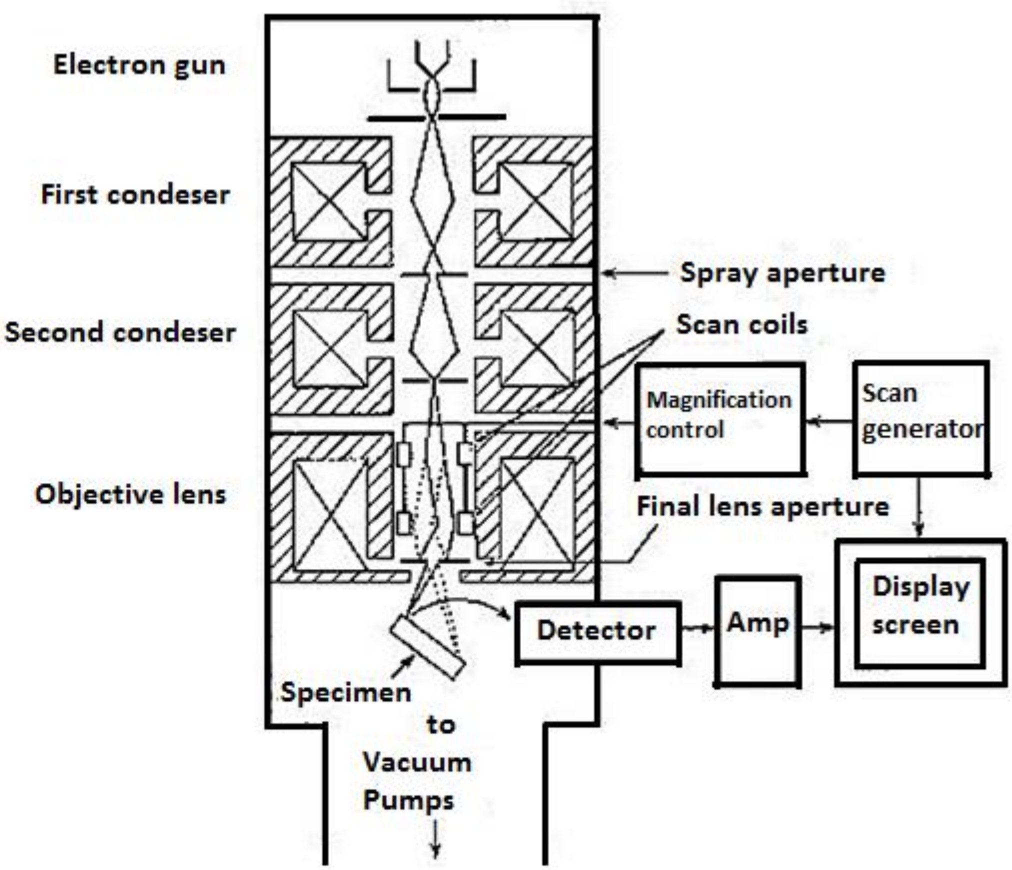

Figure 4.5: Schematic diagram for instrumentation of FE-SEM [17].

The purpose of electromagnetic lenses in FE-SEM is for electron probe formation and while the two condenser lenses minimizes the crossover diameter of the electron beam; then, the objective lens focuses the electron beam as a probe with a diameter on the nanometer scale. The third lens which is called objective lens and the function of it is to demagnifies the cross-section of the electron beam. The probe scanning is operated by a beam deflection system merged within the objective lens in FE-SEM; the deflection system moves the probe over the sample surface in a raster pattern. In addition, deflection system of the electron probe is controlled by two pairs of scan coils (electromagnetic coils). The variety of signals emitted from the sample are collected by a detector, amplified and used to form an image, according to one-to-one correlation between scanning points on the sample and picture points on a screen of a cathode ray tube (CRT). The magnification of FE-SEM is dependent to the ratio of the linear size of the display screen to the linear size of the sample area being scanned [18]. For example if the screen is 500 mm and scanned area on the specimen is 5 mm across, therefore magnification is ×100, and for a higher magnification of ×1000 the scan area of 0.5 mm across the specimen is required [1,17].

4.6 Energy dispersive x-rays spectroscopy

Energy dispersive x-rays spectroscopy (EDS) equipped to FE-SEM, it enables the user to extract important information about chemical composition of the material. The principle of EDS involves the removal of electrons from the core shells of the atom when the sample irradiated with a beam of high energy electrons. Electrons from higher energy states then fill these vacancies and that will result in the emission of energy in a form of an x-ray photon i.e characteristic x-rays as shown in figure 4.6.

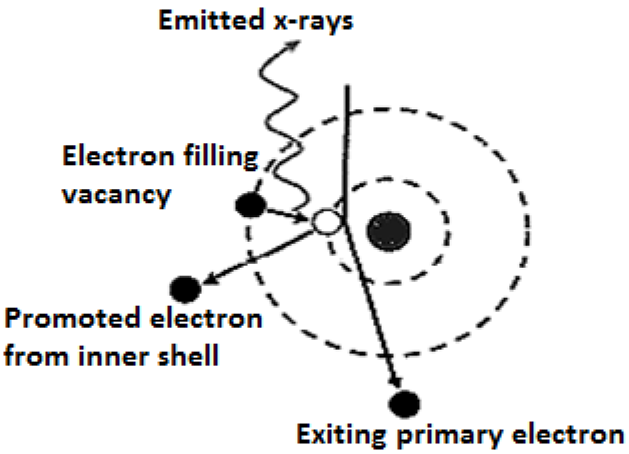

Figure 4.6: Illustration of emitted characteristic x-rays in an atom [19].

As a result of core shell vacancy then Auger electrons is also created, this process involves an electron from outer shells fill the vacancy and transfer the excess energy to another electron in an outer shell, which is then ejected as Auger electron. The Auger electrons are usually detected for the lighter elements, which is low atomic number elements. The EDS spectrum presents peaks that can be correlated to the energy levels for which the most x-rays received, and the peak that have high counts in a spectrum it indicates that particular element in the specimen is concentrated. In addition, the peaks also signify the presence of elements in the specimen. The limitation of EDS is incapable of detecting the elements such as hydrogen (H), helium (He) and lithium (Li) because at least two electrons are required for the process of generation of x-rays to occur [19-21].

4.7 Photoluminescence spectroscopy

Atoms emit light by spontaneous emission when electrons in excited states fall back to a lower level by radiative transitions. In phosphors the radiative emission process is called luminescence. There are many different types of luminescence existing such as cathodoluminescence, thermoluminescence, photoluminescence and electroluminescence. However, in this work photoluminescence was the main aspect the term which is simply means the re-emission of light from a phosphor material after absorbing a photon of higher energy. The technique used to characterize such properties is called photoluminescence (PL) spectroscopy [22,23].

The PL system with 325 nm He-Cd laser was used in this study. The He-Cd laser is assembled in the form of a tube, terminated by two Brewster's angle windows, with two laser mirrors mounted separated from the tube. The tube is filled with He, has a reservoir containing the Cd and a heater to vaporize the metal. In addition, the reservoir temperature should be high enough typically 250 ^{o}C to generate the desired vapour of Cd atoms in the tube. The He-Cd laser has a fixed UV excitation wavelength of 325 nm. In this work a 325 nm He-Cd laser was used to study the photoluminescence properties of the nano-phosphor in visible region. This was done by directing the laser beam on to a sample by aligning lenses and mirrors, followed by the chopper that was used to ensure that the light beam is sent in packets. The monochromator consists of diffraction gratings which serve as the engine of the entire optical measurement system and it is used to differentiate between emissions at different photon wavelengths. Eventually, the light from the sample is sent to the detector: photomultiplier tube (PMT) in visible region [9, 24]. Figure 4.7 depicts a schematic diagram of PL system with He-Cd laser of a fixed excitation wavelength 325 nm.

In this study the up-conversion photoluminescence was also investigated by a fiber-coupled 980 nm IR laser as the excitation source for the up-conversion excitation. This is the powerful laser with the output power that varies from 7 up to 2977 mW. The laser beam is directed straight to the sample and up-conversion emissions is recorded using monochromator equipped with PMT detector. The excitation source and detector needs to be aligned using 90° measurement geometry to prevent the entrance of excitation laser into the detector [25].

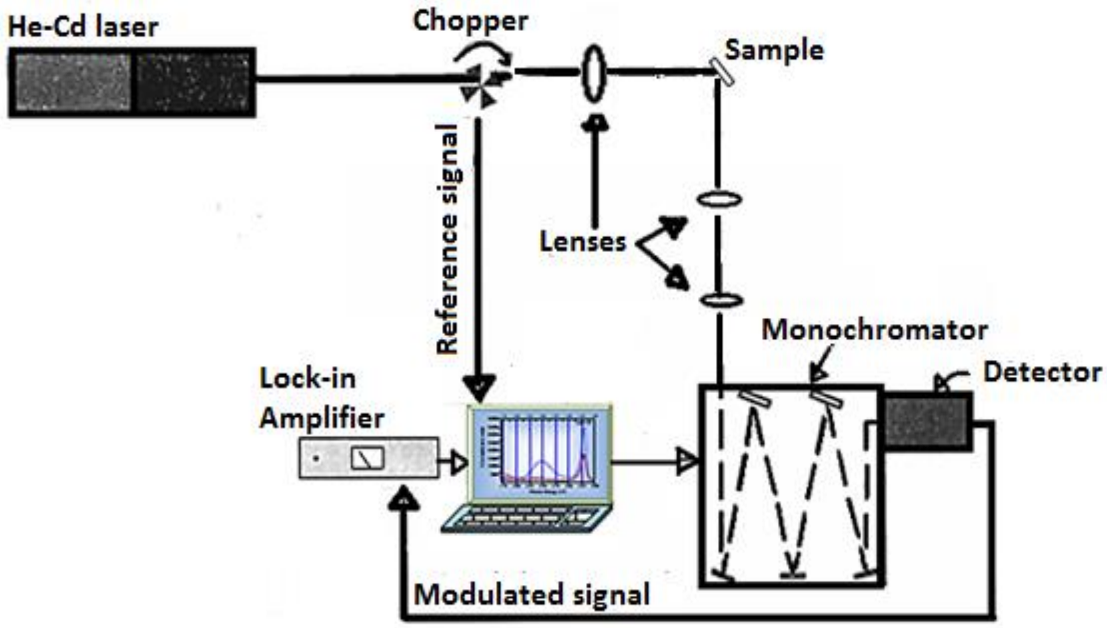

Figure 4.7: Schematic diagram of PL system with He-Cd laser of a fixed wavelength 325 nm.

4.8 References

[1]. P.P. Mokoena, O.M. Ntwaeaborwa, H.C. Swart, Narrowband Ultraviolet B emission from gadolinium and praseodymium co-activated calcium phosphate phosphors for phototherapy lamps, MSc Thesis, (2014), University of the Free State, Bloemfontein, South Africa.

[2]. W.A.I. Tabaza, R.E. Kroon, H.C Swart, Synthesis and characterization of $MgAl_2O_4$ and $(Mg_xZn_{1-x})Al_2O_4$ mixed spinel phosphors, PhD Thesis, (2014) , University of the Free State, Bloemfontein, South Africa.

[3]. B.D. Cullity, Elements of X-ray diffraction, 2nd edition, Addison-Wesley publishing company, (1956) page 20.

[4]. F.R. Cummings, D. Knoosen, TiO_2 nanotube based dye-sensitised solar cells, PhD Thesis, (2012), University of the Western Cape, Cape Town, South Africa.

[5]. https://commons.wikimedia.org/wiki/File:Bragg%27s_Law.PNG [Last accessed 03 September 2015].

[6]. http://pd.chem.ucl.ac.uk/pdnn/peaks/size.htm. [Last accessed 01 June 2015].

[7]. P.K. Giri, D.K. Goswami, A. Perumal, Advanced nano-materials and nanotechnology,(2013) Springer-Verlag, Berlin Heidelberg, page 143.

[8]. P.A. Moleme, O.M. Ntwaeaborwa, H.C. Swart, Cathodoluminescence degradations and surface characterization of $SrGa_2S_4$:Ce^{3+} powder and thin films, MSc Thesis, (2011), University of the Free State, Bloemfontein, South Africa.

[9]. M.A. Tshabalala, B.F. Dejene, H.C. Swart, The synthesis and characterization of the ZnO nanoparticles, MSc Thesis, (2011), University of the Free State, Bloemfontein, South Africa.

[10]. https://www.youtube.com/watch?v=wxrAELeXlek, [Last accessed 16 July 2015].

[11]. C. Guillen, J. Herrero, Solar energy materials, 23 (1991) page 31.

[12]. D. Bhattacharya, S. Chaudhuri, A.K. Pal, Vacuum, 43 (1992) pages 313-316.

[13]. http://mmrc.caltech.edu/FTIR/FTIRintro.pdf [Last accessed 19 July 2015].

[14]. http://chemwiki.ucdavis.edu/Physical_Chemistry/Spectroscopy/Vibrational_Spectroscopy/Infrared_Spectroscopy/How_an_FTIR_Spectrometer_Operates [Last accessed 21 July 2015].

[15]. JEOL Serving Advanced Technology Q & A book, JEOL DATUM Ltd, No. 1101C993C printed in Japan, Kp.

[16]. J.H. O'Connell, J.H. Neethling, Characterization of hydrogen and helium implanted silicon carbide, MSc Thesis, (2009), Nelson Mandela Metropolitan University, Port Elizabeth, South Africa.

[17]. Y. Leng, Materials characterization Introduction to microscopic and spectroscopic methods, (2008), John Willey & Sons, page 267 - 276.

[18]. http://www.understanding-cement.com/sem-introduction.html [Last accessed 01 April 2016]

[19]. M. Wisconsin, Energy-dispersive X-ray microanalysis, (1999) NORAN Instruments, West Beltline Highway, pages 5 - 12.

[20]. P.S. Mbule, O.M. Ntwaeaborwa, H.C. Swart, Sol-gel synthesis of and luminescent properties of Pr^{3+} in different host matrices, MSc Thesis, (2009), University of the Free State, Bloemfontein, South Africa.

[21]. http://www.understanding-cement.com/sem-introduction.html, [Last accessed 29 July 2015].

[22]. L.L. Noto, H.C. Swart, J.J. Terblans, Red emissions of Praesodymium ions (Pr^{3+}), MSc Thesis, (2011), University of the Free State, Bloemfontein, South Africa.

[23]. M. Fox, Optical properties of solids, (2001), Oxford University press Inc, New York, page 92 - 93.

[24]. M.A. Lephoto, O.M. Ntwaeaborwa, B.M. Mothudi, H.C. Swart, Luminescent properties of combustion synthesized $BaAl_2O_4:Eu^{2+}$ and $(Ba_{1-x}Sr_x)Al_2O_4$: Eu^{2+} phosphor codoped with different rare earth ions, MSc Thesis, (2011), University of the Free State, Bloemfontein, South Africa.

[25]. P. Ramasamy, P. Manivasakan, J. Kim, Royal Society of Chemistry, 4, (2014) 34873 - 34895.

5. Cooperative luminescence from low temperature synthesis of α-Al_2O_3: Yb^{3+} phosphor by using solution combustion method

5.1 Introduction

Recently, ytterbium (Yb^{3+}) is considered a most interesting rare-earth (RE) dopant ion to study in the field of luminescence because it consists of two manifolds $^2F_{7/2}$ ground state and $^2F_{5/2}$ excited state separated by approximately 10 000 cm^{-1}. The large energy gap and lack of intermediate levels between the two manifolds minimize a probability of non-radiative recombination. Thus, Yb^{3+} ion displayed efficient luminescence in different hosts [1,2]. Cooperative luminescence is a typical up-conversion process by which two interacting ions in the excited state decays to the ground state emitting one photon with the sum energies of the energy of the excited state of a single Yb^{3+} ion [3]. The process of cooperative luminescence can be easily achieved in Yb^{3+} based systems because 4f electrons in Yb^{3+} are less shielded than in other RE ions. In this process, the simultaneous de-excitation of two Yb^{3+} ions occurs from excited to ground states resulting in blue-green visible emission (~500 nm). In addition, this visible emissions is induced by the near infrared (NIR) excitation which causes anti-stokes shift [4,5]. The cooperative luminescence depends on factors such as a laser excitation power, inter-ionic distances, phonon energy and location of the edge of the fundamental absorption of the host [6]. The cooperative up-conversion emission of Yb^{3+} ions near 500 nm exhibits similar emissions of Tm^{3+} ions for three-dimensional display technology. The use of singly doped Yb^{3+} ions in a host can minimizes the cost of a multicolor display by requiring only one laser pumping beam in the NIR region [7].

Alumina (Al_2O_3) ceramic oxide is one of the most useful host lattice for rare-earth ions to prepare light emitting materials. It has got tremendous properties such as high melting point, hydrophobicity, good chemical stability, high optical transparency, good thermal and mechanical stability, and fine optical and dielectric characteristic [8,9]. There are different phases of alumina which are α, β, γ, η, θ, κ and χ. The phase α-Al_2O_3 is considered as the most thermodynamically stable at 1200 °C and others are metastable phase obtained during the calcination of aluminium hydroxides [10]. The phase α-Al_2O_3 is called corundum. In this structure Al atom is octahedrally coordinated with oxygen atoms as illustrated in figure 5.1 and was drawn by Diamond crystal software [11]. The structure can be seen as hexagonal close-packed (HCP) oxygen atoms with small Al atoms occupying two-thirds of the octahedrally coordinated holes between the oxygen atoms. The dimensions of unit cell are: $a = b = 4.7588$ Å and $c = 12.992$ Å [12].

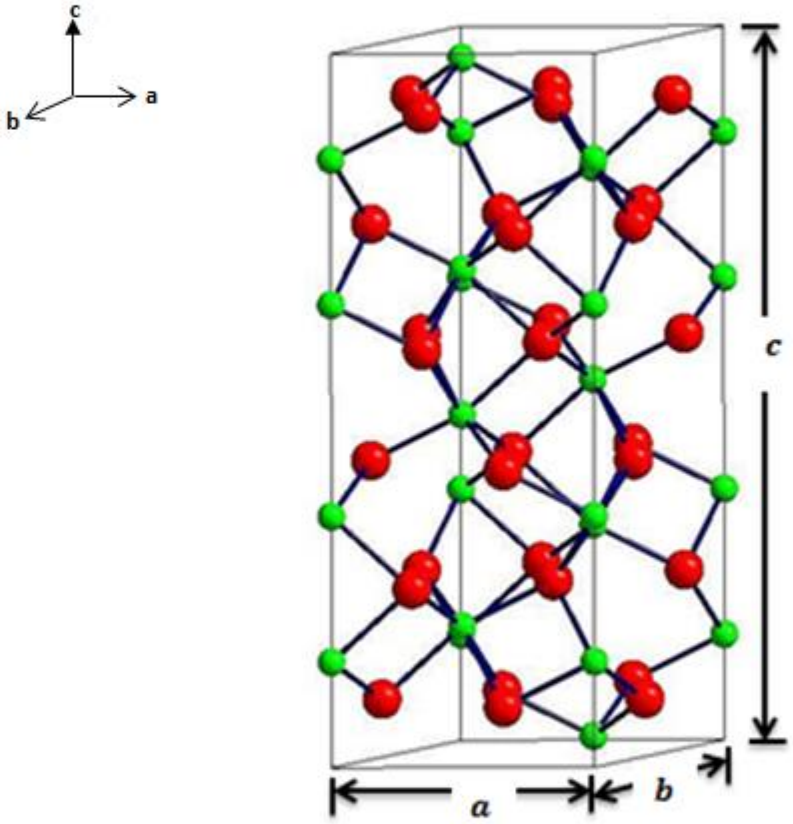

Figure 5.1: The corundum structure (Al atoms, green spheres and O atoms, red spheres) [13].

In this present study, the phase α-Al_2O_3:Yb^{3+} phosphor powder was synthesized by solution combustion method. The stoichiometric amount of aluminium nitrate, ytterbium nitrate and urea in a solution were transferred to a muffle furnace preheated to 550 ^oC resulting in the formation of α-Al_2O_3:Yb^{3+}. The cooperative and near-infrared (NIR) emissions from Yb^{3+} singly doped were observed.

5.2 Experimental procedure

5.2.1 Powder preparation

In a typical preparation, the stoichiometric amount of aluminium nitrate, ytterbium nitrate and urea were disolved in de-ionised water. A homogeneous transparent solution was obtained after stirring vigorously for 60 min. The transparent solution was transferred to a muffle furnace maintained at 550±10 ^{o}C. After all the liquid had evaporated, the mixture decomposed and released large amounts of gases. Due to the exothermic nature of the combustion process, the reaction continued for a while and mixture swelled to a large volume. Large exothermicity resulted in a high temperature flame that further decomposed the mixture into gaseous phase and alumina. The combustion process was completed in less than 5 min [28]. The resulting powder was gently ground by pestle motar. α-Al_2O_3:Yb^{3+} phosphor powders with Yb^{3+} concentrations of 0.4, 0.8 and 1.2 mol% were prepared. The procedure for the synthesis of our powder phosphors is shown schematically in figure 5.2.

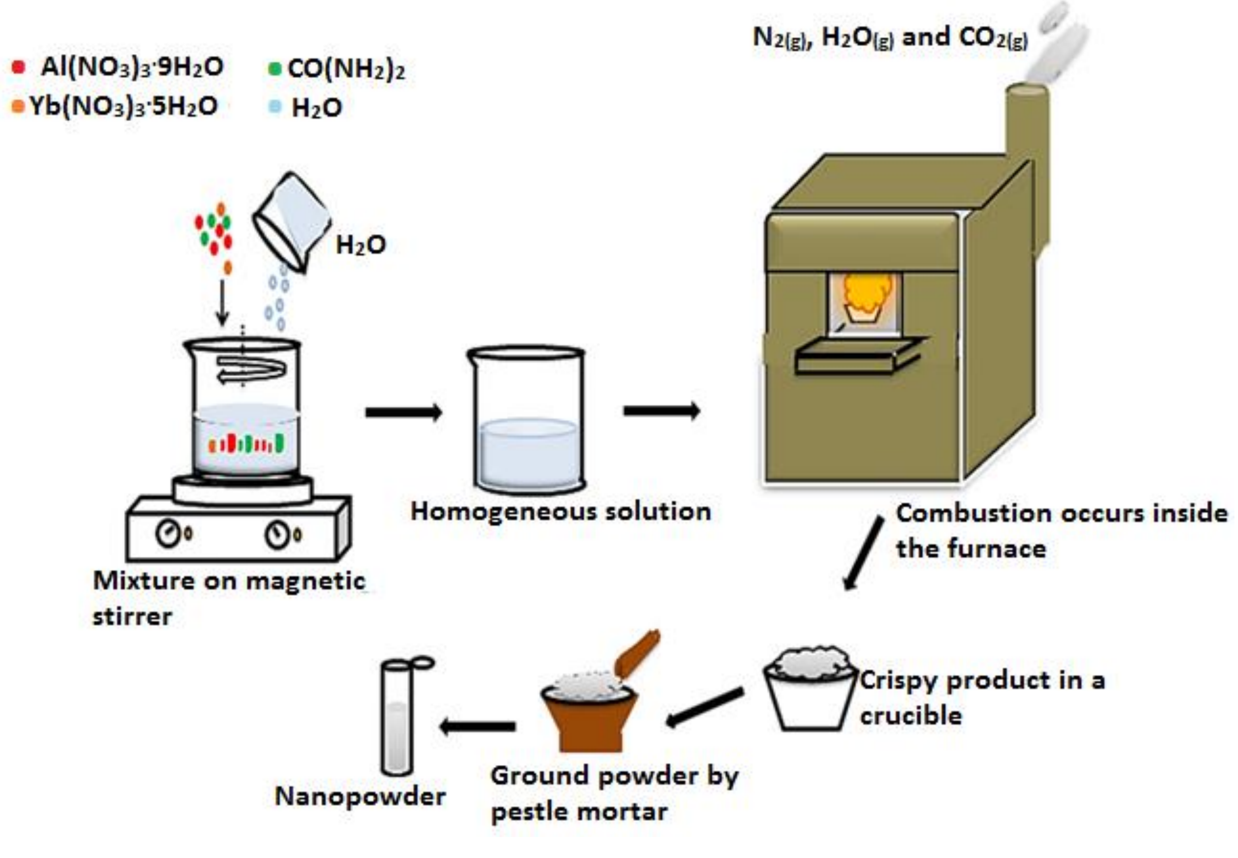

Figure 5.2: A schematic diagram of the synthesis procedure of α-Al_2O_3:Yb^{3+} nanopowder.

5.2.2 Characterization

The crystal structure of the phosphor powder was analyzed using a Bruker D8 Advanced X-ray diffractometer (XRD) with CuK_α radiation wavelength of 0.154 nm. The particle morphology and chemical composition of the materials were carried out using JEOL JSM-7800 field emission scanning electron microscope (FE-SEM) coupled with energy dispersive x-ray spectroscopy (EDS). The diffuse reflectance uv-vis measurements were taken using Lambda 950 spectrophotometer. The study of vibrational bonds of the material was carried out by Fourier transform infrared (FTIR) spectroscopy. Near infrared (NIR) emission measurements were carried out by using PL system consists of a 325 nm He-Cd laser as excitation, monochromator equipped with 2 mm InGaAs photodiode detector and a lock-in amplifier. Up-conversion measurements were performed by using fiber-coupled 980 nm NIR laser as the excitation source, monochromator equipped with photomultiplier tube (PMT) detector and a lock-in amplifier.

5.3 Results and Discussion

5.3.1 XRD analysis

Figure 5.3 presents XRD patterns of α-Al_2O_3:Yb^{3+} phosphor powders. The XRD patterns were consistent with hexagonal phase of α-Al_2O_3 with space group R3c referenced in the JCPDS file number 46-1212. For all doped samples a small impurity peak that was marked with asterisks (*) that can be assigned to the (110) diffraction peak of aluminium ytterbium oxide ($YbAlO_3$) was detected at $2\theta = 24.065\ ^{o}$ and was referenced with JCPDS file number 20-1392 [14]. The diffraction peaks of the α-Al_2O_3:Yb^{3+} were broadened as the concentration of Yb^{3+} increases in a host. The broadening can be due to instrumental settings, smaller crystallite sizes and micro-strains in the lattice. The incorporation of Yb^{3+} in a host lattice caused the XRD peaks to shift to the high Bragg angles as shown in figure 5.4. This indicates lattice contraction due to the lattice strains caused by Yb^{3+} ions because ionic radius of Yb^{3+} (0.0858 nm) is bigger than Al^{3+} (0.050 nm) ions [15,16]. To estimate peak broadening of these phosphor powders, full-width at half maximum (FWHM) for (113) XRD peak as a function of Yb^{3+} concentration was shown in figure 5.5. The increase of peak broadening due to the concentration of Yb^{3+} doping with a small fluctuation at 0.8 mol% was observed. Tshabalala et al. [17] suggested that the broadening may be due to small crystallite sizes and lattice strains. The Yb^{3+} ions in the doped α-Al_2O_3: Yb^{3+} substitutes Al^{3+} ions and become octahedrally coordinated to the six nearest O^{2-} ions. Feng et al.[15] suggested that because of the difference in electronegativities, masses and ionic radii between the Yb^{3+} and Al^{3+} ions then the bond lengths of the host (Al^{3+}-O^{2-}) and doped crystal (Yb^{3+}-O^{2-}) will also differ by 0.01089 nm and 0.01986 nm, respectively [18].

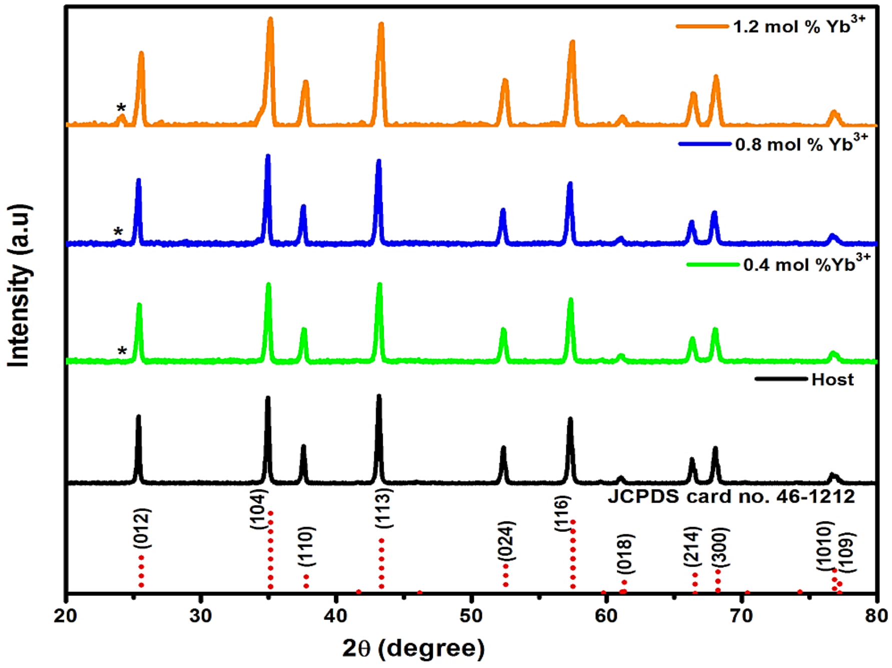

Figure 5.3: XRD patterns of α-Al_2O_3:Yb^{3+} phosphor powders.

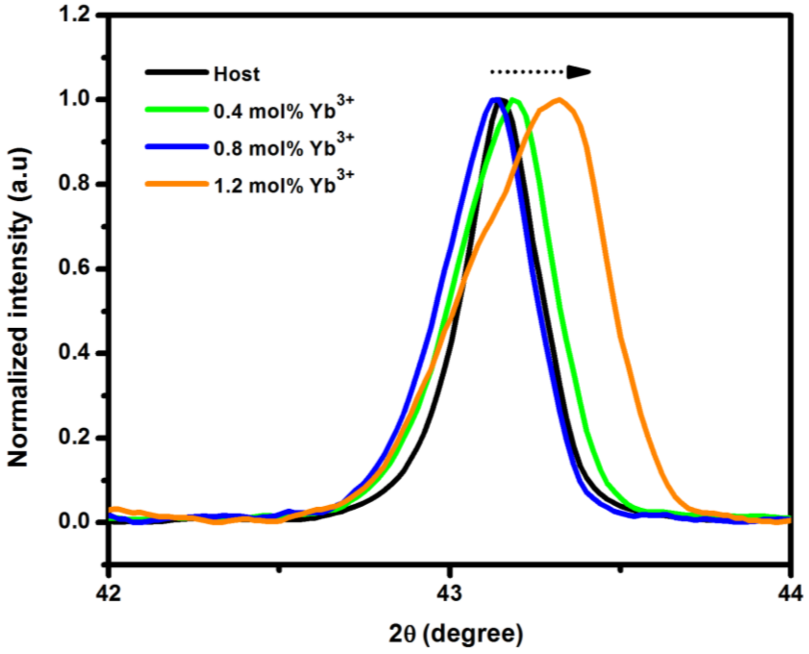

Figure 5.4: Analysis of XRD peak for (113) peak at different Yb^{3+} concentrations.

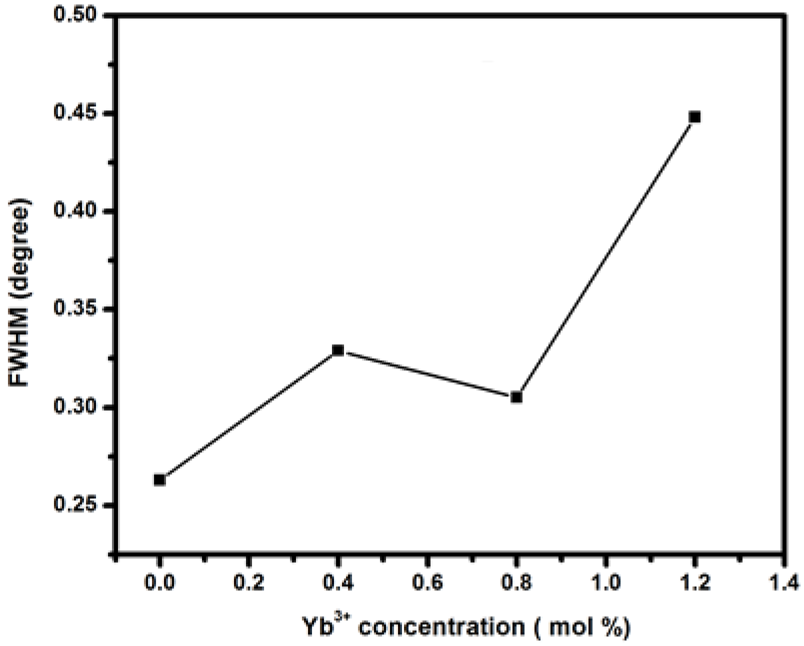

Figure 5.5: Full-width at half maximum (FWHM) for the (113) peak versus Yb^{3+} concentration.

The XRD patterns for post-preparation annealing at 1000, 1200 and 1400 ^{o}C are shown in figure 5.6. The post-preparation annealing did not perturb the α-phase of alumina. To determine the crystallinity of these phosphor powders, full-width at half maximum (FWHM) for (113) XRD peak as a function of temperature was shown in figure 5.7. The FWHM decreases from 0.323 ^{o} to 0.209 ^{o} as the temperature was raised from 1000 ^{o}C to 1400 ^{o}C. This indicates that the improvement in crystallinty was observed from 1000 ^{o}C to 1400 ^{o}C [19].

The average crystallite size D was estimated from full-width at half maximum β of the diffraction peaks at angle θ by using Scherrer equation $D = 0.9\lambda/\beta cos\theta$ where λ is the x-ray wavelength and found to be ~ 29 nm for a host α-Al_2O_3. The D for doped phosphor powders was 24, 26 and 19 nm for 0.4, 0.8 and 1.2 mol% Yb^{3+}, respectively. Figure 5.8 shows the crystallite size as function of Yb^{3+} concentration. This reduction in crystallite sizes indicates that the addition of Yb^{3+} in a host lattice affects the crystalline growth kinetics. Before distributing itself into the α-Al_2O_3 crystal structure, the Yb^{3+} is initially occupied between grain boundary regions of a host and therefore disturbs the normal growth of the α-Al_2O_3 crystallites, (FE-SEM confirms later on) [20].

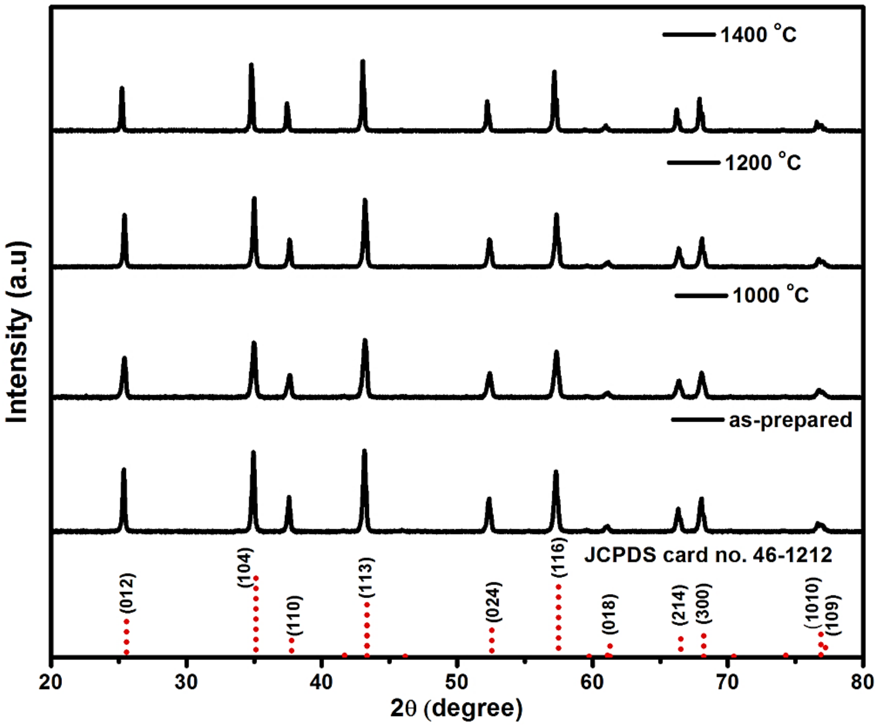

Figure 5.6: Post-preparation annealing of α-Al_2O_3:Yb^{3+} phosphor powders in air for 2 hours.

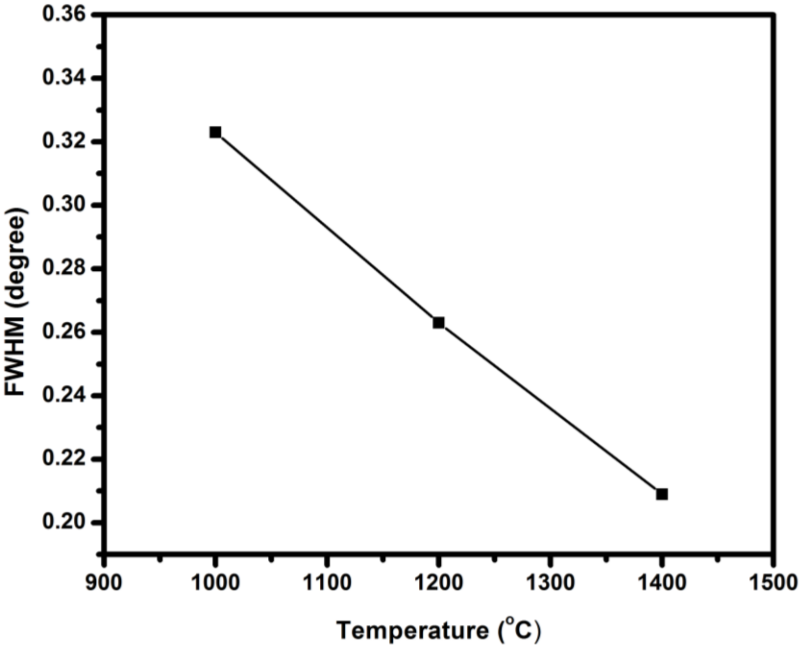

Figure 5.7: Experimental data of FWHM for the (113) peak versus temperature.

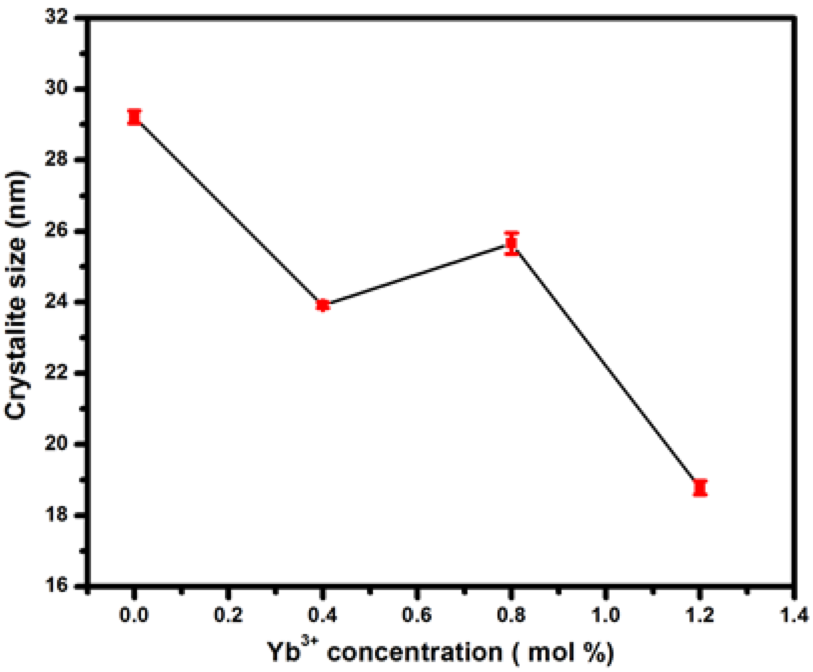

Figure 5.8: Crystallite size as the function of Yb^{3+} concentration

5.3.2 UV-vis analysis

The UV-vis diffuse reflection spectroscopy in this work was used to study absorption properties of the host and the effects of Yb^{3+}. Figure 5.9 depicts the reflectance spectra of all phosphor powders. The inset shows two absorption bands centered at 265 nm and 371 nm originating from the host. The absorption band centered at 265 nm was assigned with the band-to-band transition of octahedral AlO_6 anion in a host α-Al_2O_3 [21], while the absorption band centered at 371 nm was due to F^+ center band of oxygen vacancies with one electron trapped [22]. There was a redshift in UV absorption due to Yb^{3+} doping in a host and no absorption peaks were observed in this region from the dopants (Yb^{3+}) because of large absorption cross-section in 980 nm.

Figure 5.10 presents the determination of direct optical bandgap of α-Al_2O_3: Yb^{3+} phosphor powder by Tauc plot of $(\alpha h\nu)^n$ against $h\nu$, with $n = 2$ which were correct for a direct optical bandgap material such as α-Al_2O_3. The inset demonstrates that the bandgap of a host was estimated to be 5.51 eV, while theoretical bandgap of the bulk Al_2O_3 has a value of 8 eV [23,24]. The reduction of bandgap in the present study can be explained in terms of the appearance of some defects levels located within the bandgap such as F^+-and F-center bands [25]. The results also indicates that incorporation of Yb^{3+} into a host reduces a bandgap of material between 5.51 – 5.16 eV due to Yb^{3+} doping, the impurity band becomes broader and eventually merges with the bottom of the conduction band causing the reduction in the bandgap. Therefore, this phenomenon it is called the “bandgap engineering” [26].

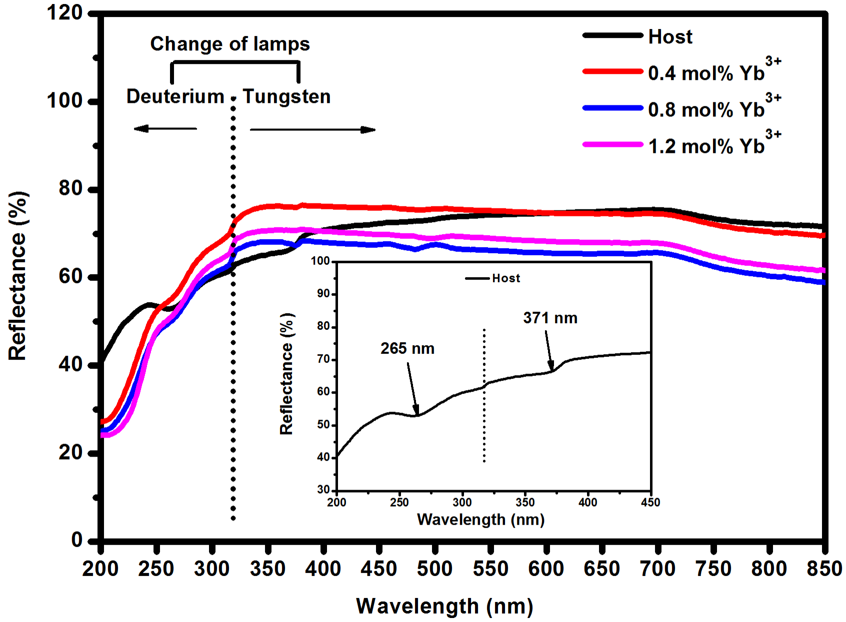

Figure 5.9: The diffuse reflectance spectra of α-Al_2O_3: Yb^{3+} phosphor powder

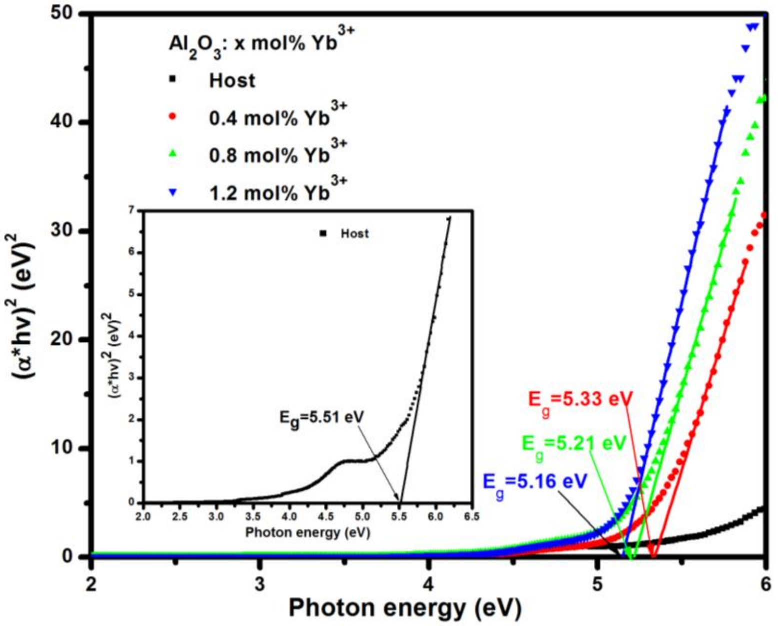

Figure 5.10: Determination of direct optical bandgap of α-Al_2O_3: Yb^{3+} phosphor powder by Tauc plot.

5.3.3 FTIR analysis

Figure 5.11 presents FTIR spectra of α-Al_2O_3: Yb^{3+} phosphor powders. Most of the characteristic peaks of α-Al_2O_3:Yb^{3+} were observed in the finger-printing region (400 – 1400 cm^{-1}). The absorption peaks at 435 and 598 cm^{-1} were both assigned to Al-O-Al bending mode and these two absorption bands indicates "α" phase of alumina [26, 27] and there was an absorption band at 805 cm^{-1} for doped samples which was assigned to Yb-O vibrations [10]. Other weak absorption bands in the range of 1091 – 1391 cm^{-1} were assigned to Al-O vibrations. The peaks at 2919 and 3433 cm^{-1} show the presence of hydroxyl (OH) vibrations, indicating presence of Al-OH bonds in these samples or probably moisture from KBr pellet. The other peaks might arise from incidental impurities such as hydrocarbons and atmospheric CO_2 [24].

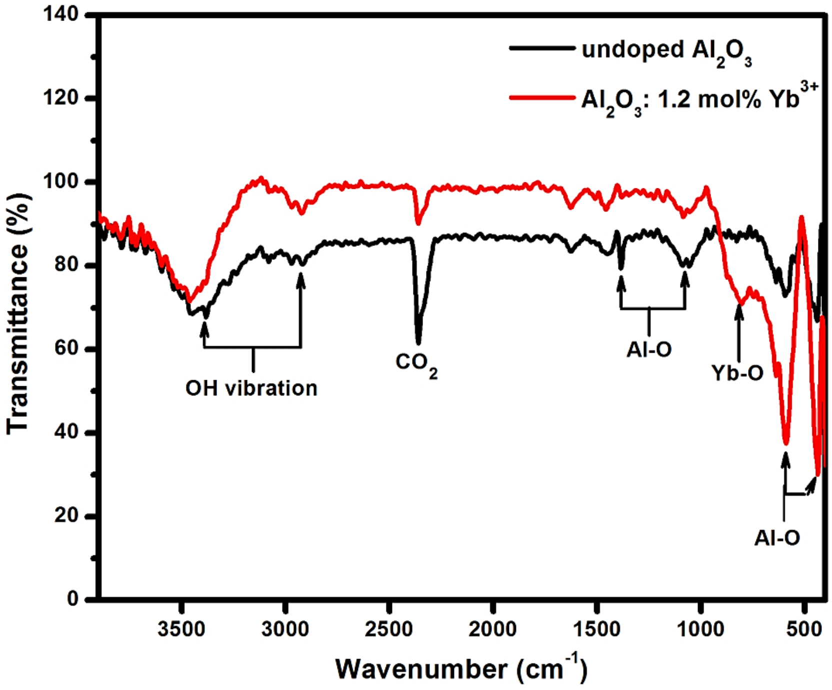

Figure 5.11: FTIR spectra of α-Al_2O_3: Yb^{3+} phosphor powder.

5.3.4 FE-SEM and EDS analysis

The FE-SEM micrographs of α-Al_2O_3 host (a) and (b), and α-Al_2O_3:1.2 mol% Yb^{3+} (c) and (d) phosphor powders are shown in figure 5.12. The low magnification micrograph of the host (Fig 5.12 (a)) shows that the powders composed particles with irregular shapes and well defined grain boundaries, while the high magnification image (Fig. 5.12 (b)) indicate that these particles were porous. These pores are due to the evolved of gases during combustion reaction [28]. Figure 5.12 (c) and (d) demonstrate that the dopants (Yb^{3+}) mostly occupied the grain boundary regions.

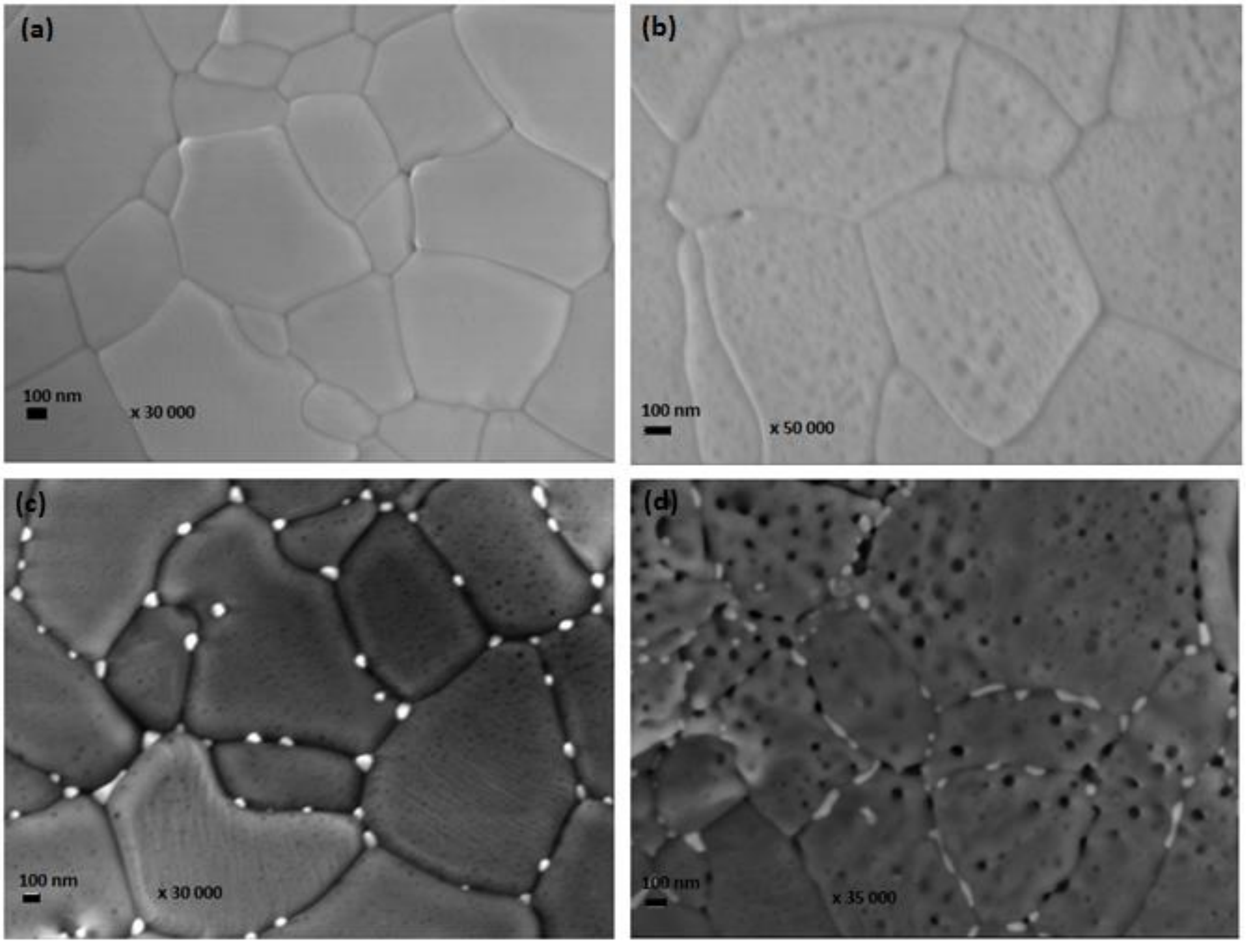

Figure 5.12: FE-SEM micrographs of (a), (b) host and (c), (d) α-Al_2O_3: 1.2 mol% Yb^{3+} phosphor powders**.**

EDS spectra of α-Al_2O_3:Yb^{3+} phosphor powder confirmed that all elements are present in the material as shown in figure 5.13. The inset in the top middle demonstrate the SEM micrograph and the positions where EDS analysis was done are marked S3 and S4 while the one on the top right corner depicts the bar graph comparing the weight % of the elements at the chosen positions. The elements such as Al, Br and Yb show an overlaps of K_α, L_α and M_α at corresponding energies of 1.49, 1.48 and 1.52 keV, respectively. Thus, in this present study the element Br was overlapping with Yb. Figure 5.13 compares the EDS spectra performed at S3 and S4, the concentration of Al is 52 % and 41 % at S3 and S4, respectively. The concentration of O is 48 % and 46 % at S3 and S4, respectively. The concentration of Yb is 12 % at S4 but no concentration of it was detected at S3. Thus, the reduction of Al concentration in S4 indicates that the presence of Yb^{3+} in a host replaces Al^{3+} ions as XRD confirmed [29].

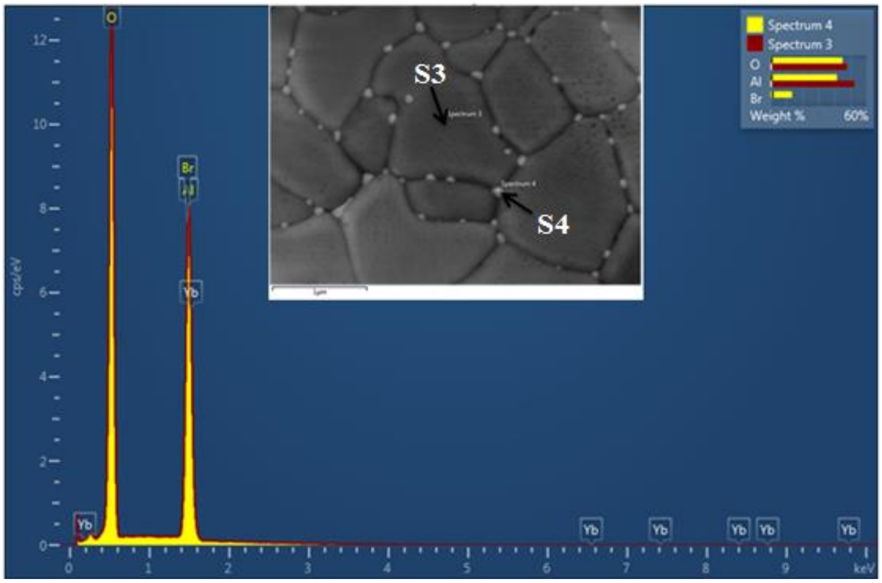

Figure 5.13: EDS spectra of α-Al_2O_3: Yb^{3+} phosphor powder.

5.3.5 PL analysis

Figure 5.14 shows PL spectra of α-Al_2O_3:Yb^{3+} phosphor powders under excitation of 325 nm He-Cd laser. All the samples show a broad emission band extending from 380 to 600 nm, with three resolved peaks with maxima at 412, 435 and 454 nm. Figure 5.15 shows a Gaussian fit for the broad band emission of a host α-Al_2O_3. The band can be deconvoluted into five Gaussian functions with maxima at 412 (Peak 1), 425 (Peak 2), 435 (Peak 3), 454 (Peak 4) and 499 nm (Peak 5). The emission at 412 and 425 nm were assigned to F-centers of oxygen vacancies defects with two electrons trapped, while 435, 454 and 499 nm were assigned to the F^+ centers with one electron trapped [30,31]. The emission marked with asterisks (*) may be due to extrinsic incidental impurities from insufficient purification of precursors. There is a change in intensity for all samples which may be because of change in pore size of the material or perhaps concentration quenching by impurities or structural defects. Gangwar et al.[27] confirmed that increase in pore size gives increasing surface area to the source which promote more absorption of photons and high intensity radiation [27], [32]. Figure 5.16 presents the chromaticity coordinates of α-Al_2O_3:Yb^{3+} phosphor powders under excitation of 325 nm He-Cd laser, determined using the CIE coordinate calculator software. The position of the coordinates in a chromaticity diagram and expected colours of the phosphor powder was shown in figure 5.16. The host exhibit pure blue colour but doped samples were tuned into violet-bluish colour [33].

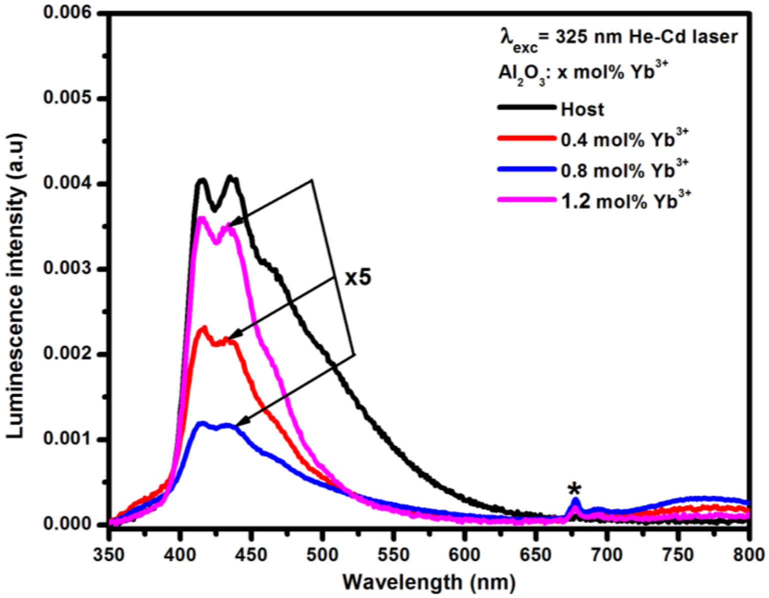

Figure 5.14: PL spectra of α-Al_2O_3:Yb^{3+} phosphor powders under excitation of 325 nm He-Cd laser.

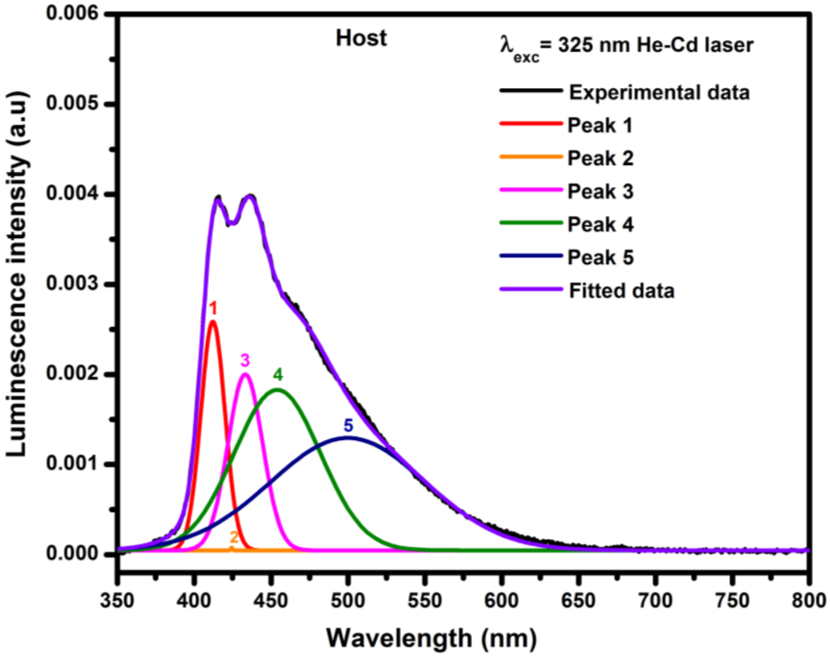

Figure 5.15: Gaussian fit for the PL spectra of α-Al_2O_3:Yb^{3+} phosphor powders under excitation of 325 nm He-Cd lasers

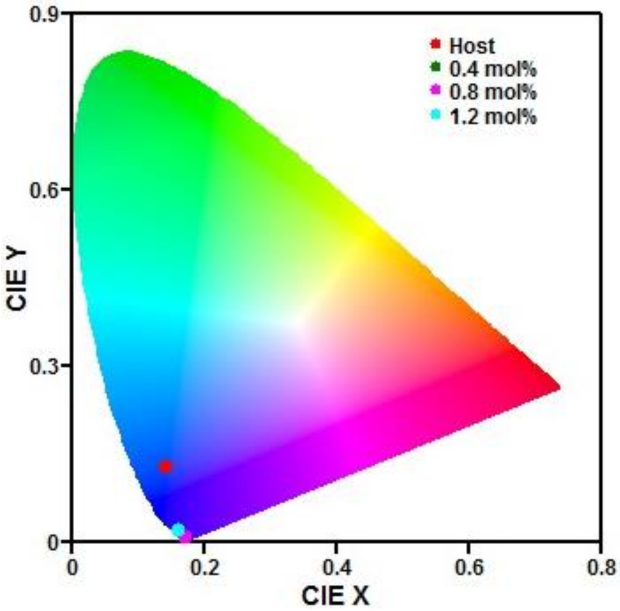

Figure 5.16: CIE colour of α-Al_2O_3:Yb^{3+} phosphor powder under excitation of 325 nm He-Cd laser.

Figure 5.17 shows cooperative emission of α-Al_2O_3:Yb^{3+} phosphor powder under excitation of 980 nm. As it observed, blue-green visible emissions appears at half-wavelength range of the near infrared (NIR) emission of Yb^{3+}. The emission is due to $(^2F_{5/2} + {}^2F_{5/2})$ or $2(^2F_{5/2}) \rightarrow {}^2F_{7/2}$ transition from the virtual state of Yb^{3+}. The inset shows cooperative luminescence process from the virtual state of Yb^{3+}. This process is due to cooperative luminescence of Yb^{3+} pairs, the process is resulting from the simultaneous de-excitation of two interacting Yb^{3+} ions and depends on Coulombian interaction and therefore shows strong dependence on Yb^{3+}-Yb^{3+} distance [1,34,35]. The emission marked with asterisks (*) with maxima at 545 nm was due to erbium (Er^{3+}) contamination probably from the sample holders during up-conversion set up. Figure 5.18 shows the position of the coordinates in a chromaticity diagram and expected colours of the phosphor powders under excitation of 980 nm laser. All doped samples were showing bluish green colour while a host was not glowing, because the excitation wavelength used was not sufficient enough to excite the electrons in a host [33].

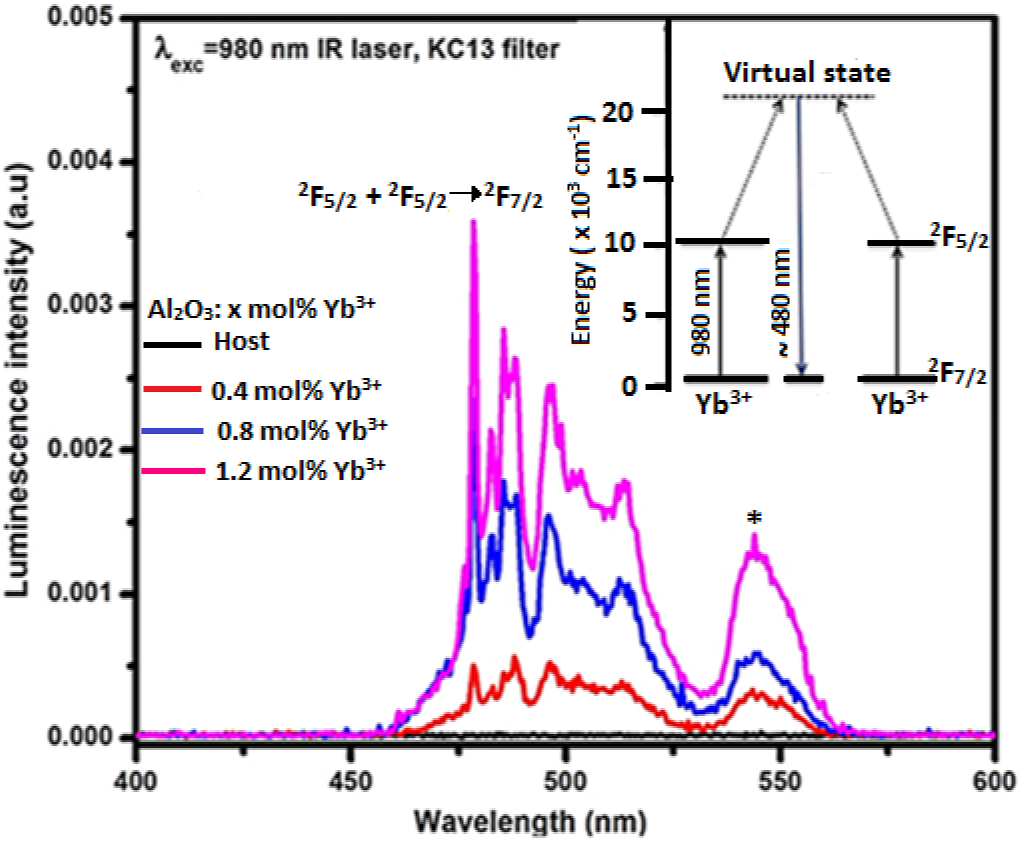

Figure 5.17: Cooperative luminescence of α-Al_2O_3:Yb^{3+} phosphor powder under excitation of 980 nm.

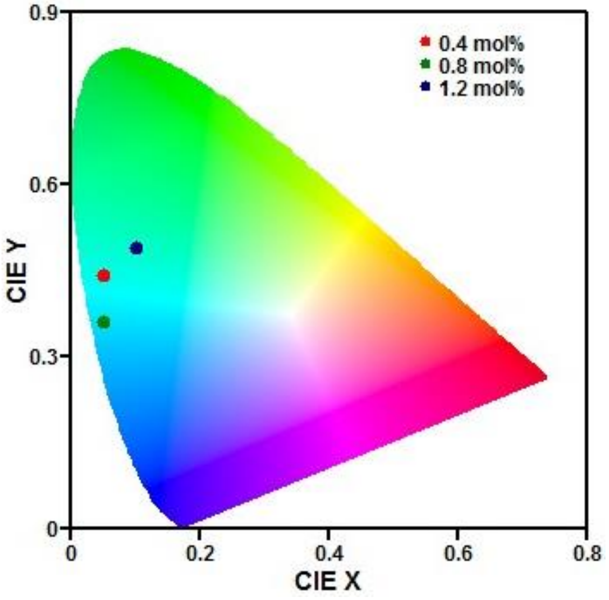

Figure 5.18: CIE colour of α-Al_2O_3:Yb^{3+} phosphor powder under excitation of 980 nm laser.

Figure 5.19 shows NIR emission of α-Al_2O_3:Yb^{3+} phosphor powders under excitation of 325 nm He-Cd laser. Yb^{3+} is usually excited by 980 nm because of two energy levels ground state $^2F_{7/2}$ and excited state $^2F_{5/2}$ with spacing of 10 000 cm^{-1} apart. Figure 5.20 presents Gaussian fit for NIR emission of α-Al_2O_3: 0.8 mol% Yb^{3+} phosphor powders under excitation of 325 nm He-Cd laser. The band can be deconvoluted into four Gaussian functions with maxima at 975 (Peak 1), 1007 (Peak 2), 1030 (Peak 3) and 1080 nm (Peak 4). The inset shows emission from the lowest stack of excited level to the different stacks of ground level in Yb^{3+}. However, in this study excitation of 325 nm He-Cd laser was used and there was an energy transfer from the host α-Al_2O_3 to the dopant Yb^{3+} as illustrated in figure 5.21. The NIR emission of Yb^{3+} are due to $^2F_{5/2}\rightarrow{}^2F_{7/2}$ transition, four emission bands with maxima at 975, 1007, 1030 and 1080 nm were attributed to the transitions from lowest stack of the excited level of $^2F_{5/2}$ manifold to the different stacks of ground level $^2F_{7/2}$. The inset shows a weak emission of a host which was probably caused by intrinsic intraband gap defects such as F- and F^+ centers [36, 37]

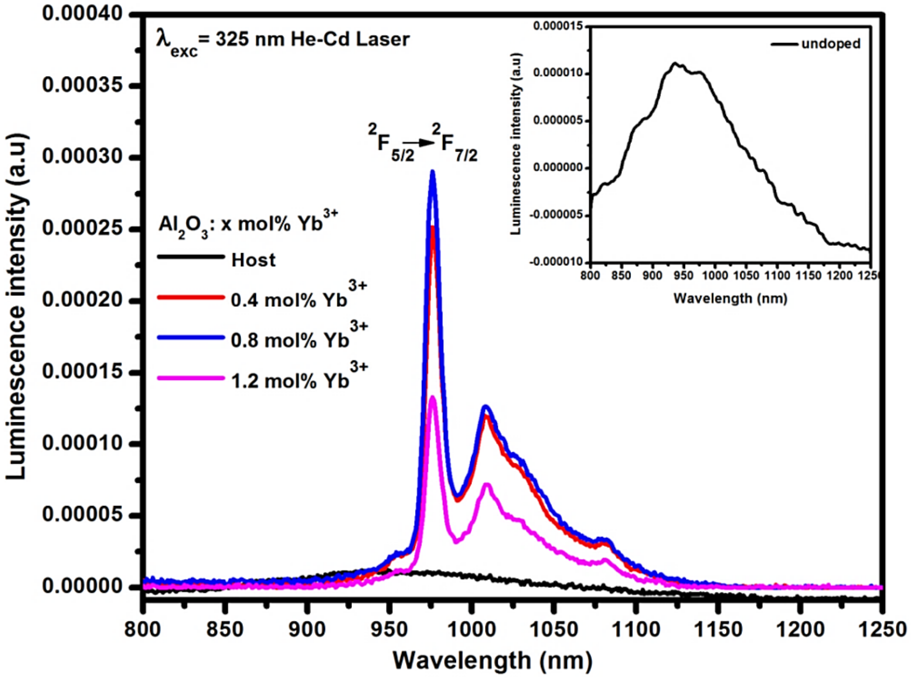

Figure 5.19: NIR emission of α-Al_2O_3:Yb^{3+} phosphor powders under excitation of 325 nm He-Cd laser.

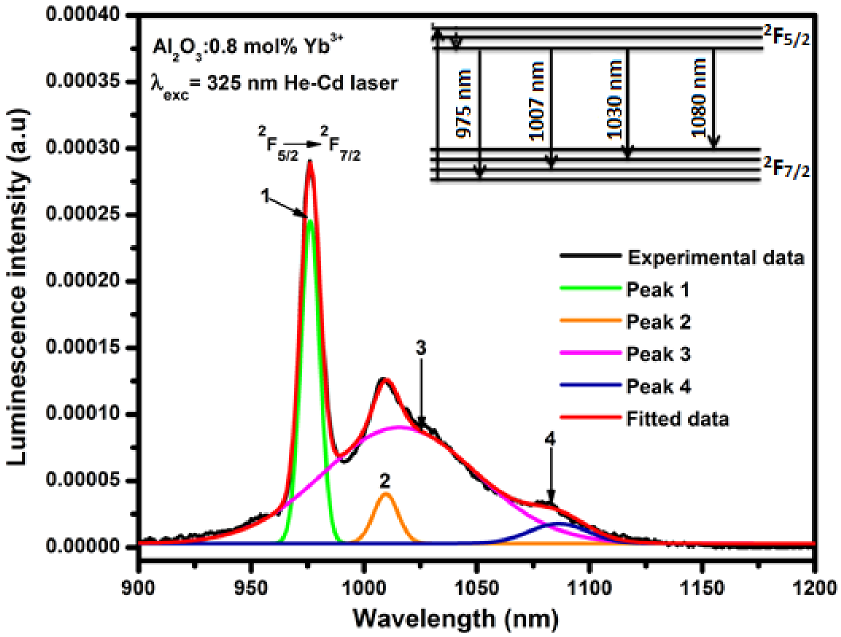

Figure 5.20: Gaussian fit for NIR emission of α-Al$_2$O$_3$: 0.8 mol% Yb^{3+} phosphor powders under excitation of 325 nm He-Cd laser.

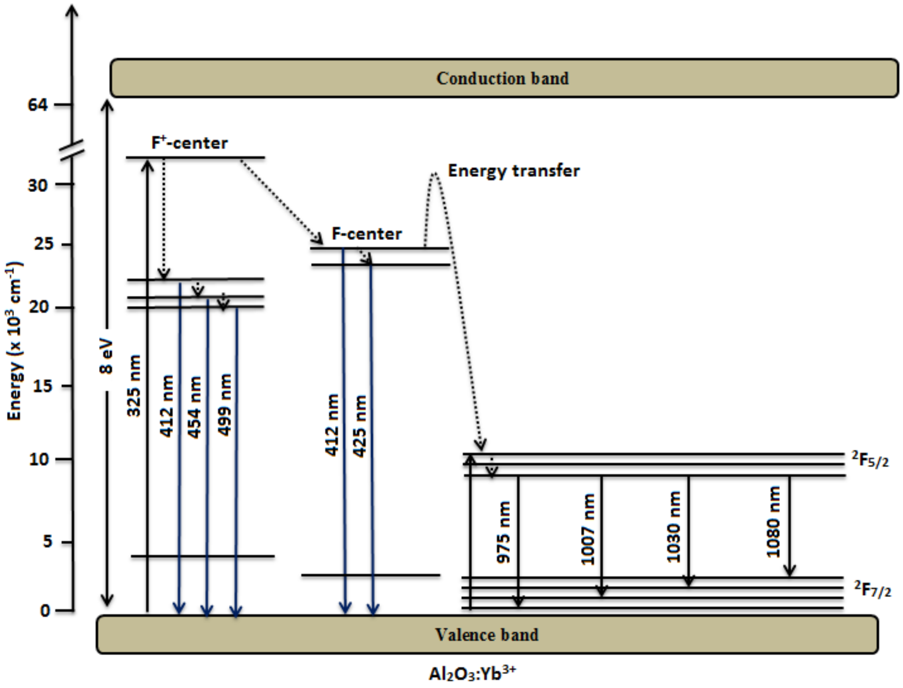

Figure 5.21: Schematic diagram of energy transfer from α-Al$_2$O$_3$ to Yb^{3+} under excitation of 325 nm He-Cd laser. (The full arrows pointed up and down represent photon excitation and emission, respectively. Square dotted lines and curly square dotted represent nonradiatively relaxation and represent energy transfer, respectively).

5.4 Conclusion

The phase α- Al_2O_3:Yb^{3+} phosphor powder has been successfully synthesized by solution combustion method at pre-heated temperature of 550 ^{o}C without any calcination. XRD patterns confirm that the phosphor crystallized in the hexagonal phase of α-Al_2O_3 with space group R3c. The post-preparation annealing did not perturb α-Al_2O_3 phase but has improved the crystallinity at high temperature from 1000 ^{o}C to 1400 ^{o}C. The FTIR measurements confirmed the formation of α-Al_2O_3. FE-SEM confirmed that the dopants Yb^{3+} occupied grain boundaries before substituting Al^{3+} ions. The bluish green emission was observed as the results of cooperative luminescence of Yb^{3+}. The NIR emission of Yb^{3+} was observed under excitation of 325 nm He-Cd laser as the results of energy transfer from the α-Al_2O_3 to the dopant Yb^{3+}. The possible mechanism of the energy transfer was illustrated and discussed.

5.5 References

[1]. M. Puchalska, M. Sobczyk, J. Targowska, A. Watras, E. Zych, Journal of Luminescence, 143 (2013) 503 - 509.

[2]. A. Ellens, H. Andres, M.L.H. ter Heerdt, R.T. Wegh, A. Meijerink, G. Blasse, Journal of Luminescence, 66 & 67 (1996) 240 - 243.

[3]. X. Qia, Y. Ye, Materials Letters, 161 (2015) 248 - 250.

[4]. S.R. Luthi, M.P. Hehlen, T. Riedener, H.U. Gudel, Journal of Luminescence, 76 & 77 (1998) 447 - 550.

[5]. W. Zhao, D. Hreniak, G. Buolon, W. Strek, A. Brenier, M. Yin, P. Gluchowski, A. Lukowiak, R. Wiglusz, T. Epicier, Radiation Measurements, 45 (2010) 304 - 306.

[6]. R. Zhuo, X. Wei, C. Duan, Y. Chen, M. Yin, ECS Journal of Solid State Science and Technology, 1 (2012) 147 - 152.

[7]. G.F. Ansari, S.K. Mahajan, Journal of Luminescence, 156 (2014) 97 - 101.

[8]. D.M. Giolando, Solar Energy, 97 (2013) 195 - 199.

[9]. K. Laishram, R. Mann, N. Malhan, Ceramics International, 38 (2012) 1703 - 1706.

[10]. G. Rani, P.D. Sahare, International Journal of Applied Ceramics Technology, 12 (2015) 124 - 132.

[11]. Y. Wu, D.N. Ruzic, J.F. Stubbins, Deposition of aluminium oxide by evaporative coating at atmospheric pressure, MSc Thesis, (2013), University of Illinois at Urbana-Champaign, Illinois, Urbana.

[12]. A. Tougerti, C. Methivier, S. Cristol, F. Tielens, M. Che, X. Carrier, Physical Chemistry Chemical Physics, 13 (2011) 6531 - 6543.

[13]. K. Brandenburg, Diamond Version 3.0 d, (2005) Crystal Impact GbR, Bonn, Germany.

[14]. M. Tang, X. Wang, D. Peng, W. Wang, H. Sun, X. Yao, Journal of Alloys and Compounds, 529 (2012) 49 - 51.

[15]. W.-L. Feng, Optik 120 (200) 696 - 698.

[16]. H.A.A. Seed Ahmed, O.M. Ntwaeaborwa, R.E. Kroon, Current Applied Physics, 13 (2013) 1264 - 1268.

[17]. K.G. Tshabalala, S,-H. Cho, J.-K. Park, S.S. Pitale, I.M. Nagpure, R.E. Kroon, H.C. Swart, O.M. Ntwaeaborwa, Journal of Alloys and Compounds, 509 (2011) 10115 - 10120.

[18]. J.K. Krebsa, U. Happek, Journal of Luminescence, 94 (2001) 65 - 68.

[19]. K.H. Yoon, J.H. Kim, Journal of the Korean Physical Society, 59 (2011) 3093 - 3096.

[20]. L. Truffault, M,-T. Ta, T. Devers, K. Konstantinov, V. Harel, C. Simmonard, C. Andreazza, I.P. Nevirkovets, A. Pineau, O. Veron, J.-P. Blondeau, Materials Research Bulletin, 45 (2010) 527 - 535.

[21]. S.V. Motloung, F.B. Dejene, H.C. Swart, O.M. Ntwaeaborwa, Ceramics International, 41 (2015) 6776 - 6783.

[22]. A. Boumaza, A. Djelloul, F. Guerrab, Powder Technology, 201 (2010) 177 - 180.

[23]. A. Stierle, F. Renner, R. Stierle, H. Bosch, W. Brube, B.C. Cowie, Science, 303 (2004) 1652 - 1656.

[24]. K.R. Nemade, S.A. Waghuley, Ceramics International, 40 (2014) 6109 - 6113.

[25]. B. Hu, M. Yao, R. Xiao, J. Chen, X. Yao, Ceramics International, 40 (2014) 14133 - 14139.

[26]. S. Singh, V.C. Srivastava, T.K. Mandal, I.D. Mall, Royal Society of Chemistry Advances, 4 (2014) 50801 - 50810.

[27]. J. Gangwar, K.K. Dey, K, P, S.K. Tripathi, A.K. Srivastava, Advanced Materials Letters, 6 (2011) 402 - 408.

[28]. S.N. Ogugua, S.K.K. Shaat, H.C. Swart, O.M. Ntwaeaborwa, Journal of Physics and Chemistry of Solids, 83 (2015) 109 - 116.

[29]. P.P. Mokoena, M. Gohain, B.C.B. Bezuidenhoot, H.C. Swart, O.M. Ntwaeaborwa, Journal of Luminescence, 155 (2014) 288 - 292.

[30]. G.S. Huang, X.L. Wu, Y.F. Mei, X.F. Shao, G.G. Siu, Journal of Applied Physics, 93 (2003) 582 - 585.

[31]. A. Nourmohammadi, S.J. Asadabadi, M.H. Yousefi, M. Ghasemzadeh, Nanoscale Research Letters, 7 (2012) 689 - 696.

[32]. B.N. Kim, K. Hiraga, K. Morita, H. Yoshida, T. Miyazaki, Y. Kagawa, Acta Materialia, 57 (2009) 1319 - 1326.

[33]. L. Li, H. Lin, X. Zhao, Y. Wang, X. Zhou, C. Ma, X. Wei, Journal of Alloys and Compounds, 586 (2014) 555 - 560.

[34]. P. Goldner, F. Pelle, D. Meichenin, F. Auzel, Journal of Luminescence, 71 (1997) 137 - 150.

[35]. A. Denoyer, Y. Levesque, S. Jandi, P. Goldner, O. Guollot-Noel, B.Viana, F. Thibault, D. Pelenc, Journal of Luminescence, 128 (2008) 1389 - 1393.

[36]. Y. Dwivedi, S.C. Zilio, Optical Society of America, 21 (2013) 4717 - 4727.

[37]. A. Jusza, K. Anders, A. Jastrzebska, P. Polis, A. Olszyna, M. Kus, A. Kunicki, R. Piramidowicz, Optical Materials, 33 (2011) 1487 - 1491.

6. The study of the structural properties and up-conversion luminescence in TiO_2:Er^{3+} nano-phosphor

6.1 Introduction

More attention has been focused on up-conversion luminescence nano-materials such as rare-earths doped in nanocrystals because of their wide range of applications in photonics, frequency up-converters, biological fluorescence labels, undersea optical communications, solar cells and temperature sensors. The generation of high-energy light (visible photons) induced by low energy excitation (near infrared photons) is called up-conversion, while the generation of visible emission by high-energy photons (UV) excitation is known as down-conversion [1-3]. Among all the rare-earth dopant ions, erbium (Er^{3+}) is widely investigated because of its many energy levels and potential infrared applications. This rare-earth ion displays up-conversion luminescence with maxima at 410, 550, 660, 810 and 980 nm corresponding to the transitions from the excited $^2H_{9/2}$, $^4S_{3/2}$, $^4F_{9/2,}$ $^4I_{9/2}$ and $^4I_{11/2}$ states to the ground $^4I_{15/2}$ state of Er^{3+}. Er^{3+}-doped phosphors can be used to enhance silicon solar cells response in the infrared spectral region and can also enhance the efficiency of dye-sensitized solar cells (DSSCs). The up-conversion luminescence from Er^{3+}-doped phosphors can be reabsorbed by dyes in the DSSCs. More solar irradiation may be used, and the DSSC photocurrent will be effectively enhanced. In addition, the ruthenium dyes in DSSC such as N719, N3 and N749 only absorb visible light in the spectral range of 300 – 800 nm [4-6].

Titania (TiO_2) is one of the suitable host of rare-earths ions especially for up-conversion phosphors because of its good physical and chemical stability, non-toxicity, anti-corrosiveness and wide bandgap [7] among other things. There are three polymorphs of TiO_2, namely brookite, anatase and rutile. The anatase phase of TiO_2 has potential applications in gas sensors, catalysts and it can also be used for pigments because of its excellent chemical and physical properties [8]. The rutile phase is thermodynamically stable at high temperatures between 600 and 1000 ^oC. It is therefore advisable to use low-temperature synthesis route to prepare anatase phase, in order to prevent the conversion of rutile phase [9]. The doping of rare-earths in TiO_2 inhibit the phase transformation of anatase to rutile phase by stabilizing the anatase phase this may be caused by surrounding rare-earths ions in anatase phase [10,11]. Huang et al. [12] investigated Pr^{3+}-doped TiO_2 nanocatalysts prepared by sol-microwave. The results indicated that inhibition of the anatase –rutile phase transformation was due to Pr^{3+} doping and therefore, the results were also consistent with the previous studies [12], [13,14].

In the present study, $TiO_2:Er^{3+}$ powder nano-phosphor was successfully synthesized by sol-gel method at room temperature and the powder was annealed at 650 ^{o}C. The structural properties were carried out by powder x-ray diffractometer (XRD) and the undoped TiO_2 exhibited mixed phases of anatase and rutile with average crystallite size of 26 nm. The green and red up-conversion emission from $TiO_2:Er^{3+}$ were studied by photoluminescent (PL) spectroscopy using the 980 nm fibre-coupled laser as the excitation source. Other characterization techniques such as field emission scanning electron microscope (FE-SEM) coupled with energy dispersive x-ray spectroscopy, Fourier transform infrared (FTIR), and ultraviolet-visible (UV-vis) spectrophotometer were used to analyze nano-phosphor samples. The influence of Er^{3+} concentrations in TiO_2 nanocrystal on structural and up-conversion luminescence was investigated.

6.2 Experimental procedure

6.2.1 Synthesis

Figure 6.1 presents the schematic diagram of the synthesis procedure of $TiO_2:Er^{3+}$ nano-phosphor powder. In a typical preparation, 5 ml titanium (IV) butoxide was added into a mixture of 50 ml ethanol and acetic acid and was stirred vigorously for 5 min. The reaction stopped after stirring for further 60 min and the milky solution was obtained. The solution was aged for 24 hours and it was transformed to a gel during that period. The gel was dried in an oven maintained at 100 ^{o}C for 2 hours to ensure that all organic solvents have evaporated, and the resulting powder was annealed at 650 ^{o}C for 2 hrs in air. The resulting powders were ground using pestle and mortar. $TiO_2:Er^{3+}$ phosphor powders with Er^{3+} concentrations of 0.5, 1.0, 1.5 and 2.0 mol % were prepared [15].

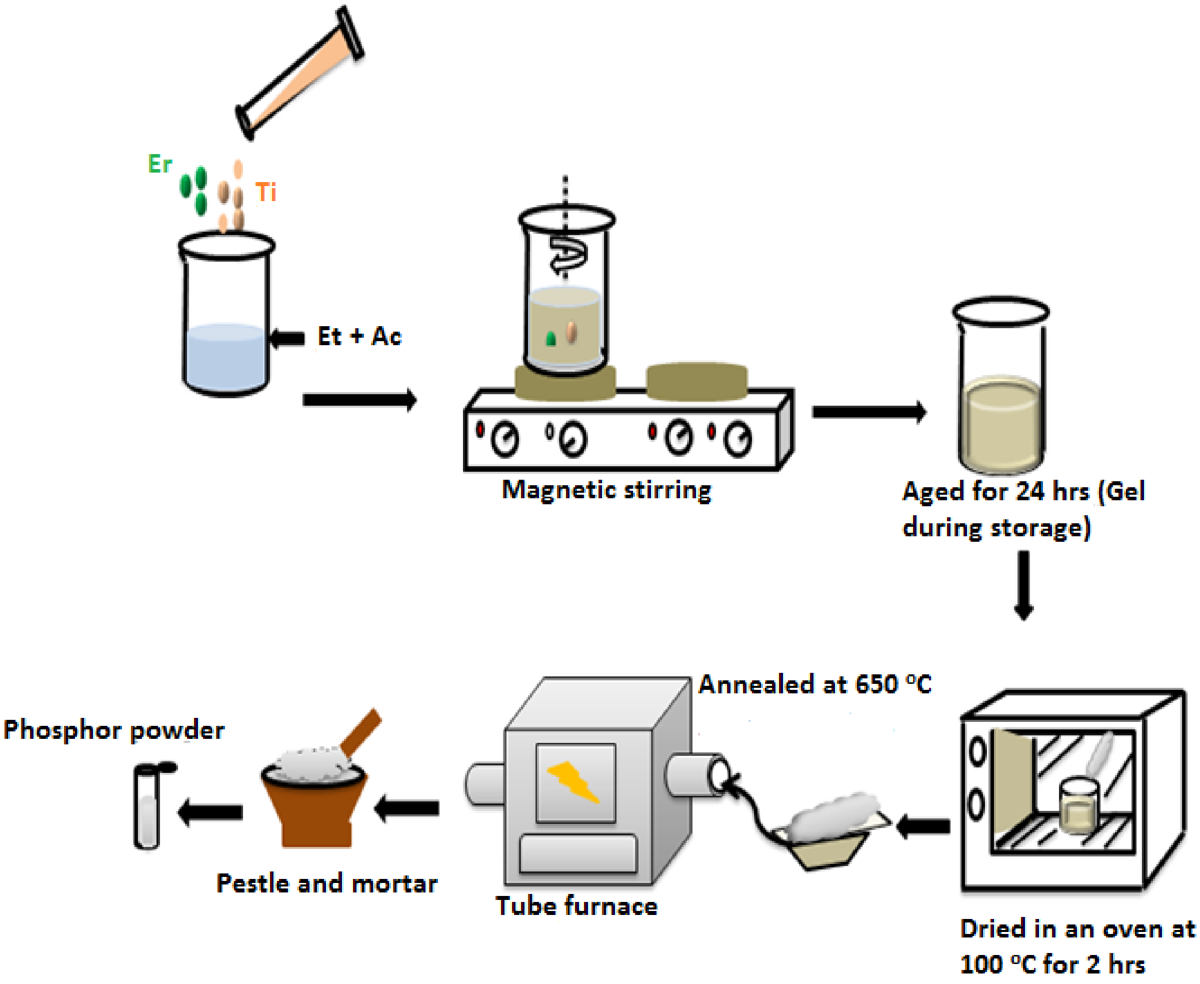

Figure 6.1: Schematic diagram of the synthesis procedure of TiO_2:Er^{3+} nano-phosphor powder (Ti = titanium (IV) butoxide, Er = erbium (III) acetate hydrate, Et = ethanol and Ac = acetic acid).

6.2.2 Characterization

The crystal structure of the nano-phosphor was analyzed using a Bruker D8 Advanced powder X-ray diffractometer (XRD) with CuK_α radiation wavelength of 0.154 nm. The particle morphology and chemical composition analyses were carried out using JEOL JSM-7800 field emission scanning electron microscope (FE-SEM) coupled with energy dispersive x-ray spectroscopy (EDS). The diffuse reflectance measurements were performed using Lambda 950 spectrophotometer. The study of vibrational bonds of the material was carried out by Fourier transform infrared (FTIR). Up-conversion measurements were performed by using fiber-coupled 980 nm NIR laser as the excitation source coupled with a monochromator, photomultiplier tube (PMT) detector and a lock-in amplifier.

6.3 Results and Discussion

6.3.1 Structure and morphology

Figure 6.2 presents the XRD patterns of TiO_2:Er^{3+} phosphor powders. The patterns are consistent with tetragonal phase of TiO_2 with space groups of $l\frac{4_1}{a}$md and $P\frac{4_2}{m}$nm referenced in JCPDS file number 21-1272 (anatase) and 75-1755 (rutile), respectively. It is clear that the undoped patterns consist of anatase and rutile phases of TiO_2. Some of the rutile peaks disappeared with increasing concentration of Er^{3+} ion. The intensity of the (110) and the (101) diffraction peaks of both the rutile and anatase phases, respectively, as a function of Er^{3+} concentration are compared in the bar graph shown in figure 6.3. The peak intensity for rutile phase in the undoped sample was 1672 a.u, while for anatase was 1182 a.u. In doped samples rutile intensity decreases while that of anatase increases with increasing concentration of Er^{3+}. This indicates that the Er^{3+} dopants in titania inhibit anatase-rutile phase transformation. Rao et al. [10] suggested that all dopants in TiO_2, both the donor and acceptor cations and anion dopants, prevent the anatase-rutile phase transformation by stabilizing the anatase phase of TiO_2. There is a relationship between the degree of inhibition, size and ionic character of the dopants. The additives of dopants with a high charged such as Er^{3+} seemed to stabilize the anatase phase more strongly than those with a lower charge [10]. However, no diffraction peaks detected from impurities of erbium due to the low concentration of Er^{3+} in the host.

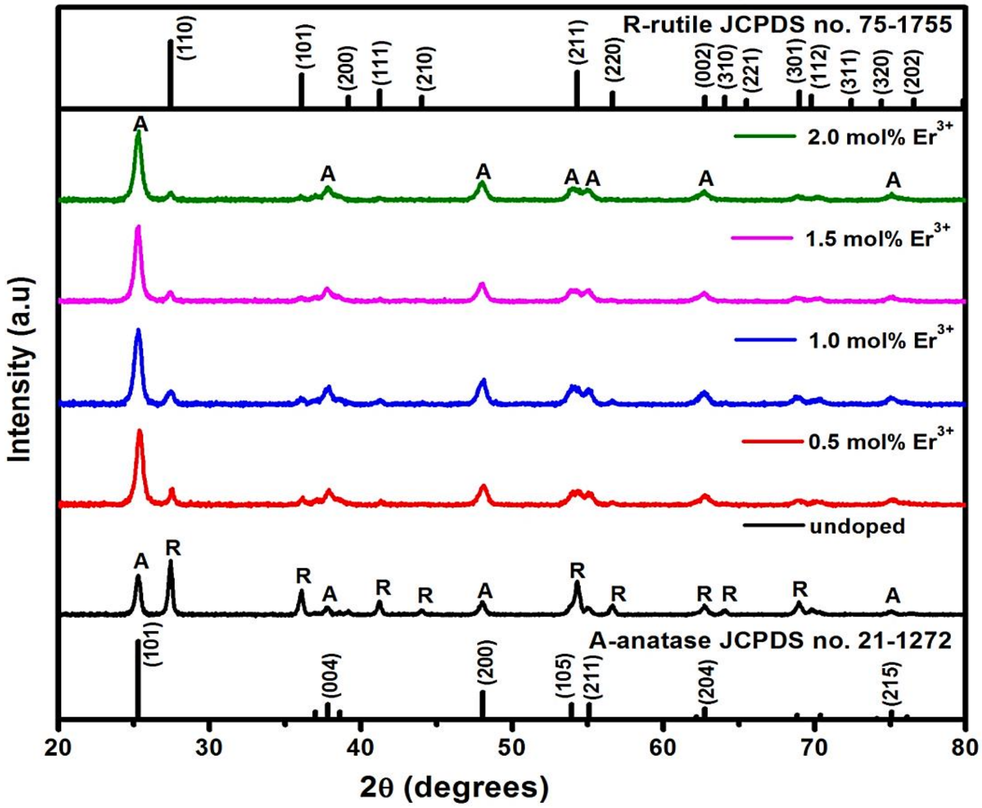

Figure 6.2: XRD patterns of $TiO_2:Er^{3+}$ nano-phosphor powder.

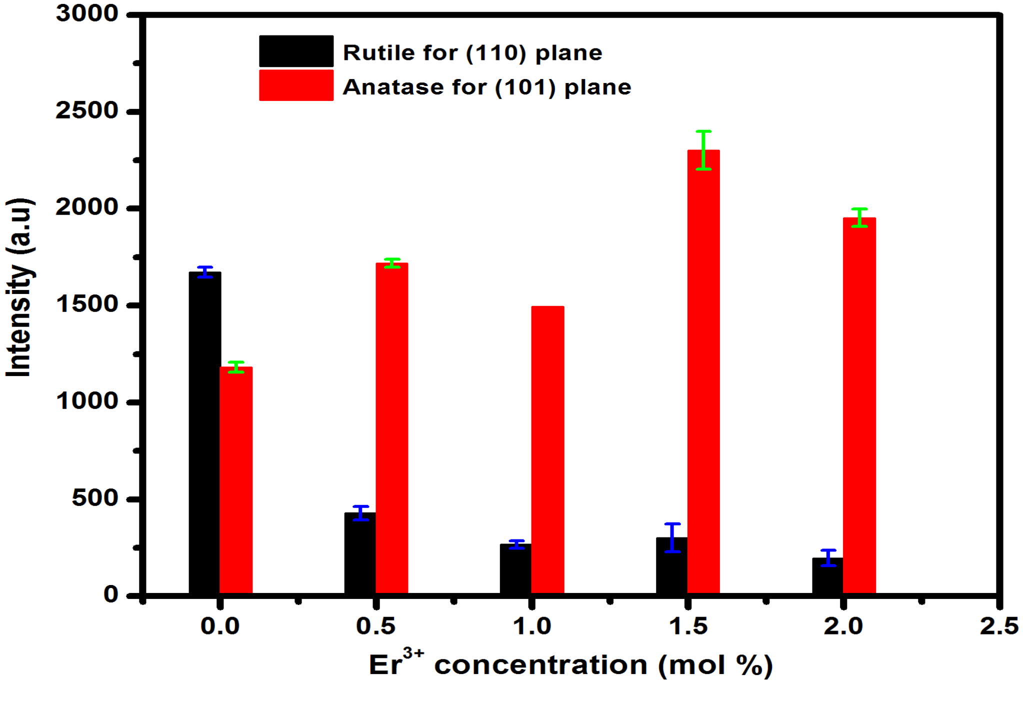

Figure 6.3: The bar graph of XRD intensity against Er^{3+} concentration for rutile (110) and anatase (101) planes.

The average crystallite size D was estimated from the Debye-Scherrer equation:

$$D = \frac{K\lambda}{\beta cos\theta} \tag{6.1}$$

where K is the shape factor ~ 0.9, λ is the x-ray wavelength and β is the full-width half at maximum (FWHM) of the x-ray peak at the Bragg angle θ. The average D of the undoped TiO_2 nano-phosphor was 26 nm. The doped samples show crystallite size of 15, 14, 12 and 11.5 nm for 0.5, 1.0, 1.5 and 2 mol% Er^{3+}. This reduction is attributed to the retarded crystallite growth upon the addition of Er^{3+} [12,16,17]. Figure 6.4 presents a crystal structure of anatase (a) and rutile phase (b) of TiO_2. The crystal structure of anatase and rutile phase is tetragonal with space group of $l\frac{4_1}{a}$md and $P\frac{4_2}{m}$nm, respectively. Both the structures consist of TiO_6 octahedron, whereby the ionic radii for Ti^{4+} and O^{2-} are 0.068 nm and 0.10 nm, respectively. Therefore, ionic radius of Er^{3+} (0.089 nm) is between that of Ti^{4+} and O^{2-} so it can either replace Ti^{4+} ions or occupy the interstitials site. Theoretical dimensions of anatase unit cell are: $a = b = 0.3872\, nm$ and $c = 0.9616\, nm$, while for rutile unit cell are : $a = b = 0.4594\, nm$ and $c = 0.2959\, nm$ [18]. The experimental lattice parameters for anatase unit cells were $a = b = 0.3786\, nm$ and $= 0.9504\, nm$, while for rutile unit cell whereas $a = b = 0.4598\, nm$ and $c = 0.2958\, nm$ which were consistent with the theoretical values of both crystal structures. Table 6.1 summarizes the crystallographic planes (miller indices) corresponding to different Bragg angles and the experimental and theoretical d-spacing for anatase and rutile phase of TiO_2. The experimental values of lattice parameters and d-spacing were calculated by using tetragonal system [19] given by:

$$\frac{1}{d^2} = \frac{h^2+k^2}{a^2} + \frac{l^2}{c^2} \tag{6.2}$$

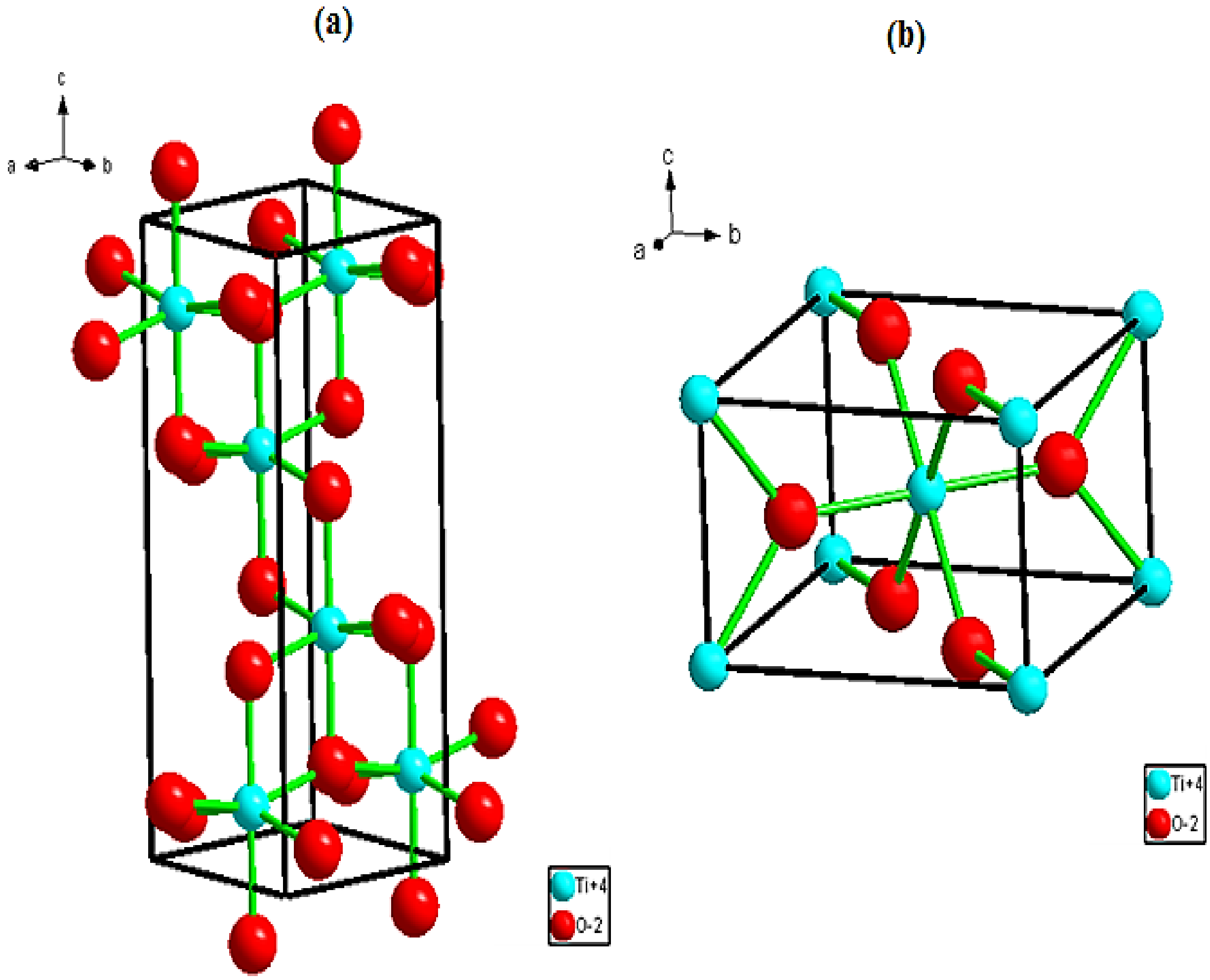

Figure 6.4: Crystal structure of TiO_2 anatase (a) and rutile phase (b) drawn by the Diamond crystal software [20].

Table 6.1: The crystallographic planes corresponding to different Bragg angles and the experimental and theoretical d-spacing values for anatase and rutile phases of TiO_2.

2θ (deg)	Anatase (hkl)	Rutile (hkl)	Anatase d-spacing (nm) Experimental	Anatase d-spacing (nm) Theoretical	Rutile d-spacing (nm) Experimental	Rutile d-spacing (nm) Theoretical
25.281	101	-	0.3512	0.35200		
27.436	-	110			0.3251	0.3248
36.080	-	101			0.2488	0.2487
37.801	004	-	0.2376	0.2378		
41.240	-	111			0.2188	0.2187
44.043	-	210			0.2056	0.2054
48.050	200	-	0.1889	0.1892		
54.321	-	211			0.1688	0.1688
55.062	211	-	0.1664	0.1667		
56.621	-	220			0.1625	0.1624
62.759	-	002			0.1479	0.1479
64.047	-	310			0.1454	0.1453
69.004	-	301			0.1360	0.1360
75.032	215	-	0.1263	0.1265		

The FE-SEM micrographs of low (a) and high magnification (b) of TiO_2:Er^{3+} phosphor powders are shown in figure 6.5. The low magnification of TiO_2:Er^{3+} (Fig 6.5 (a)) shows a network of nano-rods with diameter and length of 78 ± 36 nm and 1.51 ± 0.30 µm, respectively while in high magnification (Fig 6.5(b)) it was seen that these nano-rods formed from a combination of spherical and porous nanoparticles.

The EDS spectra of (a) undoped and (b) Er^{3+} doped TiO_2 are shown in figure 6.6. The inset in the right center and top middle, respectively in figure 6.6 (a) and (b) demonstrate the FE-SEM micrographs and the positions where EDS analysis was performed. The top right corner depicts the bar graph comparing the weight % of the elements at the chosen area in figure 6.6 (a) and (b). All the elements present were detected. Carbon is probably coming from the tape on which the powders were mounted [21]. In figure 6.6 (a) the EDS analysis reveals the weight content of Ti and O to be approximately 58.3 % and 35.0 % respectively, giving the atomic content ratio Ti/O of 35.8/64.3 to be 0.56. In figure 6.6 (b) EDS spectra of doped sample exhibits the weight content of Ti, O and Er to be 52.8 %, 43.2 % and 1.2 % respectively, giving the atomic content ratio Ti/O of 28.9/70.9 to be 0.41. These results verifies the formation of titania particles in (Fig. 6.6(a)) to a large extent than in doped sample (fig. 6.6 (b)) suggesting that the dopant (Er^{3+}) substitutes Ti^{4+} ions in the host.

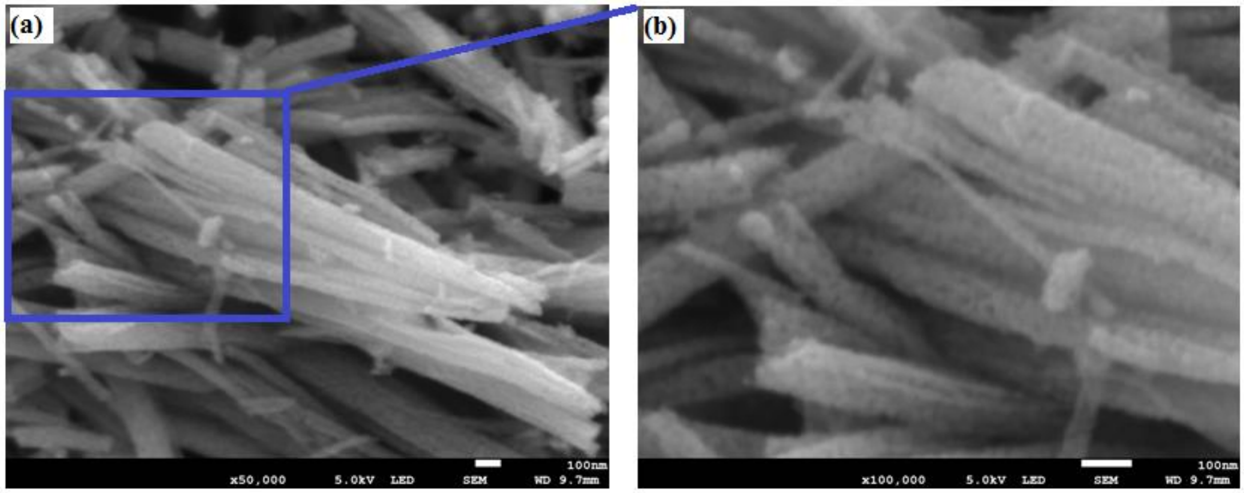

Figure 6.5: FE-SEM micrographs of low (a) and high magnification (b) of TiO_2:Er^{3+} phosphor powder.

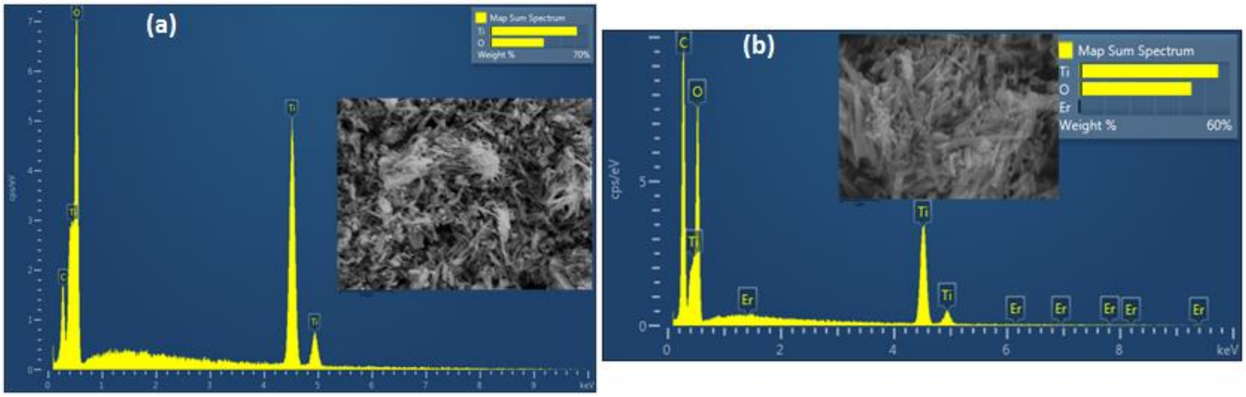

Figure 6.6: EDS spectra of undoped (a) and doped TiO_2: Er^{3+} (b) nano-phosphor powder.

6.3.2 UV-vis and optical bandgap

The diffuse reflectance spectra (DRS) were used to measure the absorption properties of TiO_2 and the effects of Er^{3+} in figure 6.7. The results indicate the strong UV absorption below a wavelength of 420 nm which is due to wide band gap of 3.2 eV and 3.0 eV for anatase and rutile phase, respectively. There was a blue shift in UV band-to-band absorption as the concentration of Er^{3+} ion increased. The inset shows six absorption bands in visible to near-infrared (NIR) region centered at 452, 490, 524, 548, 655 and 798 nm assigned to the transitions from ground $^4I_{15/2}$ state to excited $^4F_{3/2}$, $^4F_{7/2}$, $^2H_{11/2}$, $^4S_{3/2}$, $^4F_{9/2}$ and $^4I_{9/2}$ states of Er^{3+} ion, respectively [22].

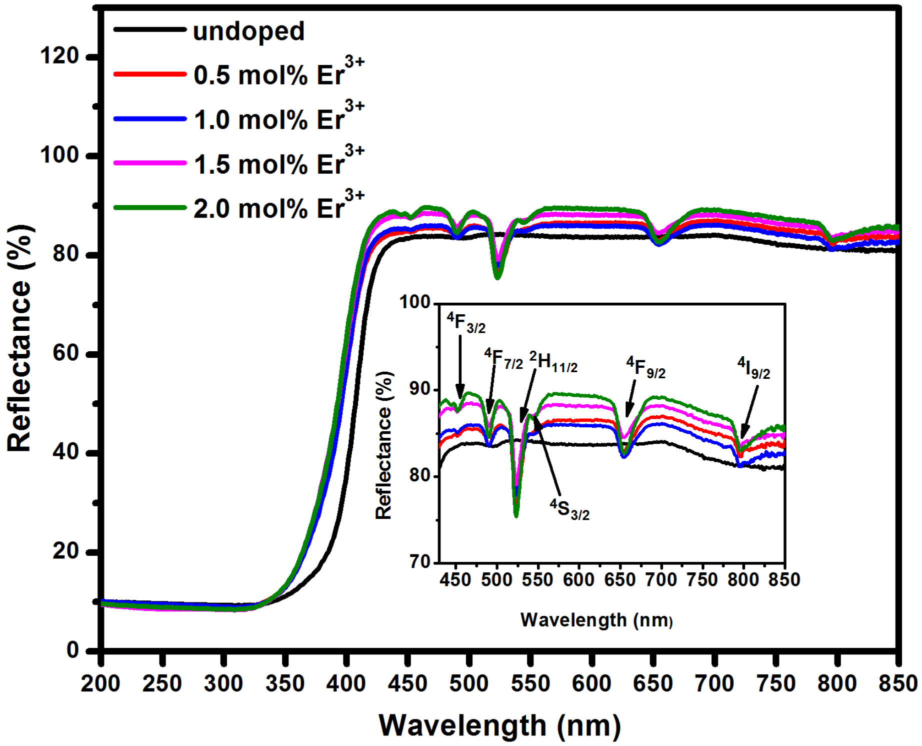

Figure 6.7: DRS of TiO_2 :Er^{3+} nano-phosphor powder.

The optical indirect bandgap of TiO_2 was estimated by Tauc plot of $(\alpha h\nu)^n$ against $h\nu$, with n = ½ which is correct for allowed indirect transition in material such as TiO_2 (shown in figure 6.8) [23]. The energy bandgap for the host TiO_2 nano-phosphor was 2.94 eV and doped samples were 2.968, 2.974, 2.995 and 3.003 eV corresponding to 0.5, 1.0, 1.5 and 2.0 mol% Er^{3+}, respectively. The energy bandgap and crystallite size as a function of Er^{3+} concentration were plotted and shown in figure 6.9. The increase of energy bandgap is due to the upshift of the Fermi level that is located deep inside the conduction band due to excess of electrons from Er^{3+} ion. These phenomena can be explained further by applying density functional theory (DFT) calculations. In addition, when the particle size decreases from its bulk to that of Bohr radius, the concepts of quantum size effect arises due to the spatial confinement of charge carriers. The electrons and holes in the quantum sized are confined in a potential well and do not experience the delocalization that occurs in the bulk phase. Therefore, the energy bandgap of the material increases with the decrease in particle size [24]. These results suggest that the doping of Er^{3+} ion plays an important role in altering the photoabsorption of TiO_2 [25].

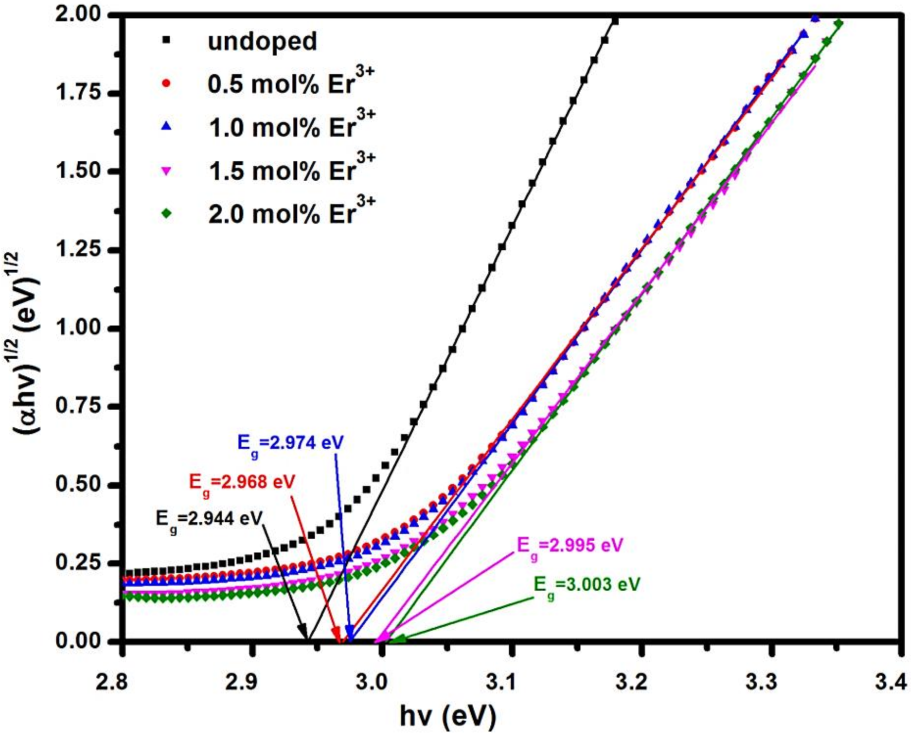

Figure 6.8: Tauc plot of indirect bandgap for $TiO_2:Er^{3+}$ nano-phosphor powder.

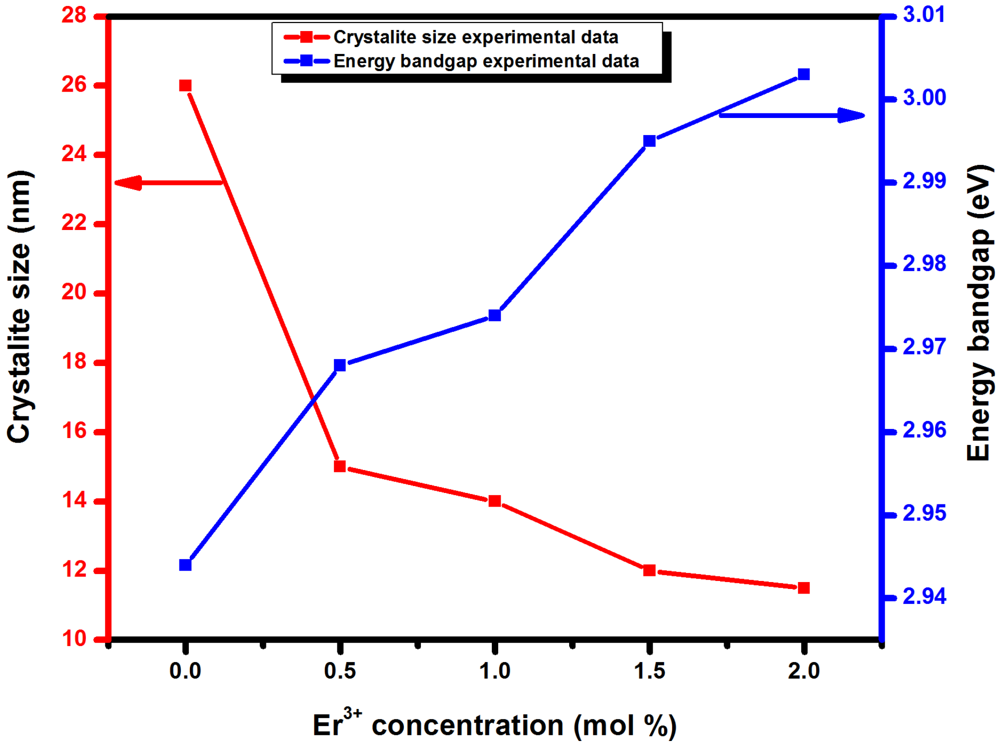

Figure 6.9: Energy bandgap and crystallite size as a function of Er^{3+} concentration in TiO_2:Er^{3+} nano-phosphor powder.

6.3.3 FTIR analysis

Figure 6.10 presents the FTIR spectra of undoped TiO_2 and doped TiO_2: 2 mol% Er^{3+} nano-phosphor. There were four absorption bands centered at 750, 1598, 2367 and 3456 cm^{-1}. The results indicate the characteristic peak of titania at 750 cm^{-1} which was assigned to Ti-O stretching vibration due to the presence of octahedral TiO_6 group. The weak peak at 1598 cm^{-1} can be assigned to unsaturated bonds (C=C) from precursors such as butene, ethene etc. or perhaps from the hydroxyl (O-H) group. The peak at 2367 cm^{-1} is assigned to hydrocarbon C-H vibrations due to the organic residues, which remain in a host TiO_2 after annealing or calcination. In addition, the same absorption bands can also be assigned to CO_2 atmospheric. The peak at 3456 cm^{-1} is assigned to O-H vibration from the moisture of KBr pellet. It is clearly seen that the peaks of doped TiO_2:Er^{3+} are more broad than those of undoped, which means surface of doped samples might be attached to hydroxyl groups and have stronger adsorption [26].

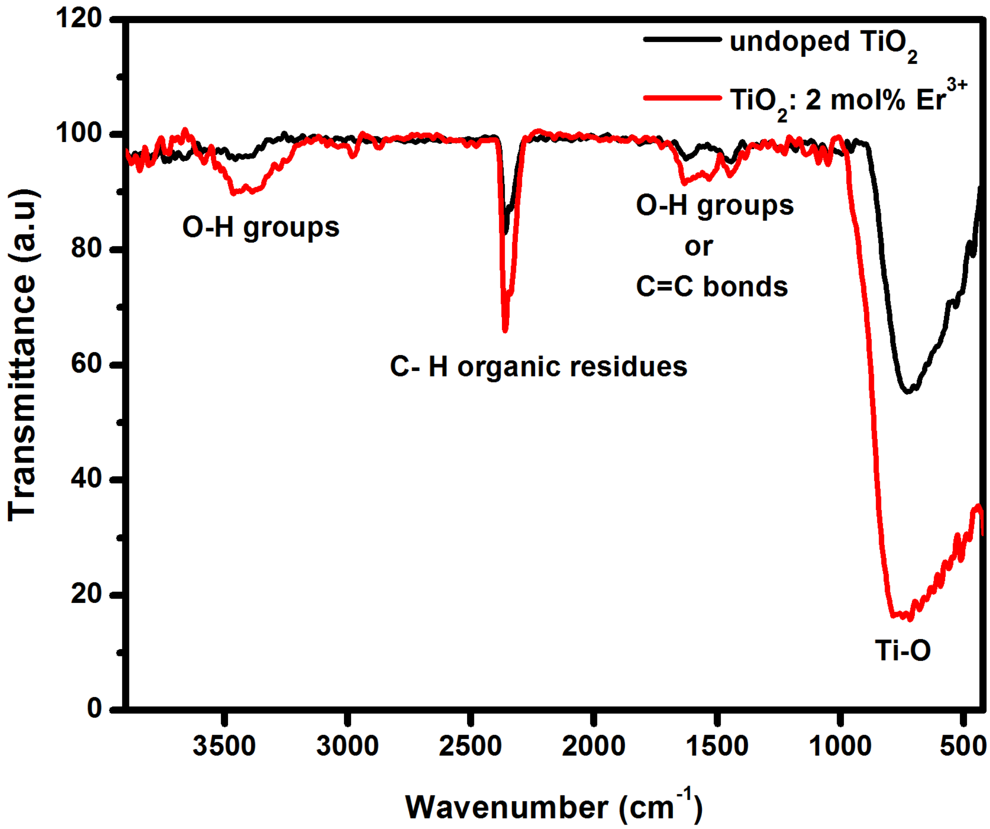

Figure 6.10: FTIR spectra of undoped TiO_2 and doped TiO_2: 2 mol% Er^{3+}nano-phosphor powder.

6.3.4 Up-conversion properties

Figure 6.11 shows the up-conversion emission of TiO_2:Er^{3+} nano-phosphor excited by 980 nm. The green emission with maxima at 527 and 564 nm are assigned to $(^2H_{11/2}, {}^4S_{3/2}) \rightarrow {}^4I_{15/2}$ transitions and the red emission with maxima at 665 nm is assigned to the $^4F_{9/2} \rightarrow {}^4I_{15/2}$ transition of Er^{3+} ions [27]. The different emission bands are observed corresponding to electronic configuration of f→f transitions of the Er^{3+} ion. The broadening shown by emission bands with maxima at 665 nm is due to the contribution of optically active Er^{3+} ions in different local sites with small difference in bond lengths and angles. This arises from the crystal-field interaction experienced by Er^{3+}, as well as to the intrinsic splitting of stark levels [28]. The weak red emission is very broad because of the local crystal field symmetry at the rare-earth site [29]. The rutile phase has TiO_6 octahedral that share edges, while in the anatase phase TiO_6 octahedral share faces. Thus, the crystal field is not identical for the Er^{3+} ions in the different crystal phases. Therefore, the emission from both anatase and rutile phases are not the same [30,31]. The inset presents the chromaticity coordinates of TiO_2: Er^{3+} nano-phosphor powders under excitation of 980 nm laser and were determined using the Commission International de I'Eclairage (CIE) coordinate calculator software. The coordinates of nano-phosphor powders display yellowish-green visible colour. The PL intensity of green and red emission as a function of the Er^{3+} concentration is shown in figure 6.12. These results depict the decrease in green emission as the concentration of Er^{3+} was increased. This indicates that Er^{3+} ion in low concentration is well distributed in the host and inter-ionic distance is too far in Er^{3+}-Er^{3+} ions. However, in a high concentration the inter-ionic distance of Er^{3+}-Er^{3+} ions is small and this results in the formation of Er^{3+} cluster. Thus, concentration quenching process is mostly to occurs which causes the non-radiative relaxation processes [31-33].

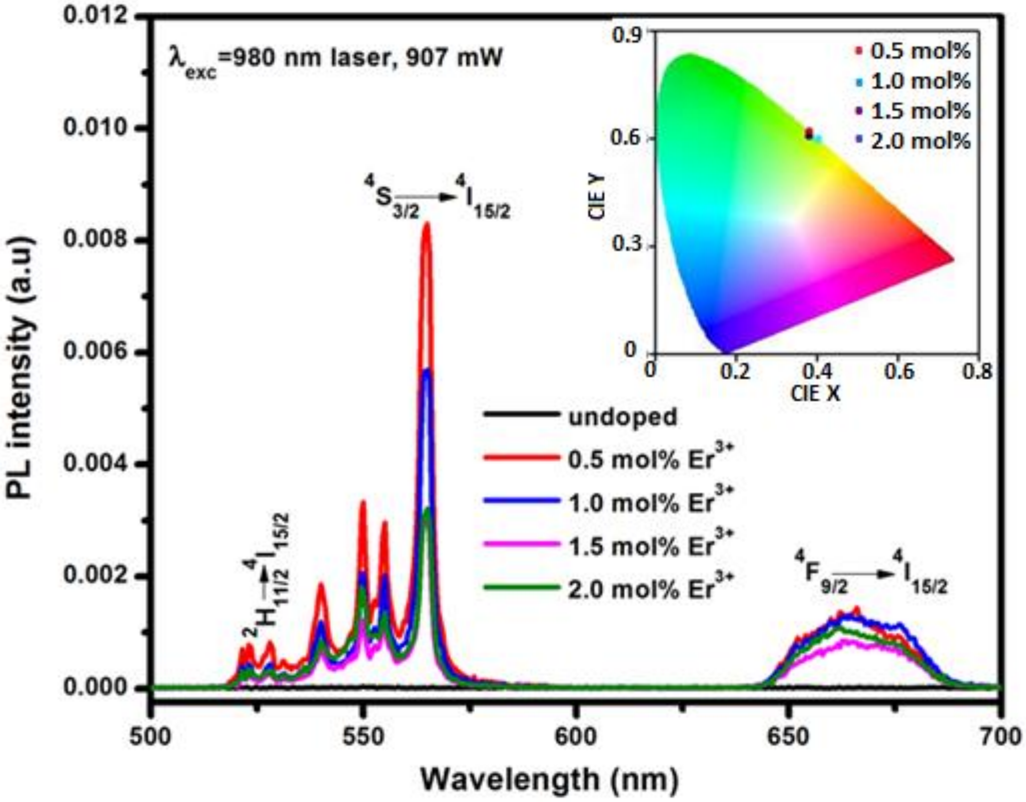

Figure 6.11: Up-conversion emission TiO_2: Er^{3+} nano-phosphor excited by 980 nm.

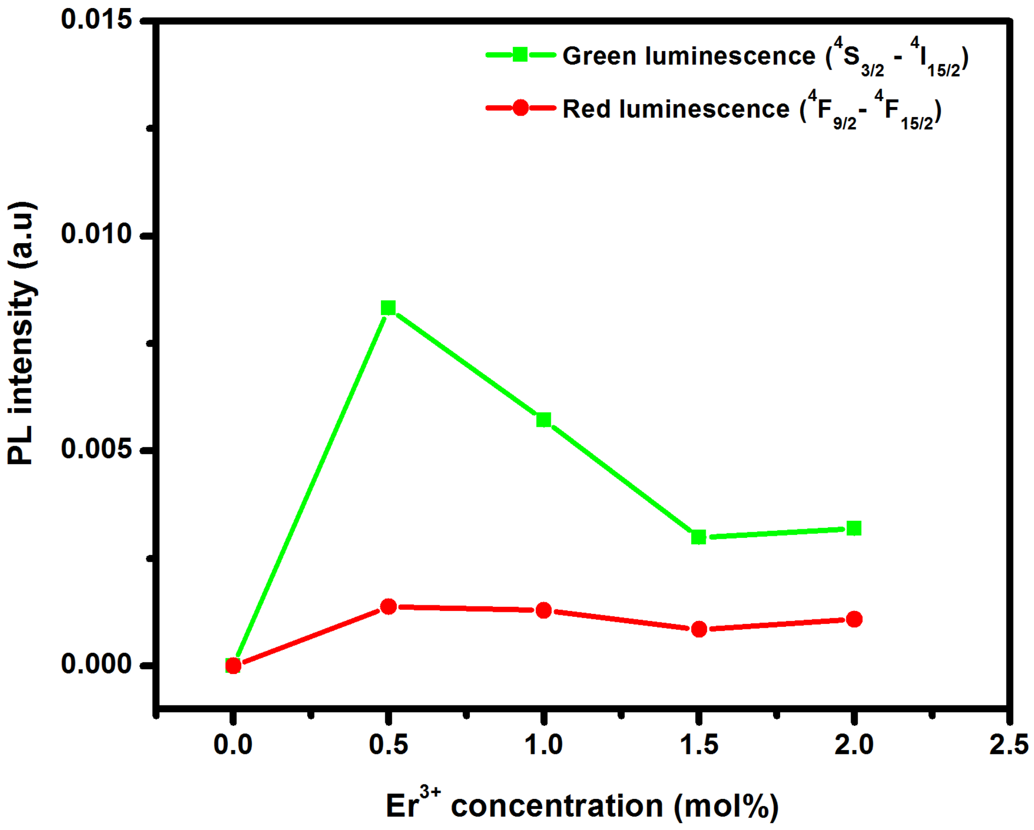

Figure 6.12: PL intensity as a function of Er^{3+} concentration.

The mechanism of up-converted emission of TiO_2:Er^{3+} nano-phosphor is illustrated in figure 6.13. In the ground state absorption (GSA) process, the wavelength of excitation laser 980 nm matches with the absorption transition from the ground state $^4I_{15/2}$ to the $^4I_{11/2}$ level. After GSA process, the same laser pumps the excited atom from the $^4I_{11/2}$ to the $^4F_{7/2}$ level; the process is called excited state absorption (ESA). There was a non-radiative relaxation from $^4F_{7/2}$ to $^4S_{3/2}$/ $^2H_{11/2}$ and $^4F_{9/2}$ levels. The green emission were seen at 527 nm and 564 nm attributed to the ($^2H_{11/2}$, $^4S_{3/2}$)→$^4I_{15/2}$ transitions while red emission at 665 nm is assigned to the $^4F_{9/2}$→$^4I_{15/2}$. At the low concentration of Er^{3+} ion $^2H_{11/2}$/ $^4S_{3/2}$ levels shows radiative decay to the ground level $^4I_{15/2}$ which gives the higher intensity of the green emission. The cross-relaxation (CR) process between $^4I_{15/2}$→$^4I_{13/2}$ and $^4F_{9/2}$→$^4I_{15/2}$ transitions was seen and this process is mostly to occur at high concentration of Er^{3+} ions. In addition, the luminescence lifetime of $^4S_{3/2}$/ $^2H_{11/2}$ levels is shortened and therefore, the quenching of green emissions is observed. Thus, it is evident from the results that up-conversion process is a concentration dependent [32-33].

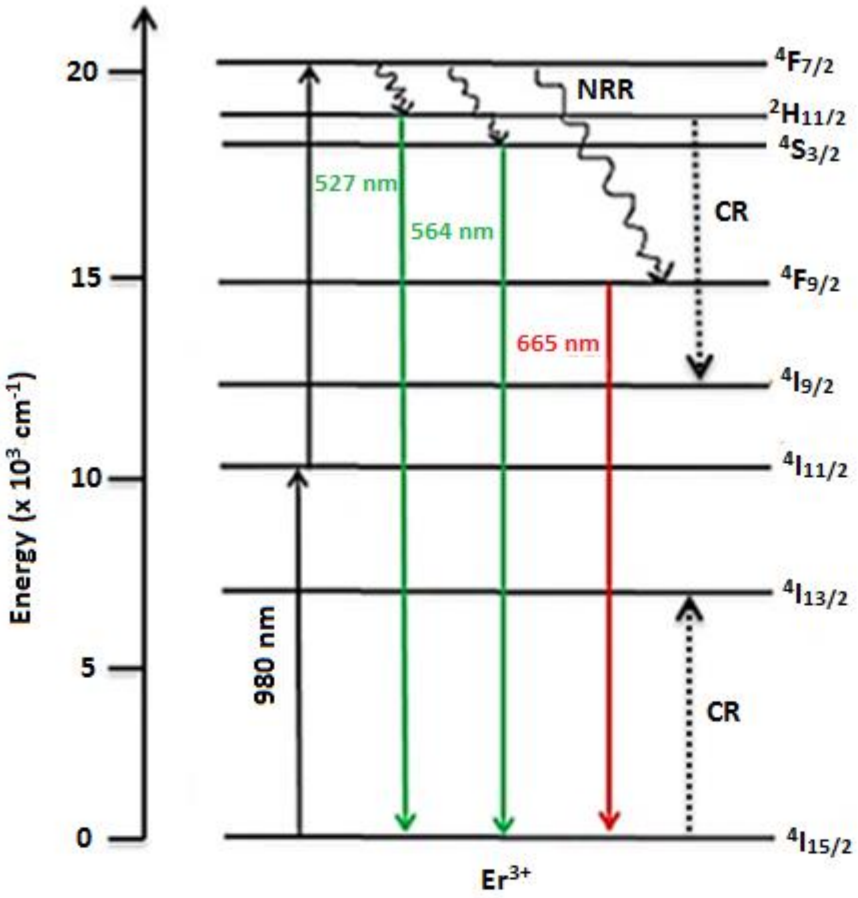

Figure 6.13: The mechanism of up-converted emisson in TiO_2: Er^{3+} nano-phosphor powder (CR - Cross relaxation and NRR - nonradiative relaxation).

6.4 Conclusion

The TiO_2:Er^{3+} nano-phosphor powder has been successfully synthesized by sol-gel method at room temperature preparation and the powder was annealed at 650 °C to form a desired phase. XRD confirms that nano-phosphor has crystallized in the tetragonal phases of anatase and rutile with space groups of $\frac{4_1}{a}$md and $P\frac{4_2}{m}$nm, respectively. XRD confirms reduction in crystallite size when the concentration of Er^{3+} increases. The increase of Er^{3+} concentration increases the energy bandgap due to quantum size effect. FE-SEM confirms nano-rods morphology with diameter and length of 78 ± 36 nm and 1.51 ± 0.30 µm, respectively. All vibration bonds for Ti-O were observed at FTIR due to the presence of TiO_6 octahedral group. The red and intense green up-conversion emission was observed from PL spectroscopy upon the excitation of 980 nm. The possible mechanism showing GSA and ESA of the Er^{3+} ion upon the excitation of 980 nm was illustrated and discussed. These results show that the addition of Er^{3+} in a host it is altering properties of TiO_2 by inhibiting anatase - rutile phase transformation, increases optical bandgap and prevent a particle growth. The green and red up-conversion emission shows that the nano-phosphor material has potential applications in DSSCs.

6.5 Reference

[1]. Z. Zhang, J. Zhang, W. Zhou, M. Song, W. Li, Q. Hu, X. Zhao, Advanced Materials Research, 66 (2009) 167 - 170.

[2]. Y. Qu, X. Kong, Y. Sun, Q. Zeng, H. Zhang, Journal of Alloys and Compounds, 485 (2009) 493 - 496.

[3]. A. Pandey, V.K. Rai, V. Kumar, V. Kumar, H.C. Swart, Sensors and Actuators B, 209 (2015) 352 - 358.

[4]. J. Yu, Y. Yang, R. Fan, H. Zhang, L. Li, L. Wei, Y. Shi, K. Pan, H. Fu, Journal of Power Sources, 243 (2013) 436 - 443.

[5]. N. Dyck, G. Demopoulos, Spectral engineering of dye sensitized solar cells through intergration $NaYF_4:Yb^{3+},Er^{3+}$ up-conversion nano-materials, M.Eng (Thesis), (2013), McGrill University, Montreal QC, Canada.

[6]. Q. Li, J. Lin, J. Wu, Z. Lan, Y. Wang, F. Peng, M. Huang, Electrochimica Acta, 56 (2011) 4980 - 4984.

[7]. X. Meng, C. Han, F. Wu, J. Li, Journal of Alloys and Componds, 536 (2012) 210 - 213.

[8]. D. Dastan, N.B. Chaure, International Journal of Materials Mechanics and Manufacturing, 2 (2014) 21 - 23.

[9]. K. Yanagisawa, J. Ovenstone, Journal of Physical Chemistry B, 103 (1999) 7781 - 7787.

[10]. C. Rao, A. Turner, J. Honig, Journal of Physical Chemistry of Solids, 11 (1959) 173 - 175.

[11]. J. Li, X. Yang, X. Yu, L. Xu, W. Kang, W. Yan, H. Gao, Z. Liu, Y. Guo, Applied Surface Science, 255 (2009) 3731 - 3738.

[12]. H. Fengping, W. Shuai, Z. Shuang, F. Yingge, L. Chunxue, W. Chuang, L. Chun, Bulletin of the Korean Chemical Society, 35 (2014) 2512 - 2518.

[13]. Z.P. Tshabalala, D.E. Motaung, G.H. Mhlongo, O.M. Ntwaeaborwa, Sensors and Actuators B: Chemical, 224 (2015) 841 - 850.

[14]. Q. Gao, X. Wu, Y. Fan, Dye and Pigments, 95 (2012) 96 - 101.

[15]. X. Meng, C. Han, F. Wu, J. Li, Journal of Alloys and Compounds, 536 (2012) 210 - 213.

[16]. Y. Zheng, W. Wang, Journal of Solid State Chemistry, 210 (2014) 206 - 212.

[17]. J.-Y, Kim, S.H. Kang, H.S. Kim, Y.-E, Sung, American Chemical Society Langmuir, 26 (2010) 2864 - 2870.

[18]. D.A.H. Hanaor, C.C. Sorrell, Journal of Material Science, 46 (2011) 855 - 874.

[19]. W. Massa, Crystal Structure Determination, (2000), Springer-Verlag, Berlin, Heidelberg, Germany, page 25.

[20]. K. Brandenburg, Diamond Version 3.0 d, (2005) Crystal Impact GbR, Bonn, Germany.

[21]. P.P. Mokoena, M. Gohain, B.C.B. Bezuidenhoot, H.C. Swart, O.M. Ntwaeaborwa, Journal of Luminescence, 155 (2014) 288 - 292.

[22]. A.K. Rai, I.M.L. Das, K.N. Uttum, Emerging Trends in Laser & Spectroscopy and Application, (2010), Allied Publsihers PVT. Ltd, New Delhi, India, page 362.

[23]. C. Strohhofer, A. Polman, Optical Materials, 21 (2003) 705 - 712.

[24]. H.Lin, C.P. Huang, W. Li, C. Ni, S.I. Shah, Y.-H. Tseng, Applied Catalysis B: Environment 68 (2006) 1-11.

[25]. Y. Peng, J. He, Q. Liu, Z. Sun, W. Yan, Z. Pan, Y. Wu, S. Liang, W. Cheng, S. Wei, The Journal of Physical Chemistry C, 115 (2011) 8184 - 8188.

[26]. M.M. Karkare, International Nano Letters, 4 (2014) 111 - 119.

[27]. G. Lakshminarayana, J. Qiu, M.G. Brik, G.A. Kumar, I.V. Kityk, Journal of Physics Condesed Matter, 20 (2008) 375101 - 375109.

[28]. L. Liang, Y. Yulin, Z. Mi, F. Ruiqing, Q. Lele, W. Xin, Z. Lingyun, Z. Xuesong, H. Jianglong, Journal of Solid State Chemistry, 198 (2013) 459 - 465.

[29]. R. El-Mallawany, A. Patra, C.S. Friend, R. Kapoor, P.N. Prasad, Optical Materials, 26 (2004) 267 - 270.

[30]. K. Yanagisawa, J. Ovenstone, Journal of Physical Chemistry, 103 (1999) 7781 - 7787.

[31]. A. Patra, C.S. Friend, R. Kapoor, P.N. Prasad, Chemistry of Materials, 15 (2003) 3650 - 3655.

[32]. R.S. Quimby, W.J. Miniscalco, B. Thompson, Journal of Applied Physics, 76 (1994) 4472 - 4478.

[33]. J. Zhang, W. Qin, D. Zhao, D. Degejihu, J. Zhang, Y. Wang, C. Cao, Journal of luminescence, 122 (2007) 506 - 508.

7. Up-conversion luminescence and nano-composites features of Al_2O_3-TiO_2: Yb^{3+}, RE (RE = Er^{3+} and Tm^{3+}) powders

7.1 Introduction

Currently, rare-earths (RE) activated optical materials with efficient up-conversion luminescence from infrared to visible radiation have attracted much interest for their possible applications in photonics, frequency up-converters, biological fluorescence labels, undersea optical communications, solar cells and temperature sensors [1,2]. This up-conversion process depends on sequential absorption of two or more photons and energy transfer between doping ions [3]. In Yb^{3+}/Er^{3+} codoped oxides, Yb^{3+} is considered an excellent sensitizer with two manifolds ground and excited states, respectively corresponding to $^2F_{7/2}$ and $^2F_{5/2}$ with spacing of 980 nm apart. Usually, Yb^{3+} is excited with near-infrared (NIR) laser and energy transfer to an activator resulting in improvement of visible or NIR emission like in the case of erbium (Er^{3+}) where green, red and NIR have been shown to improve [4]. Er^{3+} ion displays up-conversion luminescence with maxima at 410, 550, 660, 810 and 980 nm corresponding to the transitions from the excited $^2H_{9/2}$, $^4S_{3/2}$, $^4F_{9/2,}$ $^4I_{9/2}$ and $^4I_{11/2}$ states to the ground $^4I_{15/2}$ state [5]. The up-conversion luminescence from Yb^{3+}/Er^{3+} codoped oxides can be utilized in amorphous silicon (a-Si) and crystalline silicon (c-Si) solar cells, dye-sensitized solar cells (DSSCs) and organic solar cells [6]. Thulium (Tm^{3+}) is one of the most studied activator for blue ($^1G_4 \rightarrow {}^3H_6$), red ($^1G_4 \rightarrow {}^3F_4$ and $^3F_3 \rightarrow {}^3H_6$) and NIR ($^3H_4 \rightarrow {}^3H_6$) emission based on up-conversion. In addition, up-conversion phosphors in a low phonon host material can generate a high up-conversion luminescence. The alternative way of enhancing the luminescence efficiency of Tm^{3+} ion is by co-doping with Yb^{3+} sensitizer [7,8]. The Yb^{3+}/Tm^{3+} codoped in oxides are more useful in biomedical imaging applications because it displays the most intense emission in NIR region. This emission is very important for the deep tissue imaging of up-conversion fluorescent labels [9].

Alumina-titania (Al_2O_3-TiO_2) is one of the most useful nano-composites to host rare-earth ions to prepare up-conversion phosphor materials. These nano-composites have shown great interest in physical properties protected metallic structural components against wear and corrosion because of their excellent thermal, chemical and mechanical stability. In addition, the nano-composites can be used in different applications including catalysis, photocatalytic, solar cells and self-cleaning. Alumina (Al_2O_3) is a ceramic material with high level of strength, good toughness and tribological properties. Titania (TiO_2) is a wide bandgap semiconductor material that is used in different application including photocatalytic activities, solar cells, hydrogen storage and sensors [10]. There are various methods that have been used to prepare nanostructured composites such as sol-gel synthesis, hydrothermal synthesis, and chemical vapour deposition, spin coating method and microwave-combustion synthesis [11]. Sol-gel synthesis shows important advantages over other synthesis techniques, due to a low cost simple synthetic route, good compositional control and low crystallization temperature [12].

During this present study, we made an attempt to prepare nano-composites of Al_2O_3-TiO_2 with a molar ratio of 1:1 by sol-gel method using titanium (IV) butoxide and aluminium n-butoxide as a titanium and aluminium source, respectively. The Yb^{3+}/Er^{3+} and Yb^{3+}/Tm^{3+} codoped samples in Al_2O_3-TiO_2 were synthesized. The effects of nano-composite features on crystalline phase, surface morphology, optical properties and up-conversion photoluminescence for Er^{3+} and Tm^{3+} contents of Al_2O_3-TiO_2Yb^{3+},Er^{3+}/Tm^{3+} phosphor powders excited at 980 nm were investigated and the possible up-conversion mechanism is also discussed.

7.2 Experimental procedure

7.2.1 Al_2O_3-TiO_2 preparation

Figure 7.1 depicts schematic diagram of the synthesis procedure of Al_2O_3-TiO_2: Yb^{3+}, Er^{3+}/Tm^{3+} nano-composites powders. Titanium (IV) butoxide, ytterbium (III) acetate tetrahydrate, erbium (III) acetate hydrate, thulium (III) acetate hydrate, aluminium n-butoxide, ethanol and acetic acid were used as precursors to prepare Al_2O_3-TiO_2: Yb^{3+}, Er^{3+}/Tm^{3+} nano-composites powders. Al_2O_3 solution was prepared by dissolving 2.0 g aluminium n-butoxide in a mixture of 20 ml ethanol and acetic acid and was stirred vigorously for 5 min at ~ 50 ^{o}C. The reaction was stopped after stirring for further 60 min and the milky solution was obtained. The solution was aged for 25 min. TiO_2 solution was prepared by dissolving 4 ml titanium (IV) butoxide into a mixture of 20 ml ethanol and acetic acid that has been stirred vigorously for 5 min. The reaction was stopped after stirring for 60 min and the milky solution was obtained. The solution was aged for 25 min. These solutions were mixed using magnetic stirrer for 60 min. The milky solution was aged for 24 hours and it was transformed to a gel during the storage. The gel was dried in an oven maintained at 100 ^{o}C for 2 hours to ensure that all organic solvents have evaporated, and then a powder was annealed at 950 ^{o}C for 2 hrs in air. The resulting powders were ground using pestle and mortar. Al_2O_3-TiO_2: Yb^{3+}, Er^{3+}/Tm^{3+} nano-composites powders were prepared too with a fixed concentration of Yb^{3+} (1 mol %), while Er^{3+} was varied from 0.1 to 0.5 mol %, and Tm^{3+} was varied from 0.1 to 0.4 mol %.

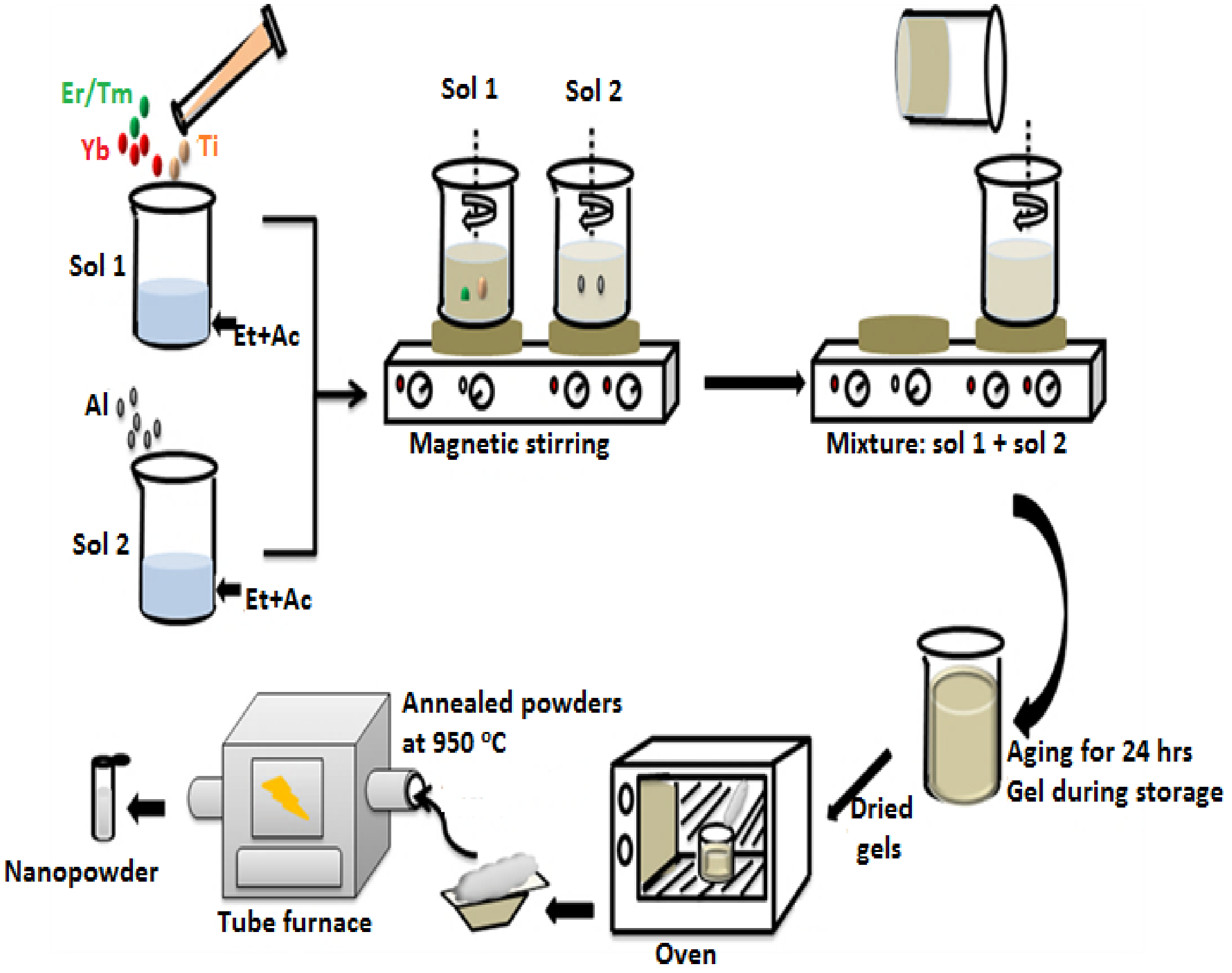

Figure 7.1: Schematic diagram of the synthesis procedure of Al_2O_3-TiO_2: Yb^{3+}, Er^{3+}/Tm^{3+} nano-composites powders (Ti = titanium (IV) butoxide, Yb = ytterbium (III) acetate tetrahydrate, Er = erbium (III) acetate hydrate, Tm = thulium (III) acetate hydrate, Al = aluminium n-butoxide, Et = ethanol and Ac = acetic acid).

7.2.2. Characterization

The crystal structure of the nano-composite was analyzed using a Bruker D8 Advanced powder X-ray diffractometer (XRD) with CuK_{α} radiation wavelength of 0.154 nm. The particle morphology and chemical composition of the nano-composites were carried out using JEOL JSM-7800 field emission scanning electron microscope (FE-SEM) coupled with energy dispersive x-ray spectroscopy (EDS). The diffuse reflectance measurements were performed using Lambda 950 spectrophotometer. The study of vibrational bonds of nano-composites was carried out by Fourier transform infrared (FTIR). Up-conversion measurements of nano-composites were performed by using fiber-coupled 980 nm NIR laser as the excitation source, redtipe ocean optics spectrometer consists of mirrors, diffraction grating, an array of charge-coupled device (CCD) detector and optical fibres relayed to the computer for spectrum recording.

7.3 Results and discussion

7.3.1 XRD analysis

Figure 7.2 presents XRD patterns of nano-composites Al_2O_3-TiO_2: Yb^{3+}, Er^{3+}/Tm^{3+} powders. The diffraction patterns exhibited mixed oxides of α-Al_2O_3 and rutile phase of TiO_2 which were indexed with JCPDS No. 46-1212 and JCPDS No. 21-1272, respectively. The peaks marked with "α" and "R" corresponded to α-Al_2O_3 and rutile (TiO_2) phases, respectively. In addition, the peak marked with asterisks (*) indicates impurity from cubic phase ytterbium titanium oxide ($Yb_2Ti_2O_7$) referenced with JCPDS No. 17-0454. The diffraction patterns of nano-composites depict the predominant existence of the rutile phase of titania, while small peaks indicate α-phase of alumina. However, the volume or molar ratio of nano-composites was 1:1. These results indicate that the small peaks of alumina were due to the early stage of crystallization because usually α-phase of alumina is thermodynamically stable at 1200 ^{o}C [13]. The average crystallite size D was estimated from the Debye-Scherrer equation:

$$D = \frac{0.9\lambda}{\beta cos\theta} \tag{7.1}$$

where λ is the x-ray wavelength and β is the full-width half at maximum (FWHM) of the x-ray peak at the Bragg angle θ. The average crystallite size D of undoped Al_2O_3-TiO_2 phosphor was 38 nm, while Yb^{3+}/Er^{3+} and Yb^{3+}/Tm^{3+} codoped samples were estimated to be 36 nm and 38 nm, respectively. Figure 7.3 shows analysis of (012) and (110) planes for "α" and "R" of alumina and titania, respectively. In Yb^{3+}/Er^{3+} codoped sample, peaks were shifted to the low Bragg angles due to the micro-strains caused by incorporation of Yb^{3+} and Er^{3+} ions [14,15].

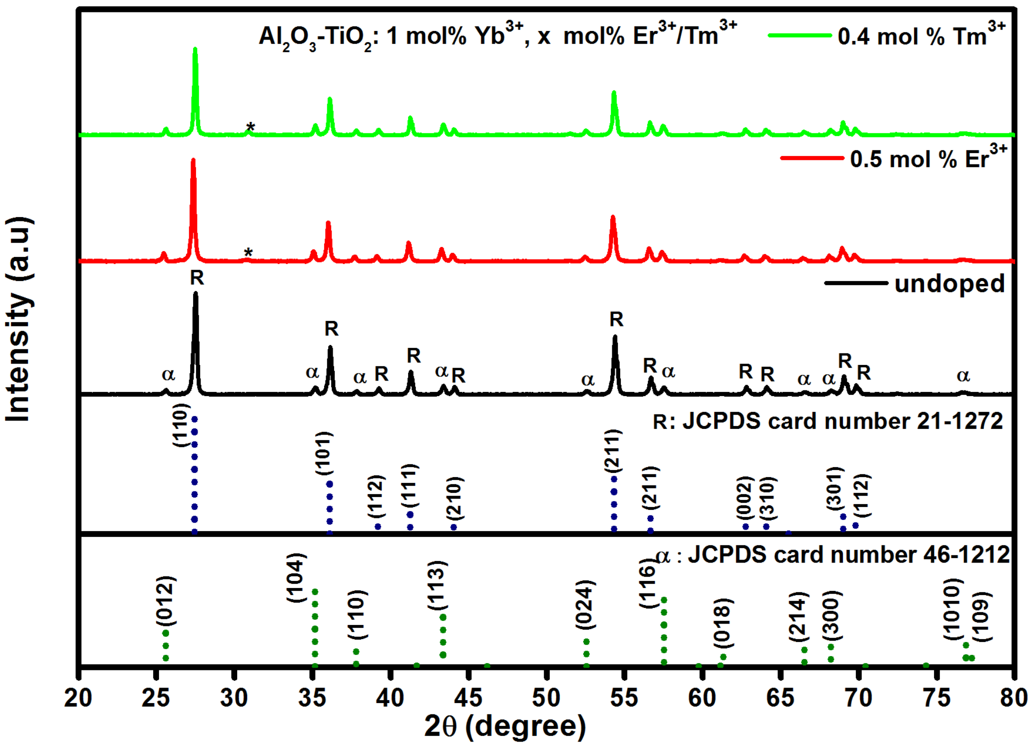

Figure 7.2: XRD patterns of nano-composites Al_2O_3-TiO_2: Yb^{3+}, Er^{3+}/Tm^{3+} powders.

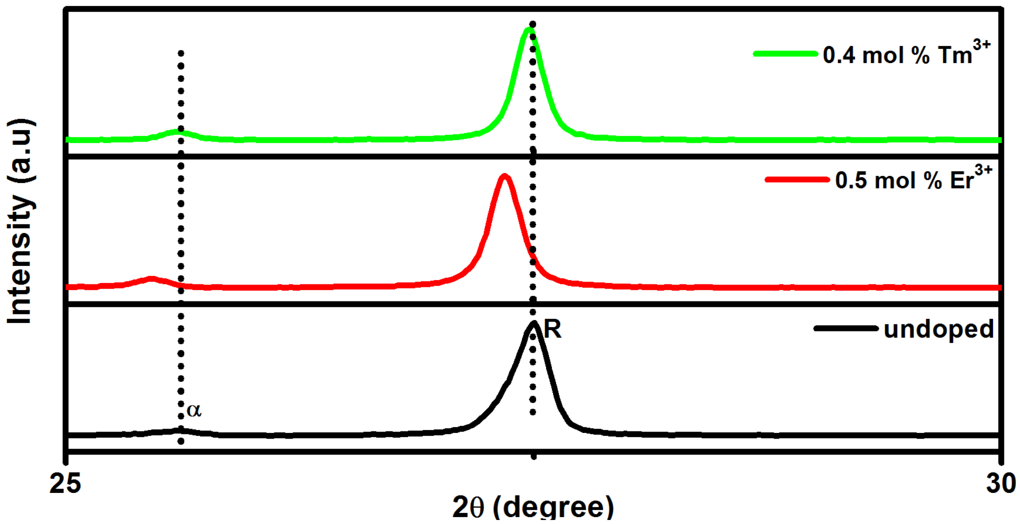

Figure 7.3: Analysis of (012) and (110) planes of alpha and rutile phases of alumina and titania.

7.3.2 FE-SEM observations

The FE-SEM micrographs of undoped Al_2O_3-TiO_2 (a), (b), codoped Al_2O_3-TiO_2: Yb^{3+}, Er^{3+} (c), (d) and Al_2O_3-TiO_2: Yb^{3+}, Tm^{3+} (e), (f) phosphor powders are shown in figure 7.4. Figure 7.4 (b) is a high magnification micrograph of the chosen area in figure 7.4 (a) while figure 7.4 (d) and

(f) respectively depict the high magnification of the selected areas in figure 7.4 (c) and (e) micrographs. The low magnification micrographs (Fig 7.4(a), (c) and (e)) show agglomerated network of nano-rods, while the high magnification micrographs (Fig 7.4(b), (d) and (f)) indicate that these particles were nano-rods self-assembled by agglomerated spherical particles. The nano-rods were attributed to titania while alumina was associated with spherical particles [13]. Figure 7.4 (c), (d), (e) and (f) exhibit that the samples retain the morphology of nano-rods with spherical particles after co-doping with Yb^{3+}, Er^{3+} and Yb^{3+}, Tm^{3+} .

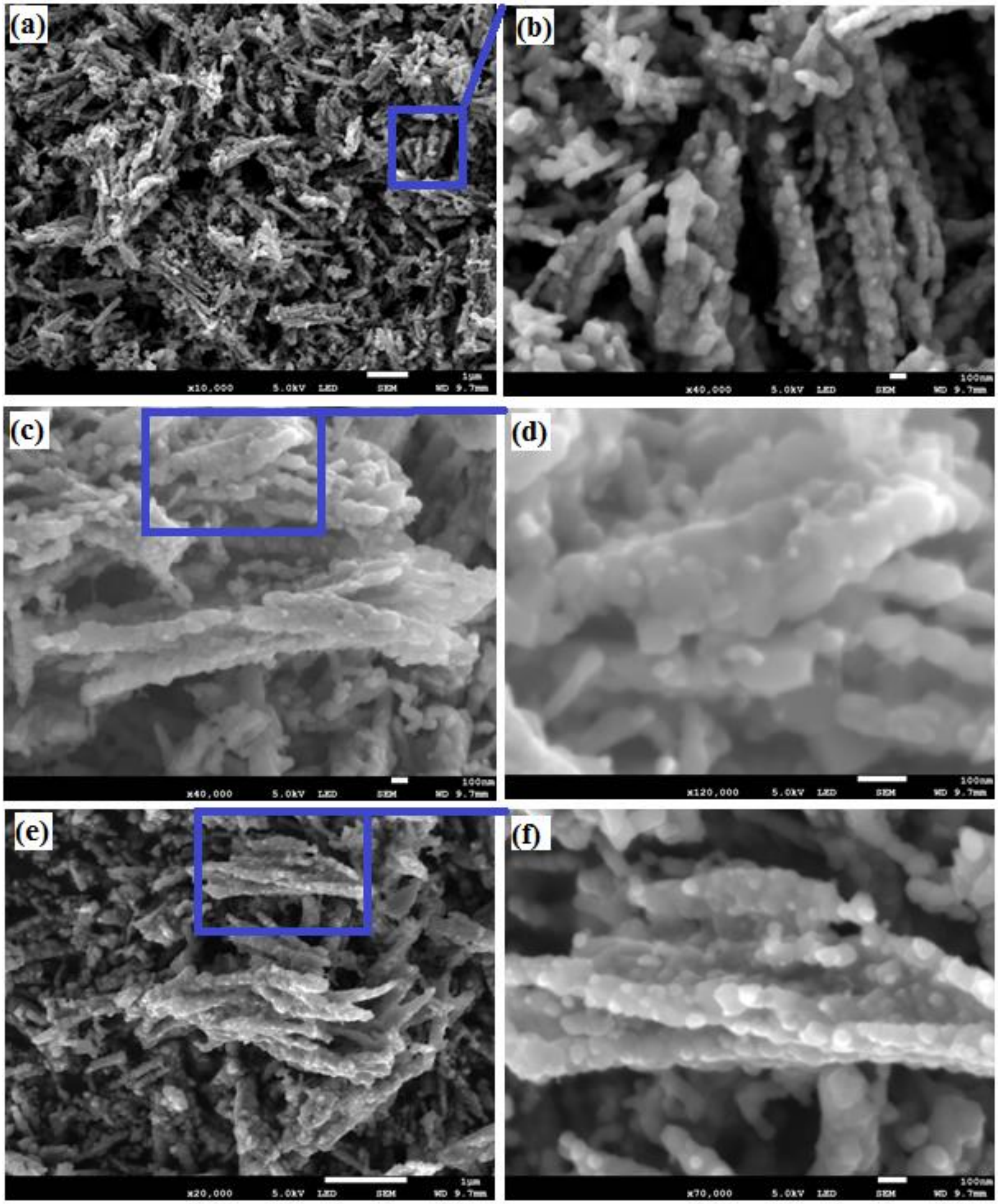

Figure 7.4: FE-SEM micrographs Al_2O_3-TiO_2 (a), (b), Al_2O_3-TiO_2:Yb^{3+},Er^{3+} (c), (d) and Al_2O_3-TiO_2:Yb^{3+},Tm^{3+} (e), (f) phosphor powders.

EDS spectra of undoped Al_2O_3-TiO_2 (a), Al_2O_3-TiO_2: Yb^{3+}, Er^{3+} (b) and Al_2O_3-TiO_2: Yb^{3+}, Tm^{3+} phosphor powders are shown in figure 7.5. The inset in the top middle demonstrates the FE-SEM micrograph and the area where EDS analysis was performed, while the one on the top right corner depicts the weight % of the elements at the selected area. All the main elements were detected. The existence of carbon (C) peak in all EDS spectrums was due to the carbon tape on which phosphor powders were mounted [16]. In undoped (Fig 7.5(a)) the elemental composition of Ti, O and Al in weight % were estimated to be 40.63, 63.10 and 15.63 % respectively, while in codoped Yb^{3+},Er^{3+} sample (Fig 7.5(b)) Ti, O and Al were 39.06, 43.75 and 14.06 %, respectively. In Yb^{3+},Tm^{3+} codoped (Fig 7.5(c)) the weight % of Ti, O and Al were estimated to be 35.94, 45.31 and 14.06 % , respectively. Figure 7.5(a) demonstrates the atomic content ratio Ti/O and Al/O of 21.92/63.10 and 14.97/63.10 to be 0.35 and 0.24, while in codoped samples (Fig 7.5(b)) atomic content ratios Ti/O and Al/O of 20.03/67.17 and 12.80/67.17 to be 0.30 and 0.19 and (Fig 7.5(c)) atomic content ratios Ti/O and Al/O of 18.29/69.01 and 12.70/69.01 to be 0.27 and 0.19, respectively. These results verify the formation of titania particles to a large extent than alumina. In codoped samples (Fig. 7.5 (b) and Fig 7.5 (c)) atomic content ratio of Ti/O decreases which means the dopants (Yb^{3+}, Er^{3+} and Tm^{3+}) substitutes Ti^{4+} ions in a host [17]. Table 7.1 depicts quantitative EDS microanalysis of weight (W) and atomic (A) content percentages (%) of Al_2O_3-TiO_2:Yb^{3+}, Er^{3+}/Tm^{3+} phosphor powders.

Table 7.1: Quantitative EDS microanalysis of Al_2O_3-TiO_2: Yb^{3+}, Er^{3+}/Tm^{3+} phosphor powders (W % -weight percentage and A % - atomic content percentage).

Elements	**Undoped**		**Yb^{3+}-Er^{3+}**		**Yb^{3+}-Tm^{3+}**	
	W %	**A %**	**W %**	**A %**	**W %**	**A %**
Ti	40.63	21.92	39.06	20.03	35.94	18.29
Al	15.63	14.97	14.06	12.80	14.06	12.70
O	39.06	63.10	43.75	67.17	45.31	69.01

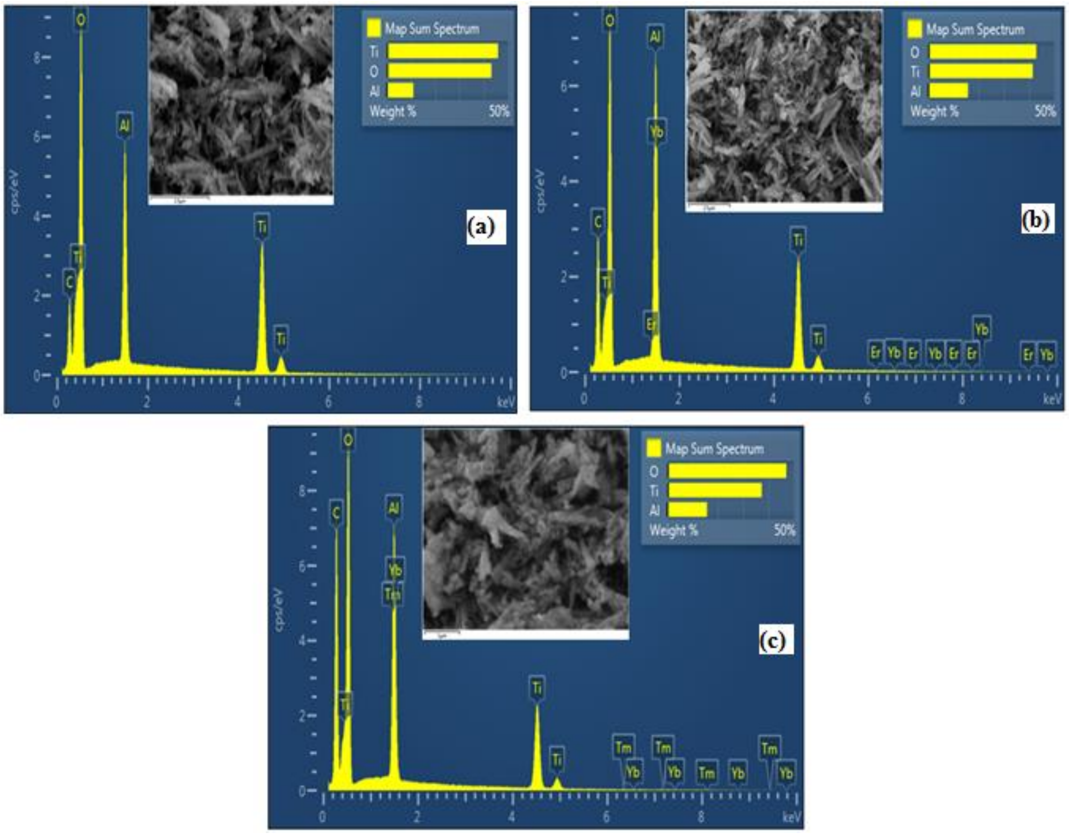

Figure 7.5: EDS spectra of (a) Al_2O_3-TiO_2, and codoped (b)Yb^{3+}, Er^{3+} and (c) Yb^{3+}, Tm^{3+} phosphor powders.

7.3.3 UV-vis analysis

The diffuse reflectance spectra (DRS) was used to measure the absorption properties of Al_2O_3-TiO_2 nano-composite and the effects of Yb^{3+}, Tm^{3+} and Er^{3+} in figure 7.6. The results indicate the strong UV absorption below 380 nm which is due to wide band gap of 3.2 eV and 3.0 eV for anatase and rutile phases of titania, respectively [18]. The inset demonstrates absorption bands of Er^{3+} and Tm^{3+} in visible and NIR spectral region. Four absorption bands centered at 490, 524, 655 and 798 nm were assigned to the transitions from ground $^4I_{15/2}$ state to excited $^4F_{7/2}$, $^2H_{11/2}$, $^4F_{9/2}$ and $^4I_{9/2}$ states of Er^{3+} ion, respectively [19,20]. Two absorption bands centered at 682 and 792 nm were assigned to the transitions from ground $^3H_6$ state to excited $^3F_3$ and $^3H_4$ states of Tm^{3+} ion, respectively [21,22].

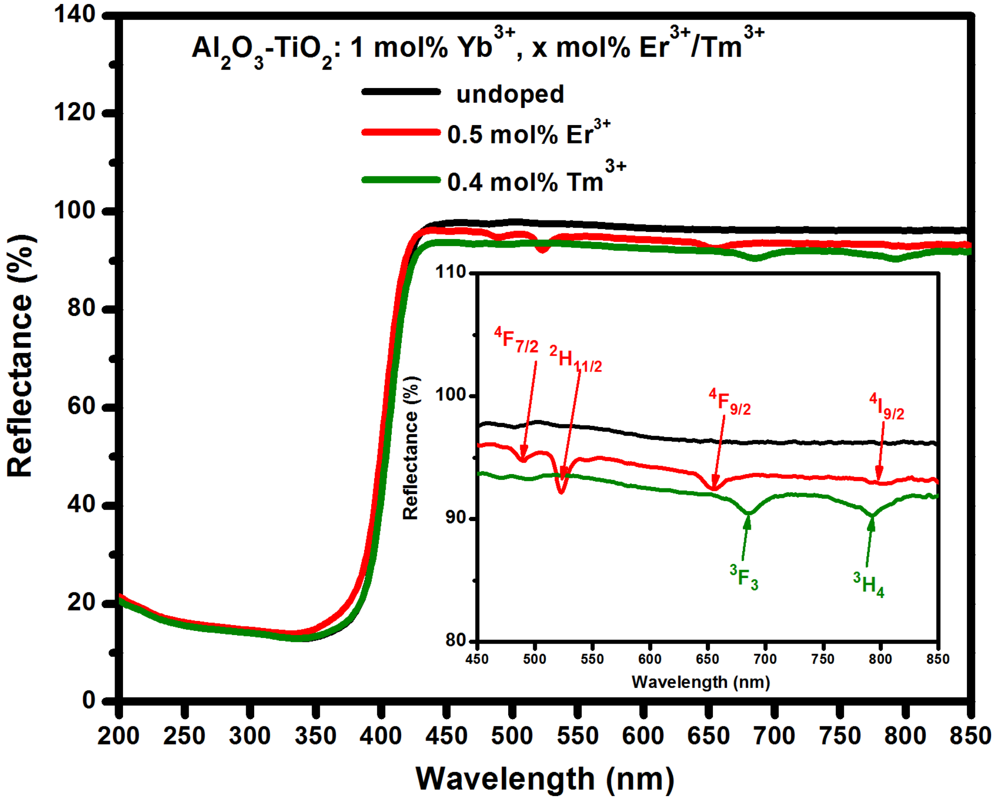

Figure 7.6: DRS of Al_2O_3-TiO_2: Yb^{3+}, Er^{3+} /Tm^{3+} phosphor powder.

The optical indirect bandgap was estimated by Tauc plot of $(\alpha h\nu)^n$ against photon energy ($h\nu$), with $n = ½$ which is correct for allowed indirect transition in material such as Al_2O_3-TiO_2 (shown in figure 7.7) [23]. However, alumina and titania are respectively direct and indirect bandgap materials. XRD and EDS proved that the titania is more dominant than alumina in a nano-composite. The energy bandgap of the host Al_2O_3-TiO_2 was 2.98 eV while Yb^{3+},Er^{3+} and Yb^{3+},Tm^{3+} codoped samples were 3.00 and 2.98 eV, respectively. The increase in energy bandgap Yb^{3+}-Er^{3+} codoped sample was noticed due to the upshift of Fermi level that is located deep inside the conduction band caused by excess of electrons from Er^{3+} and Yb^{3+} [24,25].

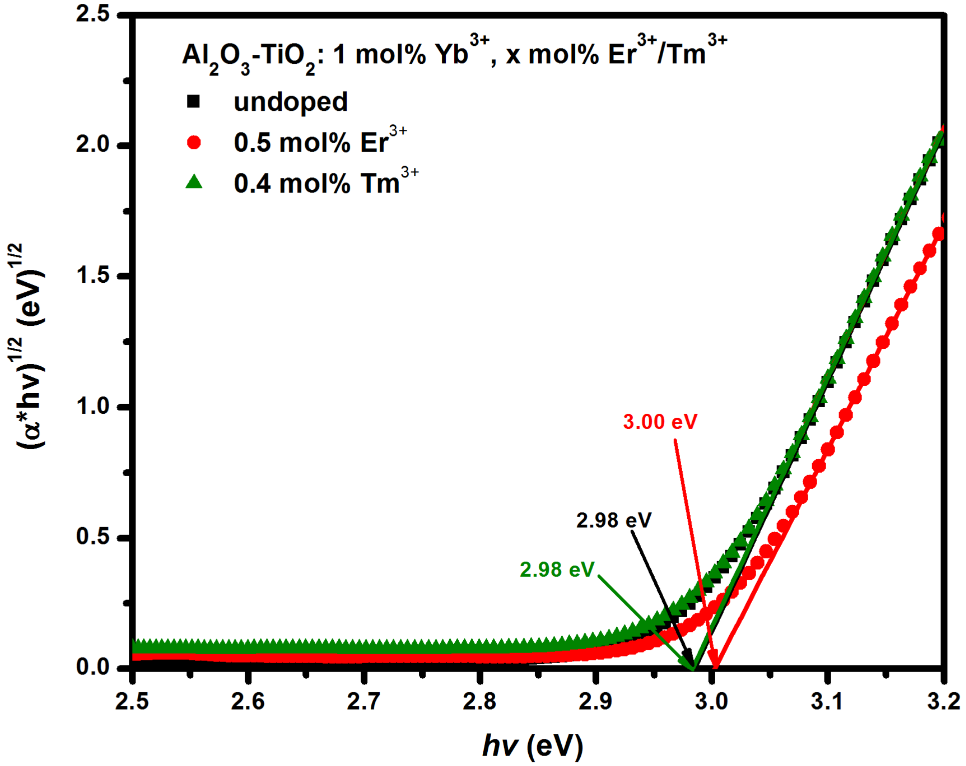

Figure 7.7: Determination of energy bandgap of Al_2O_3-TiO_2: Yb^{3+}, Er^{3+}/Tm^{3+} phosphor powders by Tauc plot.

7.3.4 FTIR analysis

Figure 7.8 presents FTIR spectra of Al_2O_3-TiO_2: Yb^{3+}, Er^{3+}/Tm^{3+} phosphor powder. The broad absorption band from 647 – 1154 cm^{-1} with resolved bands centered at 906 cm^{-1} and 1122 cm^{-1}. These bands were assigned to the Ti-O-Ti bonds of titania and asymmetric bending modes of Al-O-Al bonds, respectively [26]. This indicates that alumina and titania did not mix at the particle level to form a new compound, and they rather formed clusters of like materials. The absorption band centered at 1631 cm^{-1} is due to the OH vibration of hydroxyl group and surface adsorbed water [27]. In Yb^{3+}-Er^{3+} codoped samples, the absorption band centered at 2253 cm^{-1} was assigned to the atmospheric CO_2 [28].

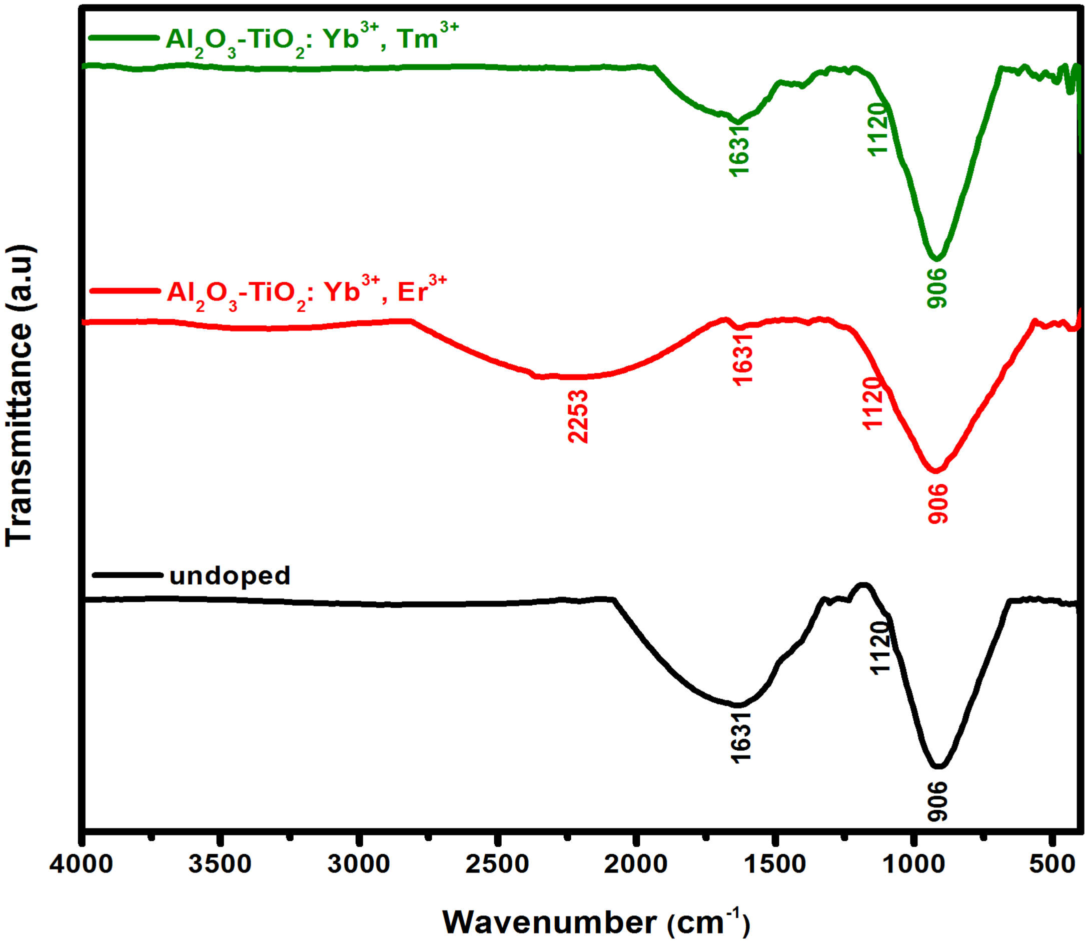

Figure 7.8: FTIR spectra of Al_2O_3-TiO_2: Yb^{3+}, Er^{3+}/Tm^{3+} phosphor powder.

7.3.5 Up-conversion properties

The up-conversion emission from Al_2O_3-TiO_2:Yb^{3+}/Er^{3+} phosphor powder excited with 980 nm laser operating at 2078 mW was measured and the spectra are shown in figure 7.9. The inset in the top right shows up-conversion spectrum of undoped sample excited with 980 nm, while the one on the bottom right indicates the Commission Internationale de I'Eclairage (CIE) chromaticity diagram. There were three main emission bands with maxima at 523, 548 and 658 nm corresponding to $^2H_{11/2}\rightarrow{}^4I_{15/2}$, $^4S_{3/2}\rightarrow{}^4I_{15/2}$ and $^4F_{9/2}\rightarrow{}^4I_{15/2}$ transitions of Er^{3+} ion, respectively [29,30]. The low concentration of 0.5 mol% Er^{3+} is uniformly distributed in a host lattice and therefore it shows the most intense red up-conversion emission. This indicates that in a high concentration the inter-ionic distance of Er^{3+}-Er^{3+} ions is small and this results in the formation of Er^{3+} cluster. Thus, concentration quenching process is mostly to occurs which causes the non-radiative relaxation processes [31,32]. In order to observe the colour of the visible light from the nano-composites phosphor powders, the colour coordinates were calculated at different concentrations of Er^{3+} as shown in the CIE chromaticity diagram. The nano-composites phosphor powder displays yellowish-green colour due to a combination of green and red visible colours [33].

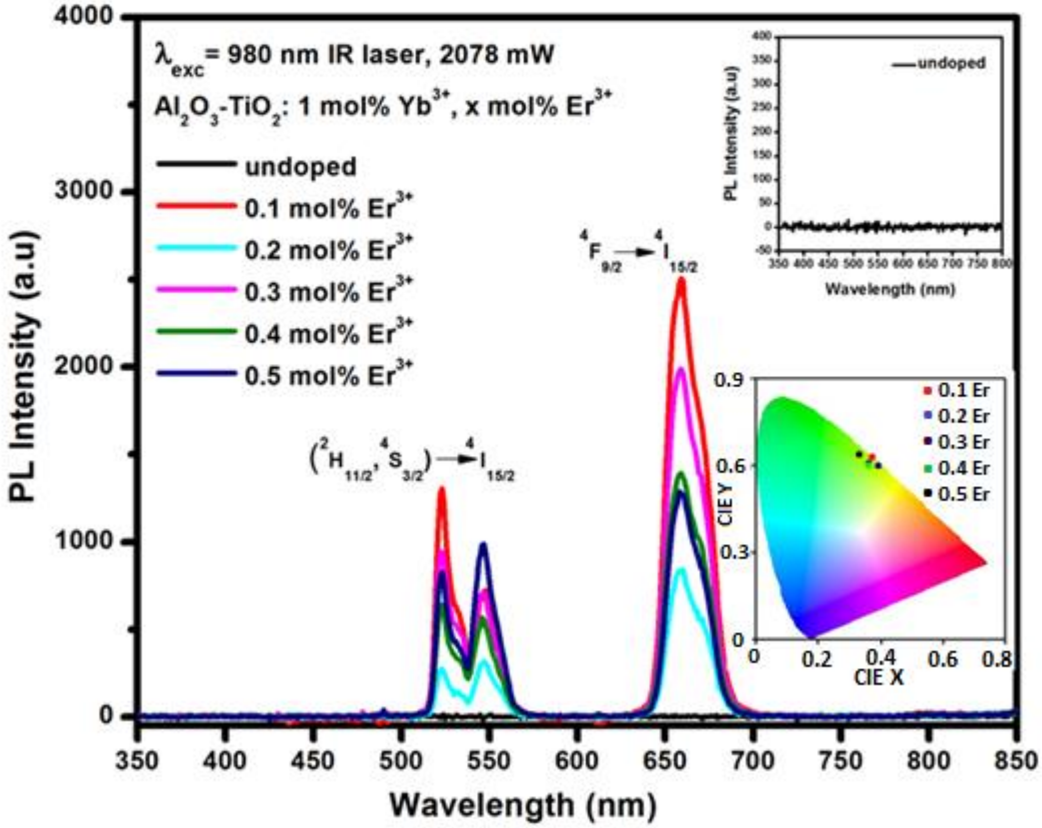

Figure 7.9: Up-conversion spectrum of nano-composites Al_2O_3-TiO_2: Yb^{3+}, Er^{3+} powders by excitation of 980 nm.

Figure 7.10 presents the up-conversion emission spectra of Al_2O_3-TiO_2: Yb^{3+},Tm^{3+} nano-composites phosphor powders excited with a 980 nm laser diode operating at 2078 mW. There were four main emission bands with maxima at 480, 650, 693 and 800 nm assigned to $^1G_4\rightarrow{}^3H_6$, $^1G_4\rightarrow{}^3F_4$, $^3F_3\rightarrow{}^3H_6$ and $^3H_4\rightarrow{}^3H_6$ transitions of Tm^{3+} ion. The most intense near-infrared emission was observed in low concentration of Tm^{3+} (0.1 mol%), while quenching was noticed in a highest concentration of Tm^{3+} (0.4 mol%). This suggest that Tm^{3+}-Tm^{3+} ions were clustered in a high concentration, while in low concentration it means Tm^{3+} ions were distributed well in a host. The inset shows magnified red emissions with maxima at 650 and 693 nm corresponding to $^1G_4 \rightarrow ^3F_4$ and $^3F_3 \rightarrow ^3H_6$ transition of Tm^{3+} ion [34].

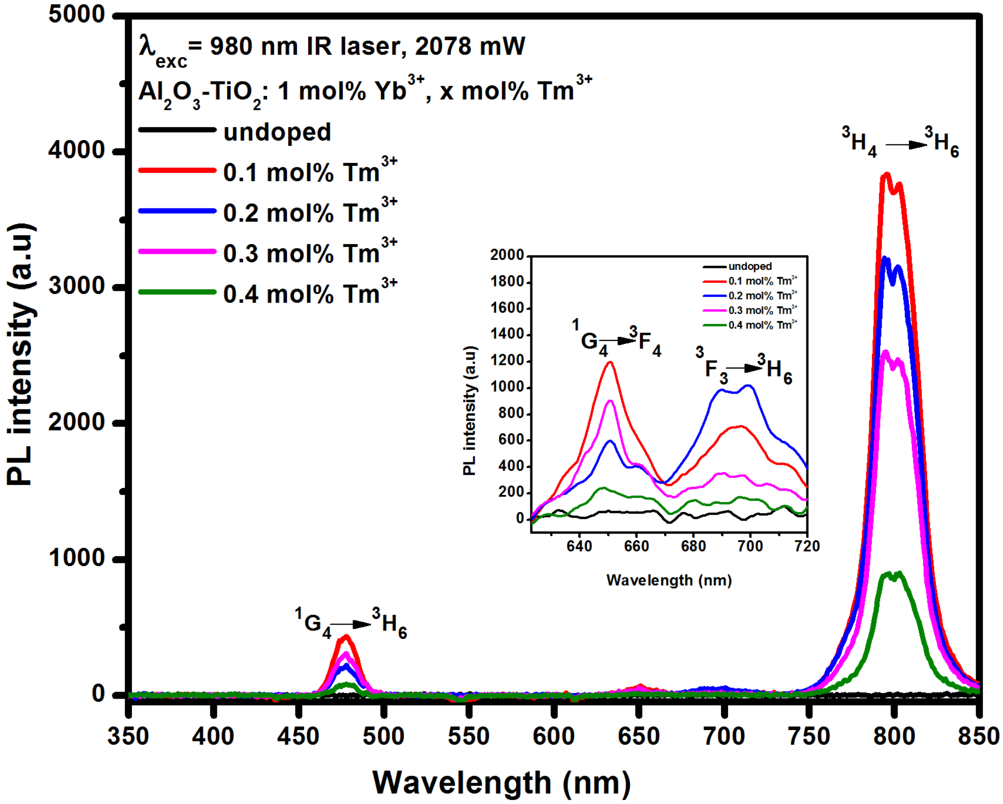

Figure 7.10: Up-conversion spectrum of nano-composites Al_2O_3-TiO_2: Yb^{3+},Tm^{3+} powders by excitation of 980 nm.

7.3.6 Up-conversion mechanism

Figure 7.11 shows an energy transfer mechanisms of up-conversion process in Al_2O_3-TiO_2: Yb^{3+}, Er^{3+}/Tm^{3+} nano-composites phosphor powders upon excitation with 980 nm laser. The excited-state absorption (ESA) and energy transfer up-conversion (ETU) are known as the dominant up-conversion mechanisms. The ETU mechanism involves sensitizer Yb^{3+} ion and activator (Er^{3+} or Tm^{3+}) ion. For Yb^{3+}/Er^{3+} samples, Yb^{3+} ions at the ground state were excited to the $^2F_{5/2}$ state by absorbing 980 nm NIR photon through ground state absorption (GSA), and energy transferred from Yb^{3+} to Er^{3+} ions to populate $^4I_{11/2}$, $^4F_{9/2}$ and $^4F_{7/2}$ intermediate states of Er^{3+}. The non-radiative relaxation occurred from $^4F_{7/2}$ to $^2H_{11/2}$, $^4S_{3/2}$ and $^4F_{9/2}$ states, while radiative relaxation for green and red emission corresponding to ($^4S_{3/2}$, $^2H_{11/2}$) $\rightarrow ^4I_{15/2}$ and $^4F_{9/2} \rightarrow ^4I_{15/2}$ transitions of Er^{3+} were seen. In addition, another alternative mechanism in Yb^{3+} ion, a non-radiative decay at $^2F_{5/2} \rightarrow ^2F_{7/2}$ will occur and energy transferred to populate $^4I_{11/2}$ intermediate states in Er^{3+}.

Therefore, Er^{3+} is excited to the $^4F_{7/2}$ state via the following channels: $^4I_{11/2} \rightarrow$ $^4F_{7/2}$ and $^4I_{13/2} \rightarrow {}^4F_{9/2}$. Eventually, the non-radiative and radiative relaxation of green and red emission will be observed [35,36]. In Yb^{3+}/Tm^{3+}-codoped samples, usually Yb^{3+} is used as a sensitizer to improve the efficiency of up-conversion because of its large absorption cross-section, while Tm^{3+} ions is considered as an activator to give the emission upon NIR excitation. Once the Yb^{3+} sensitizing ions are populated through GSA upon 980 nm NIR laser excitation, the successive three-step energy transfers from Yb^{3+} to Tm^{3+} will populate $^3H_5$, $^3F_2$ and $^1G_4$ intermediate states of Tm^{3+}. The non-radiative relaxations of $^3H_5 \rightarrow {}^3F_4$ and $^3F_2 \rightarrow {}^3H_4$ transition of Tm^{3+} ions were observed. The radiative relaxation for blue ($^1G_4 \rightarrow {}^3H_6$), red ($^1G_4 \rightarrow {}^3F_4$ and $^3F_3 \rightarrow {}^3H_6$) and NIR ($^3H_4 \rightarrow {}^3H_6$) were observed [37].

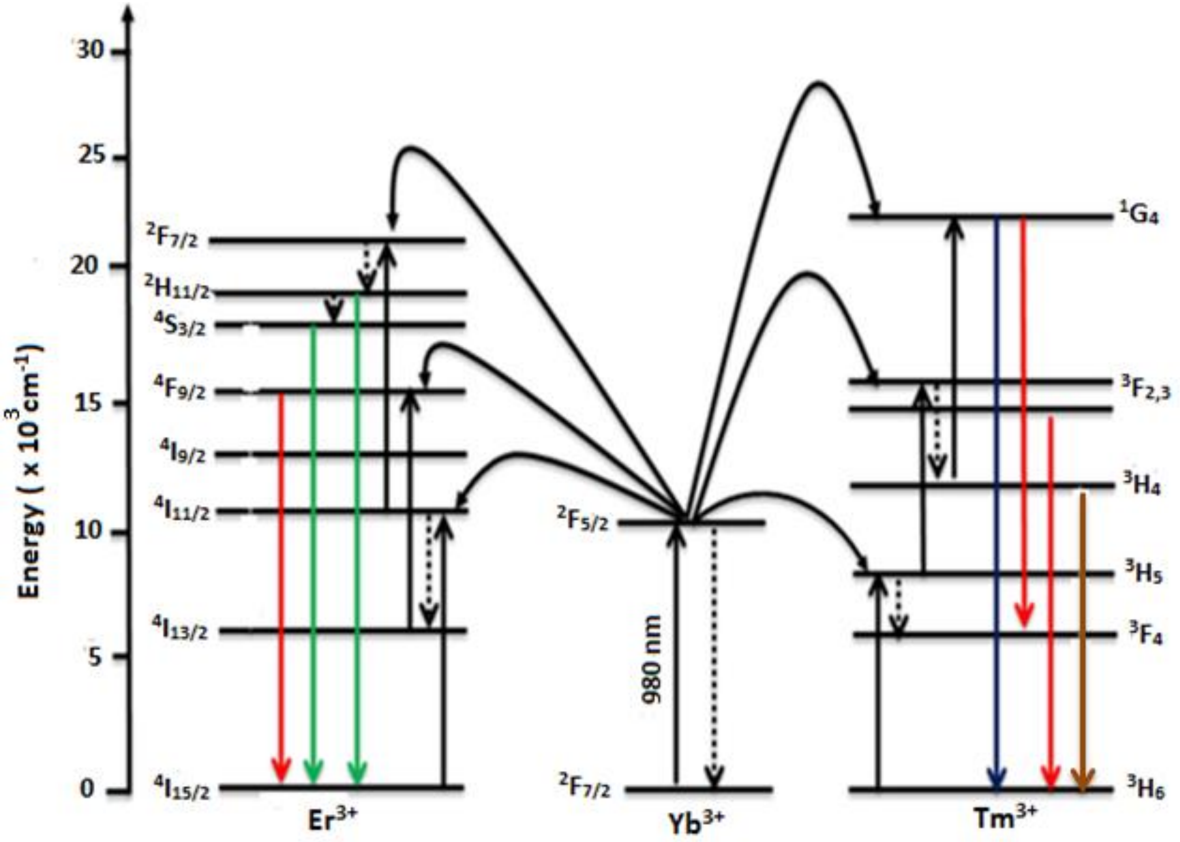

Figure 7.11: Energy transfer mechanisms showing the up-conversion process in Al_2O_3-TiO_2: Yb^{3+}, Er^{3+}/Tm^{3+} phosphor powder under excitation of 980 nm. (The full arrows pointed up and down represent photon excitation and emission, respectively. Square dotted lines and curly full arrows represent non-radiatively relaxation and energy transfer, respectively).

7.4 Conclusion

The nano-composites of Al_2O_3-TiO_2:Yb^{3+},Er^{3+}/Tm^{3+} phosphor powders were successfully synthesized by sol-gel method. XRD confirms the mixed oxides of titania rutile phase and an early crystallization of α-Al_2O_3 phase with crystallite size of ~ 38 nm in diameter. FE-SEM suggests nano-rods morphology self-assembled with spherical particles. UV-vis confirms strong band-to-band absorption at 380 nm and Tauc plot exhibit indirect optical bandgap of ~ 3.0 eV. FTIR demonstrates the characteristics absorption peaks of Ti-O-Ti and Al-O-Al bonds which indicate the incorporation of alumina into titania. The Yb^{3+}/Er^{3+} codoped phosphors exhibits the most intense red up-conversion emission with CIE coordinates showing a phosphor with yellowish-green visible colour, while Yb^{3+}/Tm^{3+} codoped samples display the most intense NIR up-conversion luminescence. The possible mechanism showing ESA and ETU between Yb^{3+}/Er^{3+} and Yb^{3+}/Tm^{3+} was illustrated and discussed. The up-conversion results suggest that by co-doping Yb^{3+} along with Er^{3+} improved red emission, while in Tm^{3+} it enhanced a NIR emission. The nano-composites did not mix well in the particle level to form a new compound but they have formed clusters of like materials whereby titania is more dominant than alumina.

7.5 References

[1]. Z. Zhang, J. Zhang, W. Zhou, M. Song, W. Li, Q. Hu, X. Zhao, Advanced Materials Research, 66 (2009) 167 - 170.

[2]. Y. Qu, X. Kong, Y. Sun, Q. Zeng, H. Zhang, Journal of Alloys and Compounds, 485 (2009) 493 - 496.

[3]. G. Mialon, S. Turkcan, G. Dantelle, D.P. Collins, M.Hadjipanayi, R.A. Taylor, T. Gacoin, A. Alexandrou, J.-P. Boilot, Journal of Physical Chemistry C, 114 (2010) 22449 - 22454.

[4]. F. Wang, D. Banerjee, Y. Liu, X. Chen, X. Liu, Analyst, 135 (2010) 1839 - 1854.

[5]. N. Dyck, G. Demopoulos, Spectral Engineering of Dye Sensitized Solar Cells Through Intergration $NaYF_4:Yb^{3+},Er^{3+}$ Up-conversion Nano-materials, M.Eng (Thesis), (2013), McGrill University, Montreal QC, Canada.

[6] P. Ramasamy, P. Manivasakan, J. Kim, Royal Society Chemistry advances, 4 (2014) 34873 - 34895.

[7]. H.K. Yang, J.H. Oh, B.K. Moon, J.H. Jeong, S.S. Yi, Ceramics International, 40 (2014) 13357 - 13361.

[8]. B. Ma, X. Liu, L. Liu, Y. Meng, B. Li, X. Zhao, P. Pu, X. Wang, Royal Society of Chemistry Advances, 4 (2014) 63100 - 63104.

[9]. J. Chang, Y. Liu, J. Li, S. Wu, W. Niu, S. Zhang, Journal of Materials Chemistry C, 1 (2013) 1168 - 1173.

[10]. U.O.A. Arier, F.Z. Tepehan, Journal of Alloys and Compounds, 509 (2011) 8262 - 8267.

[11]. S.A.E. All, G.A.E. –Shobaky, Journal of Alloys and Compounds, 479 (2009) 91 - 96.

[12]. M.R. Mohammadi, Materials Science in Semiconductor Processing, 27 (2014) 711 - 718.

[13]. M.A. Ahmed, M.F. Abdel-Messih, Journal of Alloys and Compounds, 509 (2011) 2154 - 2159.

[14]. D.Y. Lee, J.T. Kim, J.H. Park, Y.H. Kim, I.K. Lee, M.H. Lee, B.Y. Kim, Current Applied Physics, 13 (2013) 1301 - 1305.

[15]. E. Pakizeh, M. Moradi, A. Ahmadi, Journal of Physics and Chemistry of Solids, 75 (2014) 174 - 181.

[16]. P.P. Mokoena, M. Gohain, B.C.B. Bezuidenhoot, H.C. Swart, O.M. Ntwaeaborwa, Journal of Luminescence, 155 (2014) 288 - 292.

[17]. J. Gangwar, K.K. Dey, Komal, Paraveen, S.K. Tripathi, A. K. Srivastava, Advanced Materials Letters, 2 (2011) 402 - 408.

[18]. Y. Zheng, W. Wang, Journal of Solid State Chemistry, 210 (2014) 206 - 212.

[19]. L. Grigorjeva, K. Smits, D. Millers, D. Jankovica, Materials Science and Engineering, 77 (2015) 012036 - 012044.

[20]. A.K. Rai, I.M.L. Das, K.N. Uttum, Emerging Trends in Laser & Spectroscopy and Application, (2010), Allied Publsihers PVT. Ltd, New Delhi, India, page 362.

[21]. J. Xie, L. Mei, J. Deng, H. Liu, B. Ma, M. Guan, L. Lia, G. Lv, Journal of Solid State Chemistry, 231 (2015) 212 - 216.

[22]. X. Chen, G.J. Salamo, S. Li, J. Wang, Y. Guo, Y. Gao, L. He, H. Ma, J. Tao, P. Sun, W. Lin, Q. Liu, Physica B, 479 (2015) 159 - 164.

[23]. C. Strohhofer, A. Polman, Optical Materials, 21 (2003) 705 - 712.

[24]. H. Lin, C.P. Huang, W. Li, C. Ni, S.I. Shah, Y.-H. Tseng, Applied Catalysis B: Environment 68 (2006) 1 - 11.

[25]. Y. Peng, J. He, Q. Liu, Z. Sun, W. Yan, Z. Pan, Y. Wu, S. Liang, W. Cheng, S. Wei, The Journal of Physical Chemistry C, 115 (2011) 8184 - 8188.

[26]. M.A. Ahmed, M.F. Abdel-Messih, Journal of Alloys and Compounds, 509 (2011) 2154 - 2159.

[27]. U.O.A. Aner, F.Z. Tepehan, Composites: Part B, 58 (2014) 147 - 151.

[28]. K.R. Nemade, S.A. Waghuley, Ceramics International, 40 (2014) 6109 - 6113.

[29]. G. Lakshminarayana, J. Qiu, M.G. Brik, G.A. Kumar, I.V. Kityk, Journal of Physics: Condensed Matter, 20 (2008) 375101 - 375109.

[30]. Z. Zhang, J. Zhang, W. Zhou, M. Song, W. Li, Q. Hu, X. Zhao, Advanced Materials Research, 66 (2009) 167 - 170.

[31]. A. Patra, C.S. Friend, R. Kapoor, P.N. Prasad, Chemistry of Materials, 15 (2003) 3650 - 3655.

[32]. R.S. Quimby, W.J. Miniscalco, B. Thompson, Journal of Applied Physics, 76 (1994) 4472 - 4478.

[33]. L. Li, H. Lin, X. Zhao, Y. Wang, X. Zhou, C. Ma, X. Wei, Journal of Alloys and Compounds, 586 (2014) 555 - 560.

[34]. X. Bai, D. Li, Q. Liu, B. Dong, S. Xu, H. Song, Journal of Materials Chemistry, 22 (2012) 24698 - 24704.

[35]. Q. Shang, H. Yu, X. Kong, H. Wang, X. Wang, Y. Sun, Y. Zhang, Q. Zeng, Journal of Luminescence, 128 (2008) 1211 - 1216.

[36]. M.Y. Yoo, J.H. Lee, H.M. Jeong, K.S. Lim, P. Babu, Optical Materials, 35 (2013) 1922 - 1926.

[37]. D. Chen, Y. Zhou, Z. Wan, P. Huang, H. Yu, H. Lu, Z. Ji, Journal of the European Ceramic Society, 35 (2015) 2129 – 2137.

8. Conclusion

8.1 Summary

The corundum phase (α- Al_2O_3:Yb^{3+}) phosphor powder has been successfully synthesized by solution combustion method at a temperature of 550 ^{o}C. The powder X-ray diffractometer (XRD) patterns confirm that the phosphor crystallized in the hexagonal phase of α-Al_2O_3 with space group R3c. The post-preparation annealing did not transform the phase (α-Al_2O_3:Yb^{3+}) but crystallinity was improved at high temperatures from 1000 ^{o}C to 1400 ^{o}C. The Fourier transform infrared (FTIR) measurements confirmed the formation of α-Al_2O_3:Yb^{3+}. Field emission scanning electron microscope (FE-SEM) confirmed that the trivalent ytterbium (Yb^{3+}) dopant ions occupied grain boundaries before substituting Al^{3+} ions. The bluish-green emission was observed as the results of cooperative luminescence of Yb^{3+}. The near infrared (NIR) emission of Yb^{3+} was observed under excitation of 325 nm helium-cadmium (He-Cd) laser as a result of energy transfer from the α-Al_2O_3 to the dopant Yb^{3+}. The possible mechanism of the energy transfer was illustrated and discussed. These results show that α- Al_2O_3:Yb^{3+} can be synthesised by using solution combustion method at a relatively low temperature of 550 ^{o}C. The cooperative luminescence of singly doped Yb^{3+} was observed when high concentration of Yb^{3+} was added to the host. This cooperative luminescence can be very useful in blue light emitting phosphors applications.

The TiO_2:Er^{3+} nano-phosphor powder has been successfully synthesized by sol-gel method at room temperature preparation and the powder was annealed at 650 ^{o}C to form a desired phase. XRD confirms that nano-phosphor crystallized in the tetragonal phases of anatase and rutile with space groups of $\frac{4_1}{a}$md and $P\frac{4_2}{m}$nm, respectively. The XRD data confirmed the decrease in crystallite size when the concentration of Er^{3+} increases. The increase of Er^{3+} concentration increases the energy bandgap due to quantum size effect. The FE-SEM confirms nano-rods with diameter and length of 78 ± 36 nm and 1.51 ± 0.30 µm, respectively. All vibration bonds for Ti-O were observed at FTIR and were assigned to TiO_6 octahedral group. The red and intense green up-conversion (UC) emission was observed from photoluminescence (PL) spectroscopy upon excitation by 980 nm. The possible mechanism showing ground state absorption (GSA) and excited state absorption (ESA) of the Er^{3+} ion was illustrated and discussed. These results show that the incorporation of Er^{3+} in the host inhibited transformation of TiO_2 anatase to rutile phase, increases optical bandgap and prevent particle growth. The green and red UC emission suggested that the nano-phosphor material has potential applications in dye sensitized solar cells (DSSCs).

The nano-composites of Al_2O_3-TiO_2:Yb^{3+},Er^{3+}/Tm^{3+} phosphor powders were successfully synthesized by sol-gel method. XRD confirms the mixed oxides of titania rutile phase and an early crystallization of α-Al_2O_3 phase with crystallite size of ~ 38 nm in diameter. FE-SEM analyses confirmed the formation of self-assembled nano-rods and spherical particles. UV-vis confirmed strong band-to-band absorption at 380 nm and optical bandgap of ~ 3.0 eV was estimated from the Tauc plot. The FTIR analysis demonstrated the characteristics absorption peaks of Ti-O-Ti and Al-O-Al bonds which confirmed formation of alumina – titania system. The Yb^{3+}/Er^{3+} codoped phosphors exhibit the most intense red up-conversion emission with Commission Internationale de I'Eclairage (CIE) coordinates showing a phosphor with yellowish-green visible colour, while Yb^{3+}/Tm^{3+} codoped samples display the most intense NIR up-conversion luminescence. The possible mechanism showing ESA and energy transfer up-conversion (ETU) between Yb^{3+}/Er^{3+} and Yb^{3+}/Tm^{3+} was illustrated and discussed. The results from UC measurements suggest that by co-doping Yb^{3+} along with Er^{3+} improved red emission, while Tm^{3+} it enhanced the NIR emission. The nano-composites did not mix well in the particle level to form a new compound but they have formed clusters of like materials whereby titania is more dominant than alumina.

8.2 Future work

The preparation of a highly UC luminescence phosphor based nano-materials is very important for considering the potential application of these nano-composites in solar cells. There are several strategies that can be employed to enhance the UC luminescence including impurity (cations) doping and construction of core@shell nano-structures. In impurity doping it is a known factor that the UC luminescence intensities of rare-earths (RE) are dependent on electronic transition probabilities, which are very sensitive to the surrounding environment of RE. Therefore, tailoring the local crystal field of the RE can be considered as one of the most effective method to enhance the UC luminescence of various host matrixes doped with different up-conversion rare-earths (UCRE). The crystal symmetry in UC phosphor based nano-materials can be changed by an intentional doping of non-luminescent cations such as lithium (Li^+), bismuth (Bi^{3+}), iron (Fe^{3+}), scandium (Sc^{3+}) and calcium (Ca^{2+}). For example this can be done by triply doped Al_2O_3-TiO_2:Yb^{3+},Er^{3+},Li^+ phosphors. In a case of core@shell nanostructures, the shell improves UC emission by shielding the luminescence ions in the core from non-radiative relaxation caused by surface defects, as well as from vibrational deactivation ascribed to solvent molecules and ligands absorbed on the nano-material surface. The proposed core@shells are TiO_2:Yb^{3+},Er^{3+}@Al_2O_3 and TiO_2:Yb^{3+},Tm^{3+}@Al_2O_3 or Al_2O_3: Yb^{3+},Tm^{3+}@TiO_2 and Al_2O_3: Yb^{3+},Tm^{3+}@TiO_2. The influence of a volume ratio in Al_2O_3-TiO_2: RE can be varied to investigate the nano-composites features and UC luminescence properties. The power dependence of UC measurements on phosphor powders plays an important role in depicting how many photons are absorbed during UC process. The nano-composite will be incorporated into solar cell devices and the power conversion efficiencies of the devices will be measured.